TRANSCUTANEOUS POWER AND ULTRASONIC BLOOD-FLOW VELOCITY SENSORS

Philip James Curtis

SECURITY CLASSIFICATION OF THIS PAGE (When Data Entered)

REPORT DOCUMENTATION PAGE

READ INSTRUCTIONS BEFORE COMPLETING FORM

1. REPORT NUMBER

2. GOVT ACCESSION NO.

3. RECIPIENT'S CATALOG NUMBER

4. TITLE (and Subtitle)

TRANSCUTANEOUS POWER AND ULTRASONIC BLOOD-FLOW VELOCITY SENSORS

5. TYPE OF REPORT & PERIOD COVERED

THESIS

6. PERFORMING ORG. REPORT NUMBER

7. AUTHOR(s)

CURTIS, PHILIP JAMES

8. CONTRACT OR GRANT NUMBER(s)

9. PERFORMING ORGANIZATION NAME AND ADDRESS

STANFORD UNIVERSITY

10. PROGRAM ELEMENT, PROJECT, TASK AREA & WORK UNIT NUMBERS

11. CONTROLLING OFFICE NAME AND ADDRESS

CODE 031
NAVAL POSTGRADUATE SCHOOL
MONTEREY, CALIFORNIA, 93940

12. REPORT DATE

MAR 78

13. NUMBER OF PAGES

112

14. MONITORING AGENCY NAME & ADDRESS(if different from Controlling Office)

15. SECURITY CLASS. (of this report)

UNCLASS

15a. DECLASSIFICATION/DOWNGRADING SCHEDULE

16. DISTRIBUTION STATEMENT (of this Report)

APPROVED FOR PUBLIC RELEASE; DISTRIBUTION UNLIMITED

17. DISTRIBUTION STATEMENT (of the abstract entered in Block 20, if different from Report)

18. SUPPLEMENTARY NOTES

19. KEY WORDS (Continue on reverse side if necessary and identify by block number)

TRANSCUTANEOUS, TRANSCUTANEOUS POWER, ULTRASONIC, BLOOD-FLOW, VELOCITY SENSORS

20. ABSTRACT (Continue on reverse side if necessary and identify by block number)

SEE ATTACHED.

DD FORM 1 JAN 73 1473 (Page 1)

EDITION OF 1 NOV 65 IS OBSOLETE
S/N 0102-014-6601

UNCLASS

SECURITY CLASSIFICATION OF THIS PAGE (When Data Entered)

TRANSCUTANEOUS POWER

AND

ULTRASONIC BLOOD-FLOW

VELOCITY SENSORS

A THESIS
SUBMITTED TO THE DEPARTMENT OF ELECTRICAL ENGINEERING
AND THE COMMITTEE OF GRADUATE STUDIES
OF STANFORD UNIVERSITY
IN PARTIAL FULFILLMENT OF THE REQUIREMENTS
FOR THE DEGREE OF
ENGINEER

BY

LCDR PHILIP JAMES CURTIS USN

MARCH 1978

Approved for public release;
distribution unlimited.

Approved for the Electrical Engineering Department:

Approved for the University Committe
on Graduate Studie

ABSTRACT

Ultrasonic flow sensors to monitor blood flow in animals and humans have been in use for many years. This study draws on the experience of past research to solve some of the recurring problems found with implanted sensors. Four areas have been explored, all linked by the contribution each makes toward the development of an improved blood-flow sensor.

In the first, the use of transcutaneous power to operate an implanted ultrasonic blood-flow sensor is analyzed. The purpose of such a study is the total elimination of batteries. The theory of transcutaneous power is developed from the basic equations of Maxwell and Stefan and a basic efficiency statement is derived. Design guidelines and graphs are generated from this statement and basic experiments are conducted to indicate the validity of the theory. The conclusion is that a properly designed and applied transcutaneous power-transfer circuit is capable of efficiencies as high as 90%.

A high-efficiency low-voltage regulator and a low-voltage reference are developed in the second area. This regulator and reference are compatible with existing low-voltage implantable circuits intended initially to be battery powered. The regulator is capable of delivering 2.7 V (two mercury cells in series) with better than 85% efficiency; the voltage reference operates from less than 100 μA and has a temperature stability better than 200 ppm/°C.

The third area details an extensive program involving the design, fabrication and employment of a discrete-component continuous-wave implanted ultrasonic doppler blood-flow velocity sensor. The study

includes circuit design and construction, package encapsulation and extensive clinical results obtained from more than 975 functioning implant hours with 12 different flow sensors. Among the conclusions derived is the need for an alternative to batteries as a source of power.

In the fourth area, transcutaneous power, low-voltage regulator design and the original ultrasonic blood-flow unit are combined in the first of its kind transcutaneously powered blood-flow velocity sensor. The details of this sensor are described in addition to the results of two implants with a prototype unit. The overwhelming conclusion is that transcutaneous power is an immensely practical alternative to battery power for certain clinical experiments.

CONTENTS

ILLUSTRATIONS

ACKNOWLEDGMENTS

This study could not have been completed without the support of Dr. J. D. Meindl, who gave me the opportunity to become a member of the Blood Flowmeter Group and assigned to me the task of redesigning the discrete-component flow sensor. The success achieved in this undertaking was largely a result of the well-defined goals he established and the encouragement and guidance he offered.

The Burke Scholarship Program of the U. S. Navy supported me financially throughout my research at Stanford University. Mr. Wayne Foletta was a constant source of invaluable information and ideas and was responsible for many of the technical suggestions that made the project a success. The timely production of all completed blood-flow sensors was the result of the expertise of Mr. Ron Tapperell who prepared the necessary piezoelectric transducers.

The completion of this manuscript and the research that preceded it would not have been possible without the understanding and patience of my family and wife Linda.

Chapter I

INTRODUCTION

A. Background

Medical researchers and physiologists agree that accurate quantitative information concerning animal physiology in disease and health is necessary to advance the development of preventive and prosthetic medicine for human patients. The measurement of blood flow is one of the principal areas in which this information is required. To ensure that such information is accurate, it must be measured by noninvasive techniques. Currently, blood-flow measuring sensors, optimized with respect to their noninvasive nature, operate in three basic ways -- transcutaneously (across the skin), percutaneously (piercing the skin), or subcutaneously (under the skin). Transcutaneous systems are simple to maintain and afford easy data collection but often lack resolution and require confinement of the subject. Percutaneous systems have the same maintenance and data-collection advantages in addition to good resolution, but the connection through the skin creates problems with infection when measurements are required on a chronic basis. Subcutaneous systems have good resolution and complete subject mobility but are difficult to maintain because battery or other sensor failures require surgery to correct.

The subcutaneous approach has the potential of being the best sensor for the measurement of blood flow. It is capable of better resolution than a transcutaneous system and it eliminates the infection problems associated with percutaneous connections. To realize its full potential, the difficulties associated with its operating power must be resolved. This investigation centers on an alternative to batteries as means of power and the development of a simple blood-flow measuring sensor. The alternative to

batteries is inductive coupling where transformer action delivers power to the subcutaneous sensor. Induced power for physiological studies dates back to 1934 when Chaffee and Light [1] used it to stimulate the brain of a monkey.

This study is an attempt to develop the theoretical and practical aspects of a transcutaneous power-transmission system designed to be compatible with subcutaneous low-power integrated-circuit sensors intended for chronic application. Such a system should become a basic building block for a wide range of subcutaneous systems that require long implant duration, periodic data collection, freedom of mobility between data-collection periods, elimination of possible infection and a lack of nonaesthetic surface encumbrances.

B. Transcutaneous Power Transmission

Figure 1 is a block diagram of the transcutaneous power-transmission system. The inductive transfer coils consist of a flat spiral coil external to the subject and a similar coil implanted with the electronic sensor.

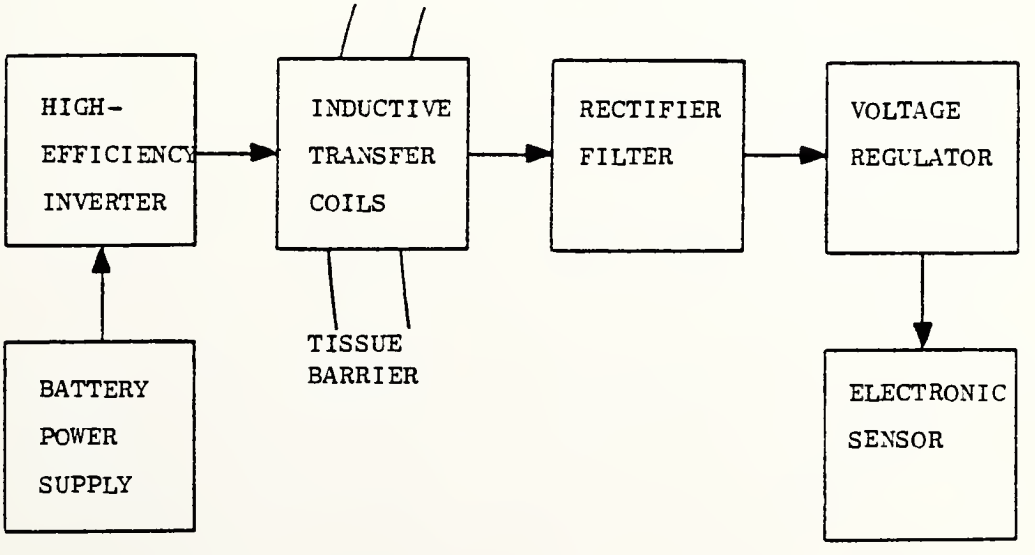

Fig. 1. TRANSCUTANEOUS POWER-TRANSMISSION SYSTEM.

The high-efficiency battery-powered inverter drives the external power coil at a fixed frequency. The internal power coil absorbs the energy contained in the time-varying magnetic field thus established. The time-varying current and voltage is then rectified, filtered and regulated. The voltage regulator minimizes the input-output voltage differential, thereby maximizing regulator efficiency; it is also temperature compensated and can be adjusted to produce any voltage from 1.35 to 20 V. This voltage then operates the physiological sensor. Except for the power coil and a minimum number of discrete components, the subcutaneous system is to be fabricated in monolithic form for small-volume compatibility with integrated-circuit sensors.

Since 1934 when Chaffee and Light used inductive coupling to electrically stimulate nerves, many medical researchers and biomedical engineers have used induced power. The great majority of published information emphasizes two specific applications--remote stimulation of the natural heart (pacemakers) and remote powering of an artificial heart. From the late 1950's through the late 1960's, several papers appeared, describing inductively powered artificial pacemakers [2-8], based predominantly on clinical experiences. The electronics employed were always of secondary importance, and optimal power-transmission efficiency and frequency were rarely discussed. Recent advances in battery longevity and reliability and improved circuit designs for implanted pacemakers have resolved the problems that the induced pacemaker sought to overcome.

Inductive power transmission for artificial hearts is much discussed in the literature [9-30]. Generally, the techniques are similar. All systems employ pancake-type coils--aircore or ferritecore. Operating

frequencies range from 3 kHz to 450 kHz and power levels vary from 30 to 1000 W. Most of these papers discuss power-transfer efficiency and a few, notably those by Schuder [21] and Fuller [11], derive an expression for maximum efficiency in terms of the most significant coil parameters but do not indicate the relationship between frequency and the parameters that determine power losses. Operating frequencies are usually determined by such practical constraints as available transistors, power amplifiers and RF interference. All support the opinion that inductive power transfer for biomedical applications is practical. Although the subjects of heart pacing and artificial-heart power are the most thoroughly studied, the great volume of research is based on laboratory experiences with functioning systems. The basic engineering concepts are contained in perhaps four selected papers.

Other applications have also produced interesting literature. Inductively powered bladder stimulators for patients suffering vesical dysfunction have achieved clinical success [31-33]. The engineering aspects of such studies are equivalent to the heart-pacemaker studies. The implanted circuitry consists of a coil, capacitor and electrode for the bladder stimulators and the same elements plus a diode for the heart pacers. More complex subcutaneous power processing has been used by only a few researchers. In 1965, Ko and Yon [34] reported inductively powered subcutaneous EMG and EKG sensors whose power supply included simple-diode rectification and zener-diode voltage regulation. A similar rectification and clamping circuit was described by Leonhardt and Hodges [35] in an inductive power system to operate a visual cortex stimulator for blind subjects. Fryer and Sandler [36] used inductive power transfer to recharge nickel-cadmium

batteries in a variety of subcutaneous systems for monitoring physiological data; in these systems, the battery provides the necessary voltage regulation.

Induced power for biomedical applications has been in use for over 40 years, but most of the literature is application oriented. No single engineering study has been made to quantify and characterize all the significant factors affecting efficient power transfer. No guidelines have been generated for coil design to minimize losses and to maximize coupling. No attempt has been made to develop an induced power system that produced a stable regulated output voltage capable of replacing batteries in current subcutaneous sensors. This report investigates these problems and develops the necessary theoretical and practical guidelines to solve them.

C. Blood-Flow Velocity Sensors

Because nearly one-half of all deaths in the United States result from disorders of the heart and circulatory system, the analysis of blood flow is significant. The quantity most desired from a blood-flow measurement is volume of flow; however, many research studies only require a measurement of blood-flow velocity near the center of the vessel lumen.

One goal of this investigation is the development of a basic blood-flow velocity sensor whose characteristics include low-power operation, small size, economy of fabrication, simplicity and reproducibility. The method of flow-velocity measurement is based on ultrasonic doppler principles. The sensor design and principles of operation are not totally unique; however, the engineering methods and attitudes used in its production have resulted in a very successful device. Twelve identical sensors have been

fabricated and have been in continuous operation since May 1973. More recently, the basic blood-flow velocity sensor has been combined with the transcutaneous power system to produce a package capable of chronic implantation and unlimited data collection.

D. Approach

The problem of optimal power-transmission efficiency is discussed in Chapter II. Various tuning arrangements for the transmission coils are reviewed and analyzed, and an expression for load resistance is developed. Optimal system frequency is derived in terms of the significant physical parameters. The factors affecting coil losses and coil design are described. Guidelines are established for coil configurations, and factors contributing to maximum coil coupling are studied.

Power rectification and regulation are the subject of Chapter III. A voltage regulator is designed to maximize power efficiency by minimizing the required input-output voltage differential. A new low-voltage temperature-compensated reference is introduced and developed. The rectifier, regulator and reference are designed for monolithic fabrication.

In Chapter IV, a basic discrete-component blood-flow velocity measuring sensor is developed, including its operating principles and required circuits. Package encapsulation techniques are described. The results of field experiences from a number of units are reviewed, from which a clear conclusion concerning sources of power is made.

In Chapter V, transcutaneous power transfer is combined with the blood-flow velocity measuring sensor in a single package. Because this CW doppler flowmeter operates with very low level and relatively wideband signals, it

provides a most stringent test of the quality of the transcutaneous power source. The sensor and power-transfer system design are detailed, and field experience with the prototype unit is described. Chapter VI discusses the conclusions of the investigation.

E. Contributions

The following contributions are the results of this investigation in the areas of biomedical engineering and solid-state circuit theory:

(1) An optimal power-transmission efficiency theory that includes all the significant contributing factors, and a practical application of the theory in the construction of a transcutaneous power system to operate chronically implanted physiological sensors.

(2) A subcutaneous system consisting of a rectifier, reference and a high-efficiency low-voltage regulator designed for monolithic fabrication and compatibility with integrated-circuit sensors.

(3) A temperature-stabilized low-voltage reference circuit for monolithic fabrication.

(4) A practical and functional miniature discrete-component blood-flow velocity sensor with over 20 successful implants.

(5) The first transcutaneously powered ultrasonic blood-flow velocity sensor.

Chapter II

OPTIMAL POWER TRANSMISSION

This chapter discusses the theoretical and practical aspects of a transcutaneous power transmission circuit. Expressions for the power-transfer efficiency of inductively coupled external and subcutaneous coils (modeled with simple RLC ladder networks) demonstrate the greater efficiency of tuned circuits over untuned circuits. From these expressions, equations are derived for optimal load resistance. The relationship between coil inductance, coupling coefficient, frequency and optimal load resistance is developed to facilitate the design of a circuit that can achieve maximum efficiency for a given load resistance. The factors that cause power loss are described and their frequency dependence is established. The effects of coil capacitance and nonuniform current distribution on coil Q are analyzed to determine the optimal operating frequency. The factors affecting coil coupling are also studied. Maxwell's equation for the mutual inductance between two wire circles is used to set the maximum possible values of the coupling coefficient for various coil spacings and relative coil sizes. Guidelines are generated for coil-winding configurations to maximize the coupling coefficient.

A. Power-Transfer Efficiency

Inductive coupling can transfer power from an external coil to a subcutaneous coil. Inefficiencies in this power transfer are the result of coil losses and separation caused by the tissue barrier. Coil losses, separation and LC tuning can be modeled adequately by a simple RLC ladder

network. The primary coil (external) and secondary coil (subcutaneous) can be either parallel or series tuned (Fig. 2) to maximize efficiency and to make the power-transfer process more practical. Using network

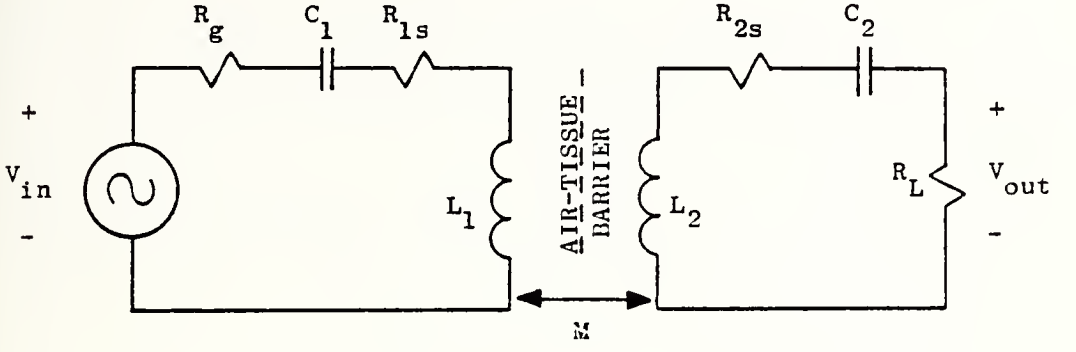

a. Series-tuned secondary circuit

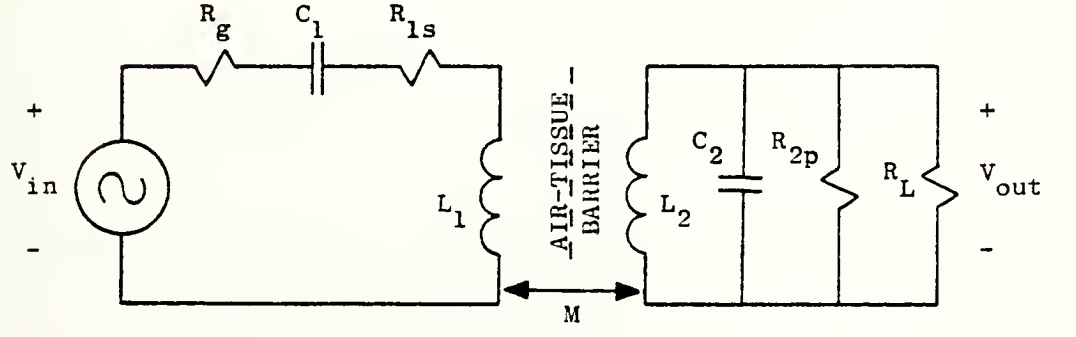

b. Parallel-tuned secondary circuit

Fig. 2. POWER-TRANSFER CIRCUIT MODEL

theory and tedious calculations, expressions can be derived for V_{out} and Z_{in}; then, P_{out} and P_{in} are calculated from

$$P_{out} = |V_{out}|^2 \frac{1}{R_L} \tag{2.1a}$$

and

$$P_{in} = \mathrm{Re}\left[V_{in}^2 \frac{1}{Z_{in}}\right] \tag{2.1b}$$

or

$$P_{in} = \mathrm{Re}\left[I_{in}^2 Z_{in}\right] \tag{2.1c}$$

Power-transfer efficiency is defined as

$$\mathrm{eff} = \frac{P_{out}}{P_{in}} \tag{2.2}$$

For the series-tuned secondary circuit, the efficiency equation is

$$\mathrm{eff}_s = M^2 C_2^2 R_L \omega^4 \left\{ [M^2(R_{2s} + R_L) + L_2^2(R_{1s} + R_g)]\, C_2^2 \omega^4 + [C_2^2(R_{2s} + R_L)^2 (R_{1s} + R_g) - 2C_2 L_2 (R_{1s} + R_g)]\omega^2 + (R_{1s} + R_g) \right\}^{-1} \tag{2.3}$$

which can be manipulated to produce an efficiency expression for a non-resonant circuit by allowing C_2 to become infinitely large. In effect, this short circuits C_2 and eliminates it from the circuit in Fig. 2a. Under these conditions, Eq. (2.3) reduces to

$$\text{eff}_s \text{ (nonresonant)} = \frac{R_L}{R_L + R_{2s} + \dfrac{L_2 (R_{1s} + R_q)}{L_1 k^2} + \dfrac{(R_{1s} + R_q)(R_{2s} + R_L)^2}{L_1 L_2 k^2 \omega^2}} \tag{2.4}$$

where k is the coupling coefficient defined as $k^2 = M^2/L_1L_2$.

The best frequency for the series-tuned secondary circuit is found by differentiating Eq. (2.3) with respect to ω; the result is

$$\omega^2 = \left[C_2L_2 - \tfrac{1}{2}C_2^2 (R_{2s} + R_L)^2\right]^{-1} \tag{2.5}$$

Under normal conditions,

$$C_2L_2 \gg \tfrac{1}{2}C_2^2 (R_{2s} + R_L) \tag{2.6}$$

and a good approximation to ω^2 is

$$\omega^2 \approx [C_2L_2]^{-1} \tag{2.7}$$

For the circuit configuration in Fig. 2a, Eqs. (2.3) and (2.5) demonstrate that power-transfer efficiency depends on the secondary rather than the primary circuit being tuned. Primary-circuit tuning is important only because it reduces Z_{in} and makes it easier to deliver power to R_L; without such tuning, high voltages are required to achieve reasonable power levels. Battery-operated external-power oscillators are more practical because, with tuning, they operate into a low-impedance load (10 to 100 Ω) and the voltage and current levels are within reasonable limits.

Substituting Eq. (2.7) into Eq. (2.3) produces the efficiency expression for Fig. 2a, with the secondary circuit tuned to series resonance. The result is [11]

$$\text{eff}_s = \frac{R_1}{R_L + R_{2s} + \dfrac{(R_{1s} + R_g)(R_{2s} + R_L)^2}{L_1 L_2 k^2 \omega^2}} \tag{2.8}$$

which, when compared to Eq. (2.4), indicates that a tuned secondary circuit improves power-transfer efficiency over an untuned secondary. The tuned secondary eliminates the primary-circuit resistance term reflected into the secondary by the transformer action of the coils. This term is significant because it is approximately $k^{-2} \times R_{2s}$, assuming $L_1 \approx L_2$, $R_{1s} \approx R_{2s}$, and $R_{1s} \gg R_g$. Because k is typically 0.1 to 0.25, k^{-2} is 16 to 100.

It can be seen in Eq. (2.8) that efficiency is related to all coil and coupling parameters and to load resistance. Each subcutaneous physiological sensor has a specific voltage and current requirement which determines the load resistance seen by the power-transfer circuit. If this relationship is established for maximum efficiency, it is possible to design the circuit for the voltage-current requirement of a given sensor. To determine this relationship Eq. (2.8) is differentiated with respect to R_L; the result is

$$R_{L\ opt} = \left[\frac{R_{2s}}{(R_{1s} + R_g)} L_1 L_2 k^2 \omega^2 + R_{2s}^2 \right]^{1/2} \tag{2.9}$$

Some good assumptions for practical circuits are

1. $R_{2s} \approx R_{1s} \gg R_g$
2. $L_1 \approx L_2$
3. $R_{L\ opt}^2 \gg R_{2s}^2$

The optimal load resistance for a circuit with a series-resonant secondary then becomes

$$R_{L\ opt} \approx kL\omega \tag{2.10}$$

where R_L is determined by the physiological sensor and k is determined by the size of the coils and their separation. As a result, coil inductance and circuit frequency can be adjusted according to Eq. (2.10) to produce maximum power-transfer efficiency.

For the parallel-tuned secondary circuit in Fig. 2b, the efficiency expression is

$$eff_p = M^2 \frac{1}{R_L} \omega^2 \left\{ C_2^2 L_2^2 (R_{1s} + R_g)\omega^4 + \left[L_2^2 (R_{1s} + R_g) \left(\frac{1}{R_{2p}} + \frac{1}{R_L} \right)^2 \right.\right.$$

$$\left.\left. - 2C_2L_2(R_{1s} + R_g) + \left(\frac{1}{R_{2p}} + \frac{1}{R_L} \right) M^2 \right] \omega^2 + (R_{1s} + R_g) \right\}^{-1} \tag{2.11}$$

Which, by setting $C_2 = 0$, reduces to an expression for power-transfer efficiency with the secondary untuned. This is the same as eliminating C_1 from Fig. 2b and deriving an equation for efficiency,

$$eff_p \text{ (nonresonant)} = \frac{1/R_L}{\frac{1}{R_L} + \frac{1}{R_{2p}} + \frac{R_{1s} + R_g}{\omega^2} + \frac{L_2}{L_1 k^2} (R_{1s} + R_g) \left(\frac{1}{R_{2p}} + \frac{1}{R_L} \right)^2} \tag{2.12}$$

If the secondary circuit in Fig. 2b is tuned with C_2, then Eq. (2.11) can be differentiated with respect to ω, equated to zero, and solved for ω.

$$\omega^2 = (C_2L_2)^{-1} \tag{2.13}$$

This result is exact, not approximate as in Eq. (2.7) for the series-tuned secondary circuit. Similar to the circuit in Fig. 2a, the efficiency of the circuit in Fig. 2b depends only on the secondary being tuned. Equations (2.11) and (2.13) demonstrate that efficiency is independent of C_1 and primary-circuit tuning.

Substituting Eq. (2.13) into (2.11) produces an equation for efficiency with a parallel resonant secondary circuit

$$\text{eff}_p = \frac{1/R_L}{\frac{1}{R_L} + \frac{1}{R_{2p}} + \frac{L_2}{k^2 L_1}(R_{1s} + R_g)\left(\frac{1}{R_L} + \frac{1}{R_{2p}}\right)^2} \tag{2.14}$$

which, when compared to Eq. (2.12), shows how parallel resonance in the secondary circuit increases efficiency by eliminating the $(R_{1s} + R_g)/\omega^2$ term. Equation (2.14) can be manipulated to yield R_L optimum for the parallel-tuned secondary circuit:

$$R_{L\ opt} = \left(\frac{R_{1s}R_{2p}^2 L_2}{R_{2p}L_1 k^2 + R_{1s}L_2}\right)^{1/2} \tag{2.15}$$

For approximately similar high-Q coils,

1. $L_1 \approx L_2$
2. $R_{2p}k^2 \gg R_{1s}$

Then,

$$R_{L\ opt} \approx \left(\frac{R_{1s}R_{2p}}{k^2}\right)^{1/2} \tag{2.16}$$

A coil and its losses are modeled by placing a resistor in series R_s or in parallel R_p with the coil. The series resistor is always smaller than the parallel resistor, and the two are related by Q^2. Coil Q is the same whether the inductive reactance is cancelled by series or parallel capacitance. The definitions of Q for the two possible cases are

$$Q = \frac{L\omega}{R_s} = \frac{R_p}{L\omega} \tag{2.17}$$

Then,

$$R_s R_p = L^2\omega^2 \tag{2.18}$$

Substituting this into Eq. (2.16) yields

$$R_{L\ opt} \approx \frac{L\omega}{k} \tag{2.19}$$

Comparison of Eq. (2.10) to (2.19) reveals that the optimal load resistance for the series-tuned secondary circuit in Fig. 2a equals k^2 times the optimal for the parallel-tuned secondary circuit in Fig. 2b. As a result, the series-tuned circuit delivers power most efficiently into loads requiring low voltages and high currents, and the parallel-tuned circuit delivers power most efficiently into loads requiring higher voltages but lower current. For example, consider a pair of approximately equal high-Q coils with inductances of 350 μH and a coupling coefficient of 0.2. If the secondary (subcutaneous) coil is tuned to series resonance at 500 kHz, the optimal load resistance becomes

$$R_{L\ opt}\ (\text{series}) \approx kL\omega = [0.2][350\times10^{-6}][2\pi\times500\times10^{3}] = 220\,\Omega$$

If it is parallel tuned, the optimal would be

$$R_{L\ opt}\ (\text{parallel}) \approx \frac{L\omega}{k} = \frac{[350\times10^{-6}][2\pi\times500\times10^{3}]}{[0.2)} = 5500\,\Omega$$

The ratio between $R_{L\ opt}$ (series) and $R_{L\ opt}$ (parallel) is k^{-2} or 25. Further calculations indicate typical circuit efficiencies. The measured series-resonant resistance at 500 kHz is 9Ω.

Equations (2.4) and (2.8) are used to calculate the circuit efficiency for the nonresonant and series-resonant secondary circuits, respectively. Assuming negligible generator resistance, the results are

$$\text{eff}_s\ (\text{nonresonant}) = 0.48$$

$$\text{eff}_s = 0.92$$

The same efficiencies will result if Eqs. (2.12) and (2.14) are used for the parallel-resonant secondary circuit. The advantage of secondary-circuit resonance over nonresonance becomes apparent in this example.

With both series- and parallel-tuned secondary circuits, the optimal load resistance is a function of the coupling coefficient (k) between the external and subcutaneous coils, coil inductances and the power-transfer frequency. Inductance and frequency are well-controlled parameters. The coupling coefficient, however, depends on the orientation of the two coils; coil realignment and spacing will change this coefficient and the optimal load resistance.

Figure 3 plots the relationship of circuit efficiency to load resistance and coupling coefficient in a series-tuned secondary circuit having the above coil parameters. As k is varied, the value of R_L that yields maximum efficiency varies. If R_L and k are fixed, then Eq. (2.10) yields

the coil reactance ($L\omega$) for maximal efficiency. Over a given range of k values, an $L\omega$ exists that will yield the highest efficiency. The selection of this optimal $L\omega$ is determined by the procedure outlined below.

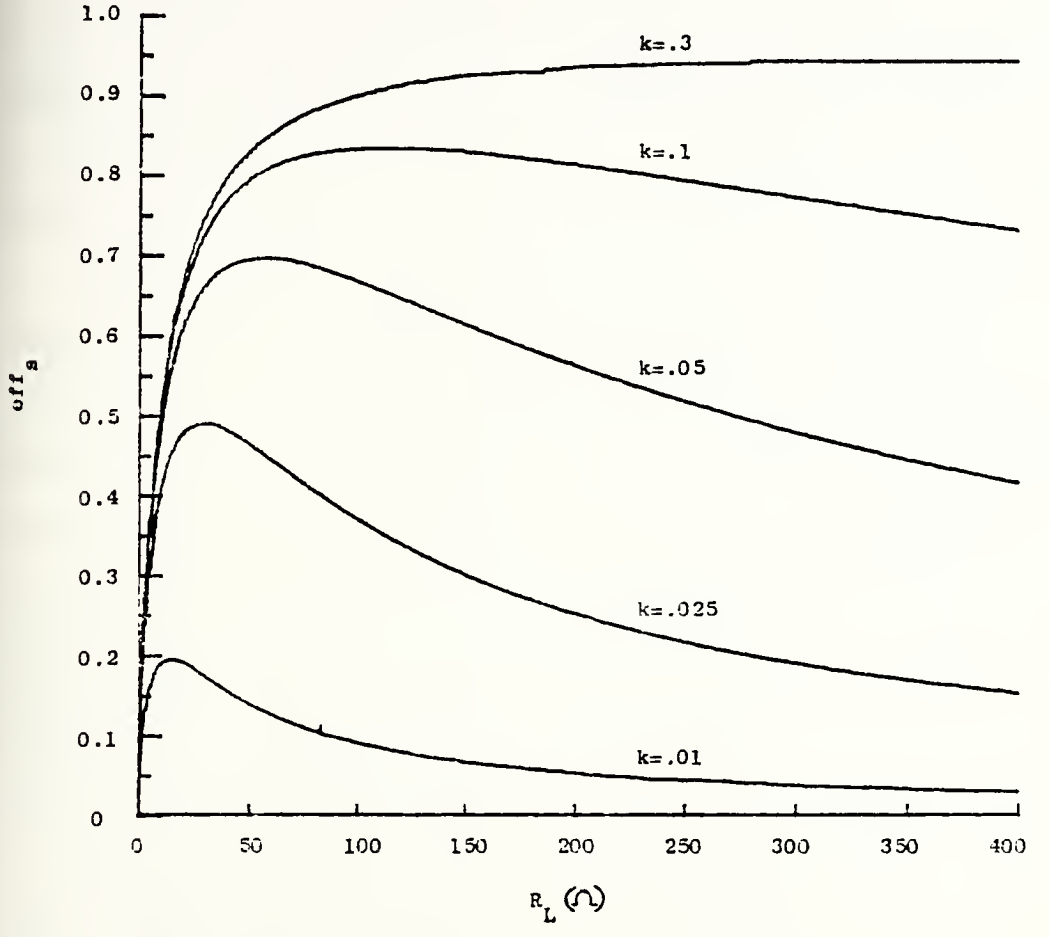

Fig. 3. POWER-TRANSFER CIRCUIT EFFICIENCY WITH SECONDARY SERIES TUNED VS LOAD RESISTANCE FOR TYPICAL VALUES OF COUPLING COEFFICIENT.

The design process begins with a given R_L because of the voltage-current requirement of the subcutaneous sensor. This value of load resistance is the best average and is identified as $\bar{R}_L$. Based on the size limitations of the implanted coil and on the application, the

range of values of the coupling coefficient is known -- k_1 is the lower limit and k_2 is the upper limit. From these values of $\bar{R}_L$, k_1, and k_2, the inductance and operating frequency of the external and implanted coils are determined in Fig. 4. The arguments necessary are the ratio k_2/k_1 and $\bar{R}_L/R_{ac}$, where R_{ac} is the ac resistance of the coil. The exact value of this resistance need not be known because coil reactance is not a strong function of R_{ac}; however, it can be estimated from the proposed coil size.

Figure 4 produces the ratio $k_1 L\omega/R_{ac}$ which is solved for $L\omega$. An infinite number of inductance-frequency combinations equal this value of $L\omega$, but only a certain range permits practical application because of coil size limitations and the frequency restraints imposed by the characteristics of the sensor. With $L\omega$ determined, the coil is wound and its ac resistance is measured which, most likely, will be different from the estimated R_{ac}. The new $\bar{R}_L/R_{ac}$ ratio is computed and another value of $k_1 L /R_{ac}$ is obtained; however, the resulting $L\omega$ does not vary greatly from the first value, and this difference can be corrected by changing ω.

For example, assume that the subcutaneous sensor requires 10 mA at 2.7 V. Because this is an $\bar{R}_L$ of 270Ω, the secondary circuit is series tuned. The largest possible coil set that is compatible with the size of the sensor has a minimum k of 0.05 and a maximum of 0.2. If the ac resistance is estimated at 10Ω, then

$$\frac{\bar{R}_L}{R_{ac}} = \frac{270\Omega}{10\Omega} = 27 \quad \text{and} \quad \frac{k_2}{k_1} = \frac{0.2}{0.25} = 4$$

From Fig. 4, $k_1 L\omega/R_{ac} \approx 16.6$ and $L\omega = 3320\Omega$. One solution to this $L\omega$ product is

$$L\omega = 528\ \mu H$$

$$f = 1\ MHz$$

When constructed, if the 528 μH coil measures 500 μH with $R_{ac} = 25\Omega$ at 1 MHz, then

$$\frac{\bar{R}_L}{R_{ac}} = \frac{270\Omega}{25\Omega} = 10.8$$

and

$$\frac{k_1 L}{R_{ac}} \approx 6.5$$

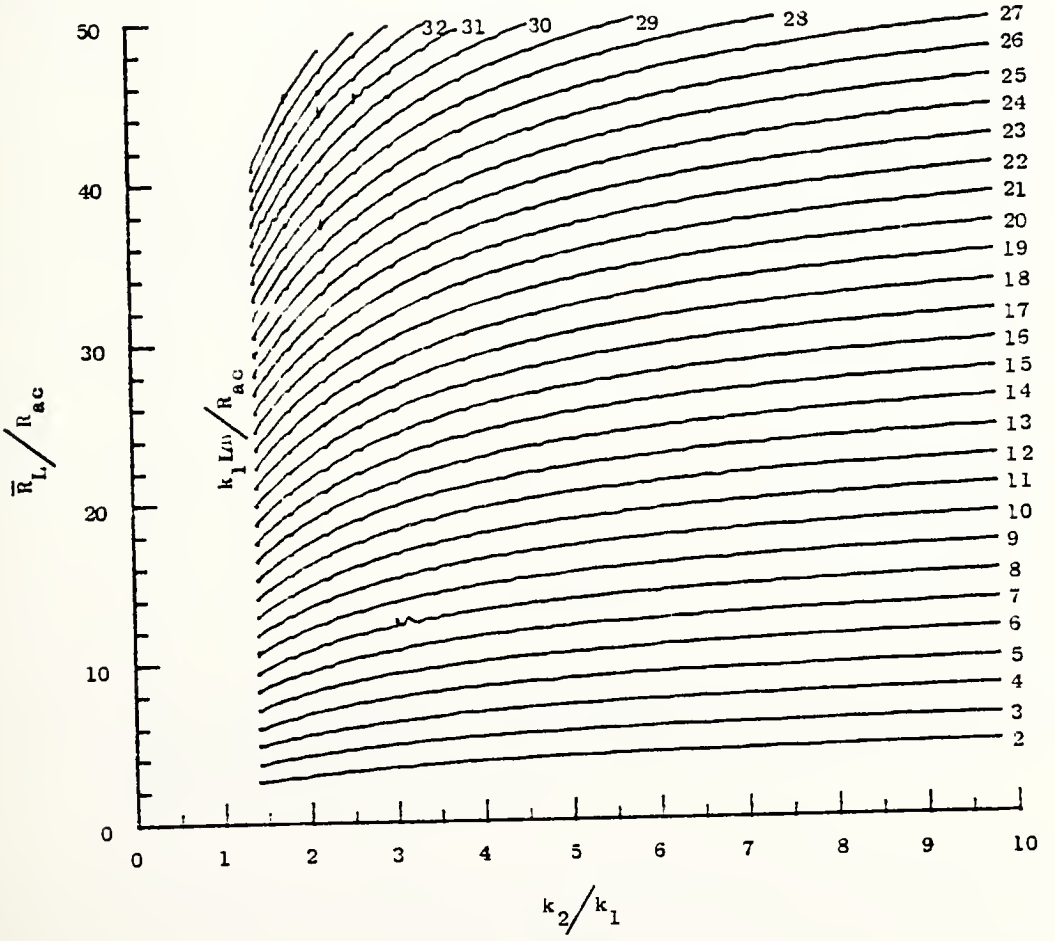

Fig. 4. NORMALIZED BEST-AVERAGE LOAD RESISTANCE VS RATIO OF MAXIMUM-TO-MINIMUM VALUES OF THE COUPLING COEFFICIENT FOR VARIOUS VALUES OF $k_1 L\omega / R_{ac}$.

Because the new optimal $L\omega$ is 3250, ω must be shifted from 1 to 1.04 MHz, which is well within the other design constraints.

In Fig. 5, percent efficiency is determined over the range from k_1 to k_2. With the above parameters, Eq. (2.10) can be used to compute $R_{L\ opt}$.

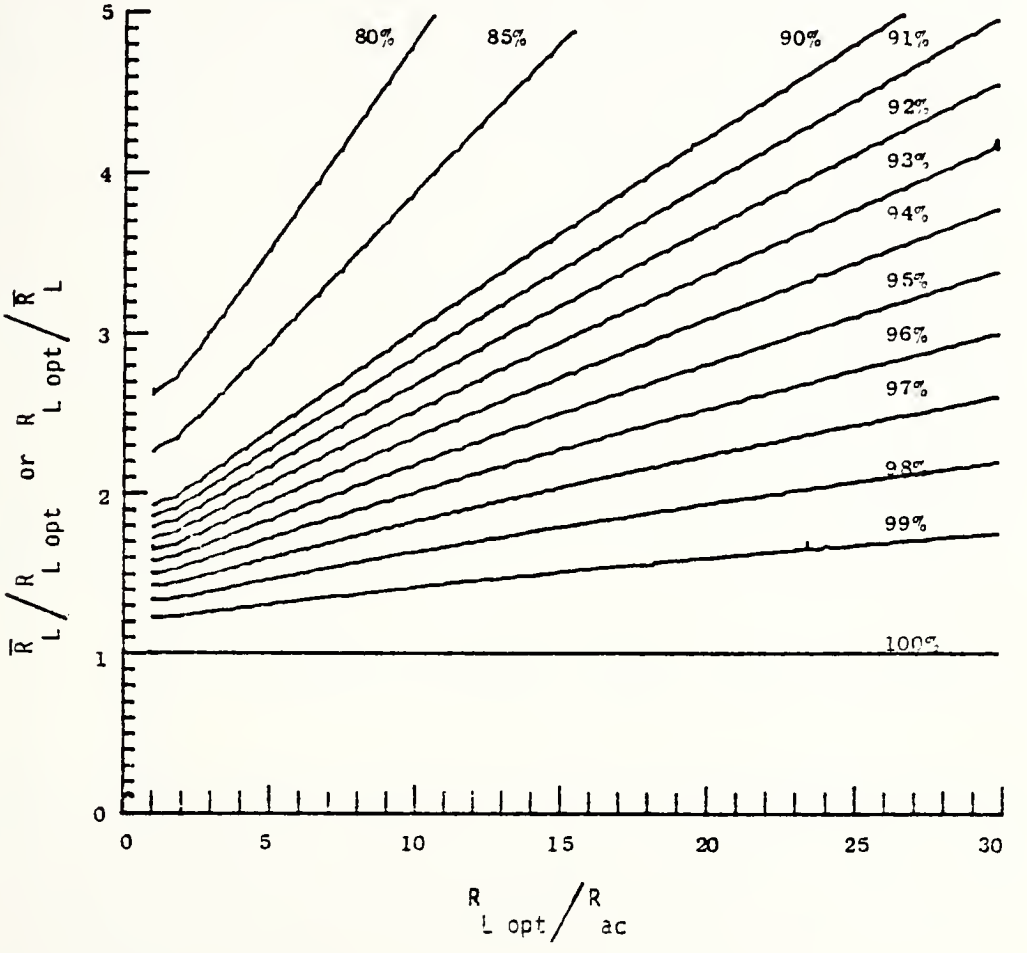

Fig. 5. RATIO OF BEST-AVERAGE LOAD RESISTANCE TO OPTIMAL LOAD RESISTANCE VS RATIO OF OPTIMAL LOAD RESISTANCE TO COIL ac RESISTANCE FOR VARIOUS PERCENT EFFICIENCIES.

Then the arguments $R_{L\ opt}/R_{ac}$ and $\bar{R}_L/R_{L\ opt}$ are required to derive the maximum percent efficiency. In this example, $R_{L\ opt}$ (series) for the lower limit of k (k_1) is 166Ω ,

$$\frac{R_{L\ opt}}{R_{ac}} = \frac{166}{25} = 6.6 \quad \text{and} \quad \frac{\bar{R}_L}{R_{L\ opt}} = \frac{270}{166} = 1.63$$

It can be seen in Fig. 5 that $\bar{R}_L$ achieves approximately 97% efficiency at the lower value of k.

Figures 4 and 5 can also be used to determine the optimal $L\omega$ when the secondary circuit is parallel tuned. The only additional information required is an estimate of the coil Q from which the parallel resonant resistance R_p can be approximated. In Fig. 4, $\bar{R}_L/R_{ac}$ is replaced by $R_p/\bar{R}_L$ and, in Fig. 5, $R_{L\ opt}/R_{ac}$ is replaced by $R_p/R_{L\ opt}$. All other arguments and the design process remain the same as for the circuit with a series-tuned secondary. Combining Eqs. (2.8) and (2.14) with their appropriate optimal load resistance [Eqs (2.10) and (2.19)] produces the following efficiency expression that can be applied to any primary or secondary tuning arrangement,

$$\text{eff} = \frac{kQ}{1 + kQ + \left(\frac{1}{kQ} + 1\right)^2} \tag{2.20}$$

from which it can be seen that efficiency is greatest when Q (coil-quality factor) and k (circuit-coupling coefficient) are maximum. The importance of individually maximizing both parameters is demonstrated in Fig. 6 where circuit efficiency is plotted vs the coupling coefficient as a function of coil Q.

The significant points in Section A are summarized as follows:

(1) For maximum efficiency, the secondary circuit (subcutaneous coil, capacitor and load) is capacitively tuned and the power-transfer frequency is fixed at

$$\omega^2 = [C_1 L_1]^{-1}$$

(2) Assuming the external and subcutaneous coils are approximately equal and have Q's > 20, the load resistance for maximum efficiency is

$$R_{L\ opt}\ [\text{series}] \approx kL\omega$$

$$R_{L\ opt}\ [\text{parallel}] \approx \frac{L\omega}{k}$$

(3) When the power-transfer circuit is operated at the resonant frequency of the secondary circuit ($\omega = 1/C_2L_2$) and the load resistance is optimum, the efficiency is given by the general expression,

$$\text{eff} = \frac{kQ}{1 + kQ + \left[\frac{1}{kQ} + 1\right]^2}$$

(4) For a given range of values of k, Figs. 4 and 5 determine the optimal coil reactance ($L\omega$) and the efficiency range.

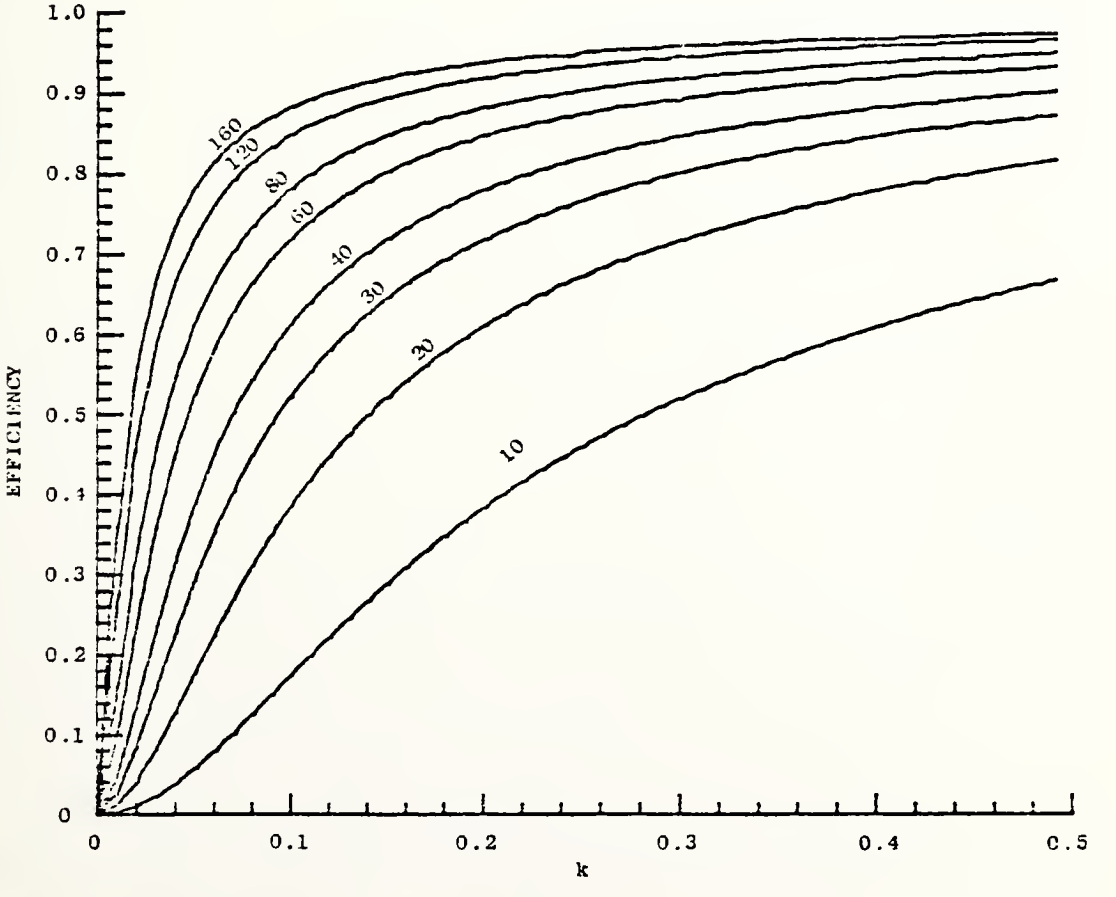

Fig. 6 EFFICIENCY VS COUPLING COEFFICIENT AS A FUNCTION OF COIL Q.

B. Maximizing Coil Q

To increase efficiency, Eq. (2.20), coil Q must be maximized. The following loss factors limit Q:

(1) dc coil resistance caused by copper losses

(2) ac coil resistance caused by nonuniform current distribution

(3) parasitic shunt capacitance that results in an apparent increase in ac resistance near coil self-resonance

(4) biological tissue losses

Biological tissue losses in low- and medium-frequency ($<$3 MHz) circuits are generally small compared to coil losses.

The dc coil resistance (R_{dc}) is merely a function of the conductor material, cross-section area, and length and sets the lower limit on the value of the ac coil resistance. For a given length of wire, R_{dc} can be reduced by increasing the cross-section area through the use of a larger diameter wire or a number of parallel wires.

The ac coil resistance is a complex function of many parameters. It depends on conductor size, coil size and configuration (such as number of turns per layer), and frequency. At radio frequencies, the magnetic flux in the conductor links the current in the center but does not link the current flowing near the surface. The inductance at the conductor center is then higher than at the surface, thereby causing the current to distribute itself near the surface. This nonuniform current distribution (called the "skin effect") decreases the effective cross-section area of the conductor and increases resistance [37].

Because the skin effect is caused by the magnetic flux in a conductor that results from ac currents, it cannot be predicted except in the simplest circuits. The skin effect associated with a straight round conductor

removed from all other conductors is predictable and sets a lower limit on the ac resistance for a given coil wound of that type of conductor. The ac resistance of a coil is always several times greater than that of a straight wire (the "proximity effect") because of the proximity of other conductors and their associated magnetic flux. Skin effect becomes significant at lower frequencies as the conductor diameter is increased. A fine wire exhibits this effect only in the high-frequency range, but its fineness also means high dc resistance. This problem can be partially solved by paralleling a number of fine separately insulated stranded wires called "litzendraht" (litz) wire. These coils will minimize losses and maximize coil Q in the power-transfer circuit.

Parasitic shunt capacitance causes power loss because it increases apparent coil resistance near the self-resonant frequency of the coil. The power-transfer coil is modeled by the simple RLC circuit in Fig. 7.

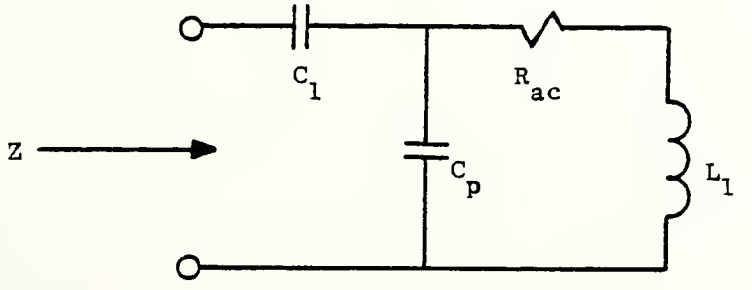

Fig. 7. MODEL OF SERIES-TUNED POWER-TRANSFER COIL WITH PARASITIC SHUNT CAPACITANCE AND ac RESISTANCE.

The complex coil impedance is

$$Z(j\omega) = \frac{R_{ac} + j\,[L_1\omega(1 - C_pL_1\omega^2) - C_pR_{ac}^2\omega]}{(1 - C_pL_1\omega^2)^2 + (C_pR_{ac}\omega)^2} - \frac{j}{C_1\omega} \qquad (2.21)$$

At $\omega^2 \approx (L_1C_1)^{-1}$, the imaginary part of Z equals zero; the real part is

$$\text{Re } Z(j\omega) \approx \frac{R_{ac}}{\left(1 - \frac{\omega^2}{\omega_{sr}^2}\right)^2} \tag{2.22}$$

where ω_{sr} is the coil self-resonant frequency, $1/(C_pL_1)^{1/2}$. Equation (2.22) is accurate only when ω is not close to ω_{sr}. At $\omega = 0.5\omega_{sr}$, the effective ac resistance is almost twice that of resistance without parasitic capacitance, and this apparent increase sets an upper limit on the frequency of the series-resonant circuit.

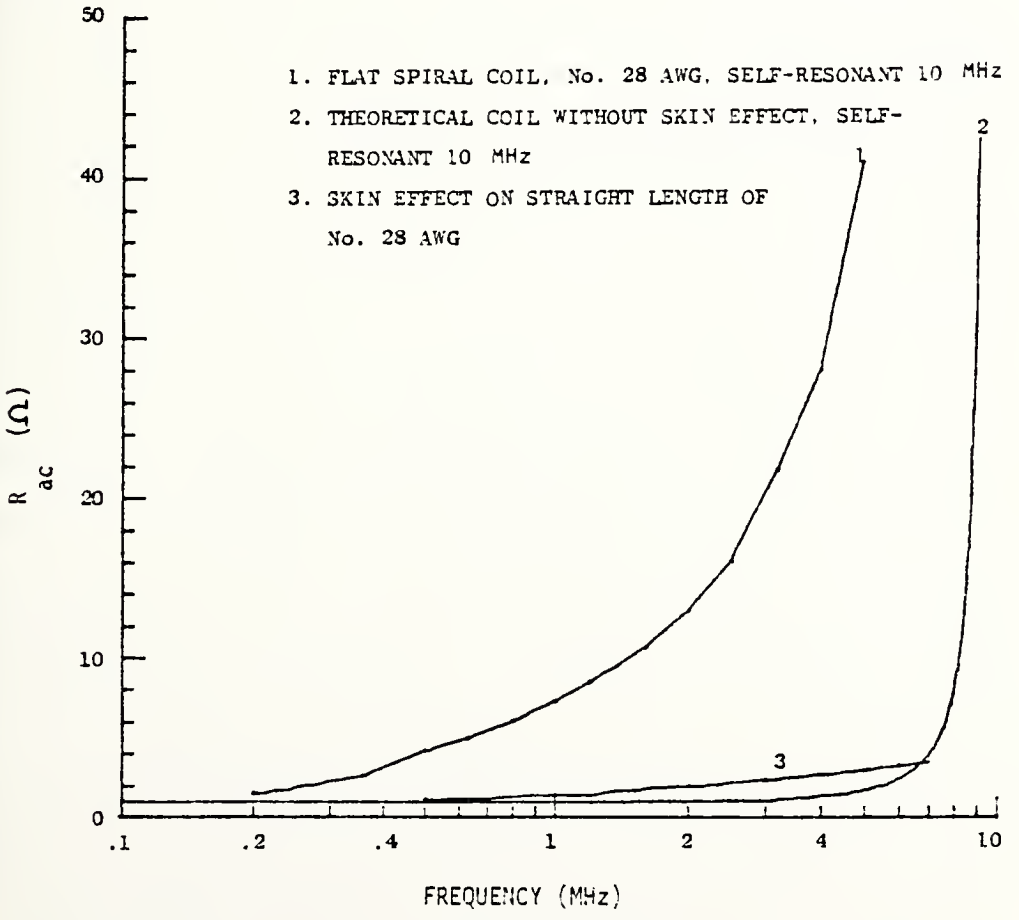

Fig. 8 ac RESISTANCE VS FREQUENCY. This plot demonstrates increases in ac resistance as a result of proximity effect (1), self-resonance (2) and skin effect (3).

Figure 8 illustrates how skin effect and parasitic capacitance increase ac resistance. A comparison of curves 1 and 2 indicates that increases in ac resistance at frequencies below 4 MHz are independent of coil self-resonance but are the result of skin effect. Curves 1 and 3 demonstrate the proximity effect. The ac resistance of the actual coil increases at approximately six times the rate of increase for the straight conductor. It can be seen that either skin effect must be minimized or higher frequencies must be avoided.

Additional information concerning the relationship between conductor size, coil configuration and ac resistance is plotted in Fig. 9. These curves are for five flat spiral coils wound with the copper conductor indicated. Curves 1 and 3 demonstrate the proximity effect and represent two coils of similar size and inductance but different winding configurations. Curve 1 plots a coil that has two turns/layer so that each turn is in proximity to five other turns; curve 3 is for a coil that has only one turn/layer so that each turn is in proximity to only two other turns. As a result, the proximity effect causes the ac resistance of the coil with two turns/layer to increase more rapidly than the coil with one turn/layer. While the ac resistance of the one turn/layer coil increases at approximately six times that for a straight conductor, the ac resistance of the two turns/layer coil increases at nine times the rate for a straight conductor. Curves 2 and 4 demonstrate the proximity effect for a smaller wire and, when compared to curves 1 and 3, they also illustrate how a smaller wire reduces skin and proximity effects. Note that curves 3 and 4 cross at approximately 800 kHz. In the absence of the proximity effect (a straight conductor removed from other conductors), the larger conductor

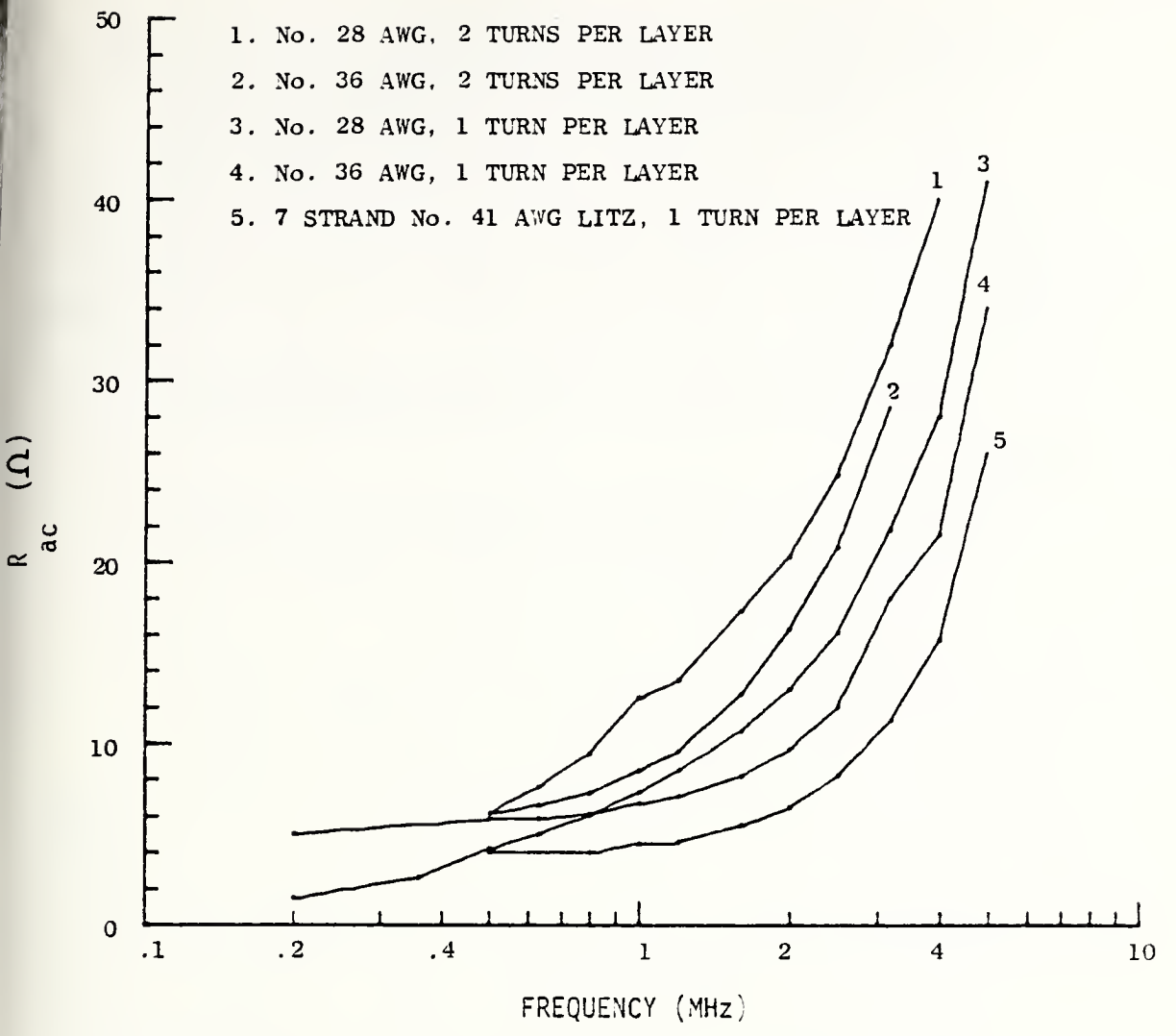

Fig. 9. ac RESISTANCE VS FREQUENCY FOR SIMILAR FLAT SPIRAL COILS WOUND WITH VARIOUS SIZE WIRES.

always has the lower ac resistance. As a result, the cross of curves 3 and 4 indicates the presence of the proximity effect and the proximity effect becomes more pronounced as the conductor size increases. Curve 5, representing a litz-wire coil, shows the improvement possible over single conductors in maintaining a low value of ac resistance up to reasonably high frequencies.

Figures 8 and 9 contain the following information:

(1) Skin and proximity effects increase coil ac resistance to several times the dc resistance value.

(2) Operation near the coil self-resonant frequency greatly decreases the efficiency of the series-tuned circuit.

(3) Coil losses are minimized by the use of fine-stranded litz wire.

No single frequency is better than another for maximizing power-transfer efficiency. The frequency used depends on the following factors:

(1) Tissue losses -- as frequency increases so do tissue losses; however, below 3 MHz, such losses account for less than 1% inefficiency.

(2) Information band -- transfer of power within the sensor information band severely distorts information accuracy. A buffer band of frequencies is required between the power-transfer frequency and the information band.

(3) Sensor size -- high efficiency at low frequencies requires large coils to achieve high Q. If the sensor is small, the coil must also be small to be size compatible. For small coils, high frequencies are needed to maintain maximum power-transfer efficiency.

Equation (2.20) states that power-transfer efficiency depends only on the circuit coupling coefficient (k) and coil Q. The coupling coefficient is not a function of frequency, as is Q. As frequency becomes greater, Q increases because $Q = L\omega/R_{ac}$. At some frequency, however, R_{ac} increases more rapidly than ω and Q begins to decrease. It is difficult to predict theoretically the frequency of maximum Q from the physical characteristics of the coil because of the skin and proximity effects. In the absence of these effects, parasitic capacitance and coil self-resonance limit the useful upper frequency.

Section A details the selection of coil reactance for achieving maximum efficiency for a given load resistance. After the approximate operating frequency is selected based on the above factors, the coils are wound and then tested to determine the frequency of maximum Q by means of a standard Q-meter to measure Q as a function of frequency. A plot of Q vs frequency

results. Figure 10 is an example of such a plot for three litz-wire coils of similar size but a different number of turns. This plot indicates the frequency of maximum Q and demonstrates that Q is near maximum over a reasonably wide range of frequencies; also marked are the self-resonant frequencies of the coils. In each case, Q_{max} occurs at approximately $0.25\omega_{sr}$ and generally between 0.1 and $0.4\omega_{sr}$. When the skin and proximity effects are absent, the upper frequency is fixed in a predictable manner. The coil ac resistance is altered only by the parasitic capacitance and, as a function of frequency, is

$$R_{ac} = \frac{R_{dc}}{[\ 1 - (\omega^2/\omega_{sr}^2\ )\ ]^2} \tag{2.23}$$

which is similar to Eq. (2.22).

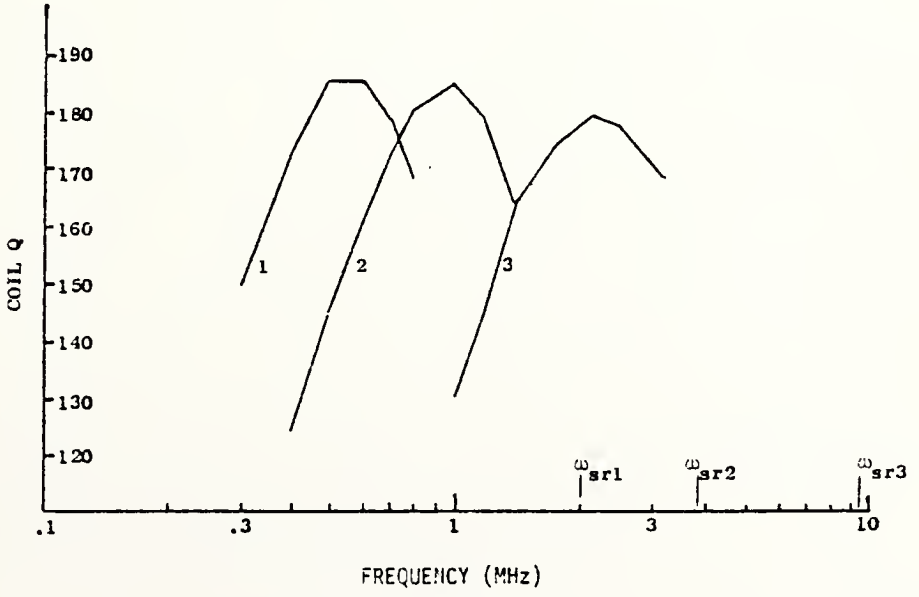

Fig. 10. COIL Q VS FREQUENCY FOR FOUR LITZ-WIRE COILS SHOWING THE RELATIONSHIP BETWEEN ω_{sr} AND FREQUENCY OF MAXIMUM Q.

results. Figure 10 is an example of such a plot for three litz-wire coils of similar size but a different number of turns. This plot indicates the frequency of maximum Q and demonstrates that Q is near maximum over a reasonably wide range of frequencies; also marked are the self-resonant frequencies of the coils. In each case, Q_{max} occurs at approximately $0.25\omega_{sr}$ and generally between 0.1 and $0.4\omega_{sr}$. When the skin and proximity effects are absent, the upper frequency is fixed in a predictable manner. The coil ac resistance is altered only by the parasitic capacitance and, as a function of frequency, is

$$R_{ac} = \frac{R_{dc}}{[\ 1 - (\omega^2/\omega_{sr}^2\ )\ ]^2} \tag{2.23}$$

which is similar to Eq. (2.22).

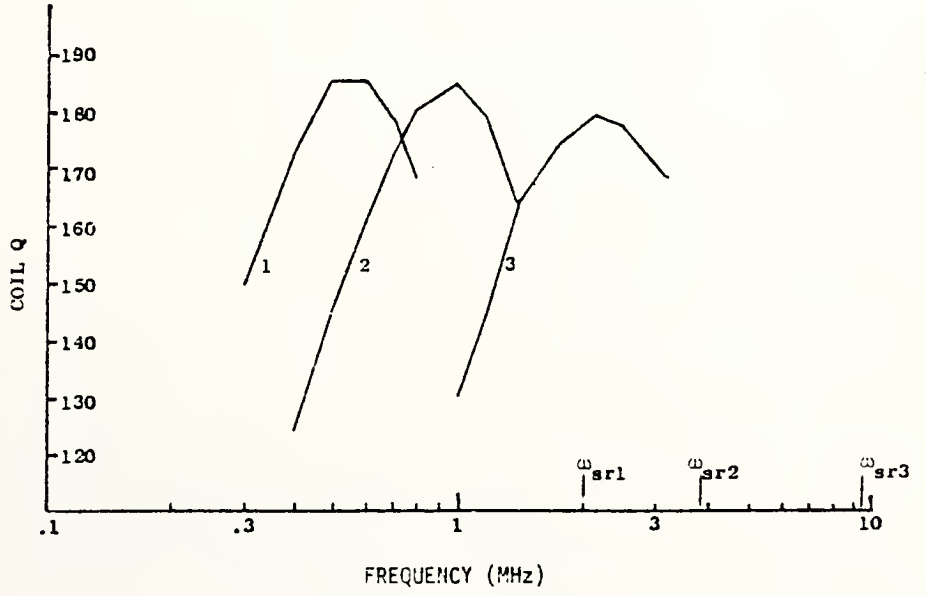

Fig. 10. COIL Q VS FREQUENCY FOR FOUR LITZ-WIRE COILS SHOWING THE RELATIONSHIP BETWEEN ω_{sr} AND FREQUENCY OF MAXIMUM Q.

For $\omega/\omega_{sr} < 0.5$, the denominator of Eq. (2.23) is approximated by $[\ 1 - 2(\omega/\omega_{sr})^2\ ]$. The Q of a coil not subject to skin or proximity effects is defined by

$$Q = \frac{L\omega}{R_{dc}} [\ 1 - 2(\frac{\omega}{\omega_{sr}})^2\ ] \qquad (2.24)$$

The maximum Q as a function of frequency is found by differentiating Eq. (2.24) with respect to ω. The result is that, at Q_{max},

$$\omega = \sqrt{\frac{\omega_{sr}^2}{6}} \approx 0.4\omega_{sr}$$

which sets an absolute upper limit on the operating frequency of any coil. Because of skin and proximity effects, the actual frequency limit is always less than $0.4\omega_{sr}$; this is supported by Fig. 10 where Q_{max} occurs at approximately $0.25\omega_{sr}$ for all three coils.

In Fig. 9, the proximity effect was demonstrated by comparing the ac resistance of two similar coils. For standard wire coils, those with one turn/layer were observed to have a lower R_{ac} and a higher Q than those with multiple turns/layer. The three litz-wire coils whose Q's are plotted vs frequency in Fig. 10 all achieved approximately the same maximum value of Q. These coils are similar in size but have one, two and four turns per layer. The conclusions to be drawn are that litz wire is very effective in minimizing the proximity effects and that multiple turns per layer are not detrimental to coil Q if this type of wire is used.

C. Maximizing Coil Coupling

Power and information transfer between an external and a subcutaneous coil is possible because of the mutual inductance between the two coils.

Because efficiency increases as mutual inductance increases, the design of a transcutaneous power and information system should include guidelines to maximize mutual inductance. The coupling between two coils depends on their size, the distance between them, their orientation, and the magnetic permeability of the medium that connects them. The size of the subcutaneous coil is determined by the subcutaneous physiological sensor; it should be as large as possible but still remain size-compatible with the sensor. The separation between the two coils is determined by the thickness of the tissue and the layers of material used to insulate the coil from its environment. The coil and sensor are enclosed in a thin plastic shell and encapsulated first in a special wax and then in medical-grade silastic. Because the thickness of these three layers (plastic, wax and silastic) normally does not exceed 3 to 5 mm, the separation between the external and subcutaneous coils is equal to the tissue thickness plus 3 to 5 mm; this usually does not exceed 15 mm.

For flat spiral coils, optimal mutual inductance for a given size and separation is achieved when the coils are arranged coaxially. For maximum efficiency, therefore, the external coil must be placed accurately over the implanted coil. The subcutaneous coil operates like an air-core coil because the magnetic permeability of tissue is approximately unity; therefore, the medium surrounding it does not permit the use of a complete magnetic circuit of ferrite or iron as found in most transformers. Some researchers [10, 31, 25] report using ferrite cores with one or both coils; however, no study is available that indicates that such cores consistently improve power-transfer efficiency. Such improvement must be weighed against increased subcutaneous coil volume which becomes a significant factor when the system is intended to power subminiature integrated-circuit physiological sensors.

The mutual inductance between two coaxial coils is derived from the equation for the mutual inductance between two coaxial circles developed by Maxwell [38],

$$M_o = 4\pi\mu_r\sqrt{r_1 r_2}\left[\left(\frac{2}{h} - h \right) F - \frac{2}{h} E \right] \text{ nH} \qquad (2.25)$$

where

μ_r = relative magnetic permeability

r_1, r_2 = radii of the circles (in centimeters)

$$h = \frac{2\sqrt{r_1 r_2}}{\left[(r_1 + r_2)^2 + d^2 \right]^{1/2}}$$

d = distance between the circles (in centimeters)

F, E = complete elliptic integrals of the first and second kind, respectively

The integrals are determined by the infinite series,

$$F = \frac{\pi}{2}\left[1 + \left(\frac{1}{2} \right)^2 h^2 + \left(\frac{1\cdot 3}{2\cdot 4} \right)^2 h^4 + \left(\frac{1\cdot 3\cdot 5}{2\cdot 4\cdot 6} \right)^2 h^6 + \ldots \right] \qquad (2.26a)$$

$$E = \frac{\pi}{2}\left[1 - \left(\frac{1}{2} \right)^2 h^2 - \left(\frac{1\cdot 3}{2\cdot 4} \right)^2 \frac{1}{3} h^4 - \left(\frac{1\cdot 3\cdot 5}{2\cdot 4\cdot 6} \right)^2 \frac{1}{5} h^6 - \ldots \right] \qquad (2.26b)$$

The mutual inductance between two coils is then

$$M = M_o n_1 n_2 \qquad (2.27)$$

where n_1 and n_2 are the turns per coil.

When the ratio of the spacing between the coils to the coil cross-section dimensions is small, it is necessary to compute several values

of M_o and then average them. Figure 11 is an example of such an arrangement, where the average mutual inductance between the circles at locations 1, 2, 3 and 4 is

$$M_o = \frac{1}{4}(M_{13} + M_{14} + M_{23} + M_{24}) \tag{2.28}$$

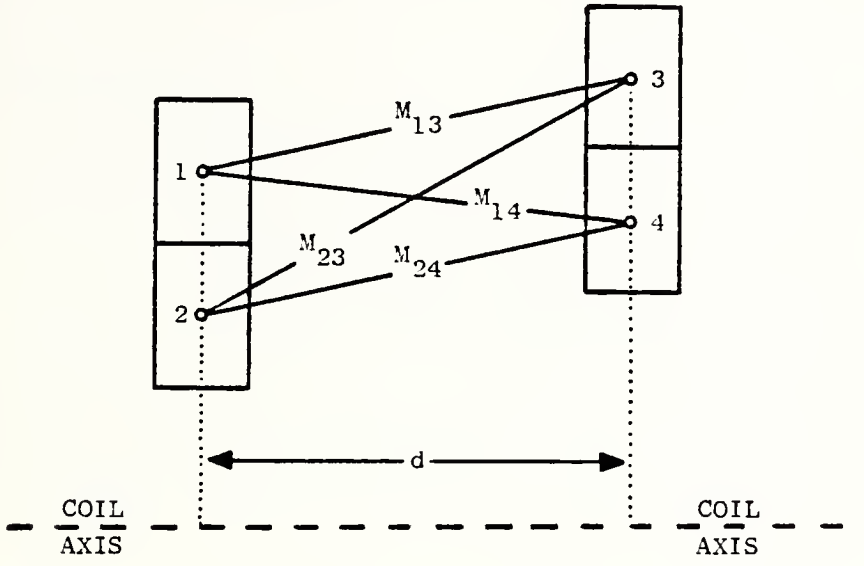

Fig. 11. CROSS SECTION OF TWO CLOSELY SPACED COAXIAL COILS. Circles for computing M_o are located at 1, 2, 3 and 4.

For large values of d, the difference between any two values of M becomes negligible, and M_o is approximately calculated by using only two circles -- one at the center of each coil cross section. Because M depends on the number of turns of the two coils, it is easier to calculate in terms of the ratio between M and the geometric mean of the inductances of the two coils. This ratio is called the coupling coefficient and is defined as

$$k = \frac{M}{(L_1 L_2)^{1/2}} \tag{2.29}$$

The inductance of a flat spiral or short solenoid coil is directly related to its mean radius and to the square of the number of turns. If

its cross-section dimensions are small compared to its mean radius, the coil inductance is approximated by Stefan's formula [39],

$$L = 4\, n^2 \mu_r r\, [\, \log_e (8r/s) - y\,]\ \text{nH} \qquad (2.30)$$

where

- n = number of turns
- r = coil mean radius (in centimeters)
- s = diagonal of winding cross section (in centimeters)
- y = constant related to winding geometry ($y = 0.6$ for flat spirals and $y = 0.8$ for square cross sections)

By combining Eqs. (2.25), (2.29) and (2.30), the following expression for the coupling coefficient is obtained,

$$k = \frac{(2/h - h)\, F - (2/h)\, E}{\sqrt{[\, \log_e (8r_1/s_1) - y_1\,]\, [\, \log_e (8r_2/s_2) - y_2\,]}} \qquad (2.31)$$

where k is a function of two ratios -- the ratios between coil radii and spacing and between coil radii and winding diagonal. A plot of k vs coil separation facilitates the estimation of the coupling coefficient; it is constructed by assuming that the cross-section diagonals of the external and implanted coil are approximately the same ($s_1 \approx s_2$). Figure 12 is a plot of the maximum coupling coefficient vs the coil spacing to implanted coil radius ratio. This plot was developed in terms of the implanted coil size because the maximum value of k is a function of d and the ratio between r_1 and r_2. As the coil spacing widens, the external coil increases in size to achieve maximum coupling. This factor was considered when plotting Fig. 12 as was the fact that, as r_1 (for the external coil)

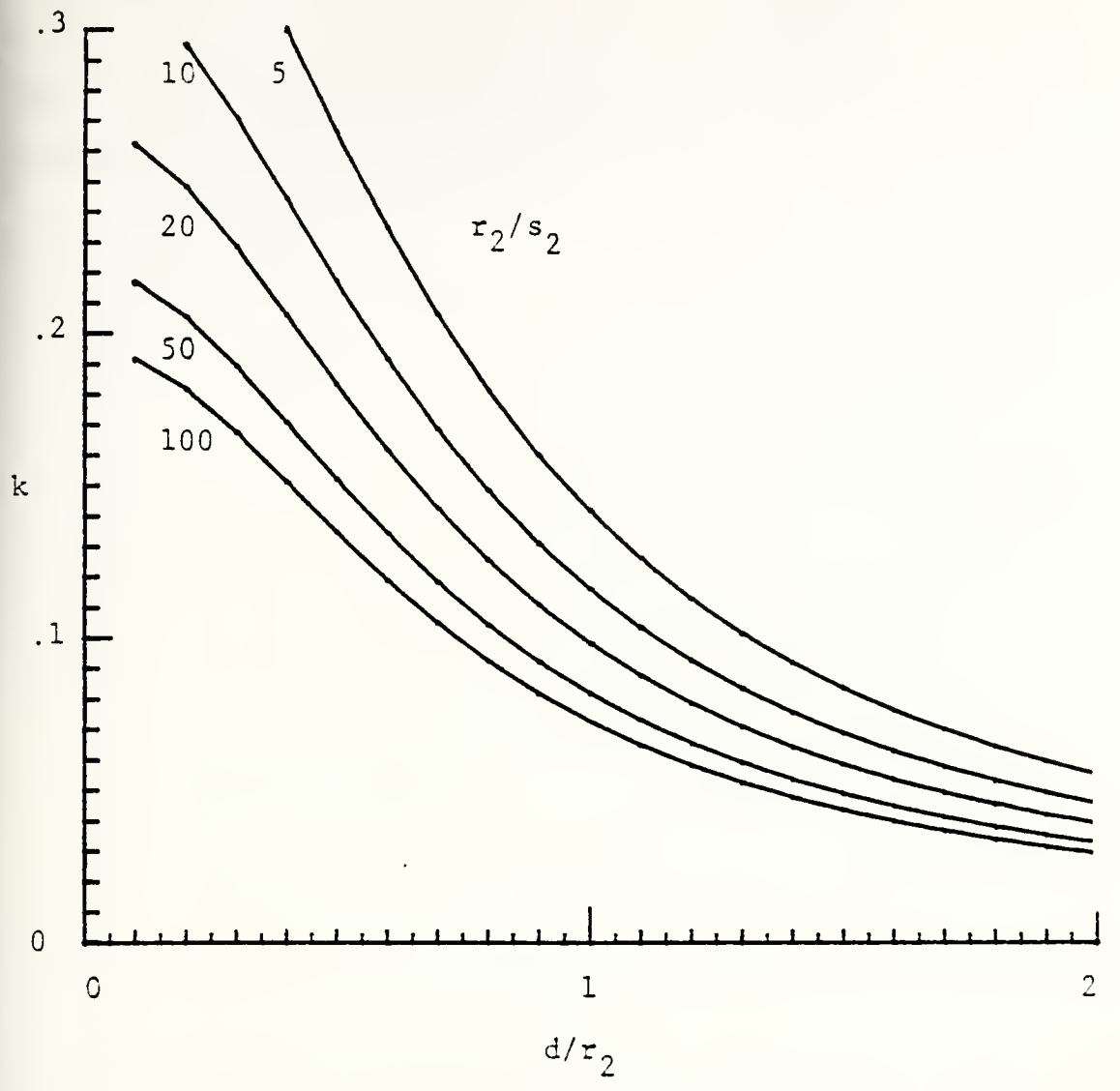

Fig. 12. MAXIMUM COUPLING COEFFICIENT VS COIL SPACING TO IMPLANTED COIL RADIUS (d/r_2) AS A FUNCTION OF IMPLANTED COIL RADIUS TO COIL CROSS-SECTION DIAGONAL (r_2/s_2).

increases, L_1 increases. Figure 13 plots the optimal ratio between external- and implanted-coil sizes (r_1/r_2) vs coil separation (d/r_2) for maximum k.

From a knowledge of the implanted sensor size the size of the implanted (subcutaneous) coil is determined. The physiological application of the sensor and its location determine the expected spacing between external and implanted coils. From the implanted coil size and the expected spacing,

the proper external coil size and the maximum coupling coefficient can be determined using Figs. 13 and 12, respectively.

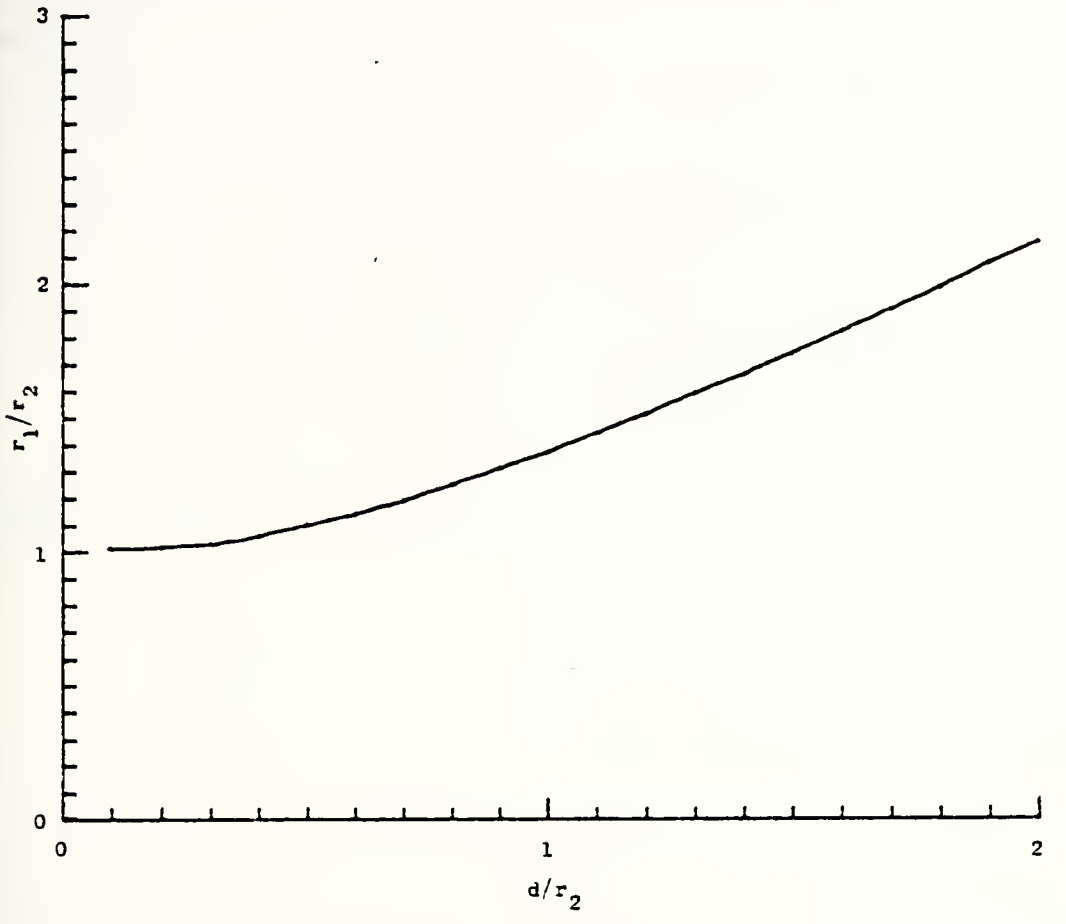

Fig. 13. RATIO OF COIL RADII FOR MAXIMUM COUPLING COEFFICIENT VS RATIO OF COIL SPACING TO COIL RADIUS.

The above analysis is based on the approximation that the power-transfer coils are represented by single-turn coils located at the center of the cross section of the actual coil. To study the extent to which cross-section dimensions affect coupling and power-transfer efficiency, Eqs. (2.25) and (2.28) were used to analyze some representative coils.

At various spacings, these dimensions were changed and the resulting coupling coefficient computed. The mean radii were held constant at values determined in Fig. 13. From a series of such computations at different spacings and number of turns, the following guidelines were developed.

(1) The closer the coils are spaced, the more critical is the cross-section geometry.

(2) When the spacing between coils is large and the coupling coefficient is small ($k < 0.05$), the cross-section geometry has negligible effect on k.

(3) As coil coupling increases and spacing decreases, the cross-section geometry moves from a thin rectangle (flat spiral) toward a square (short solenoid).

It can be seen in Fig. 14 that, although optimal coil cross-section geometries exist to maximize the coupling coefficient, the actual percent

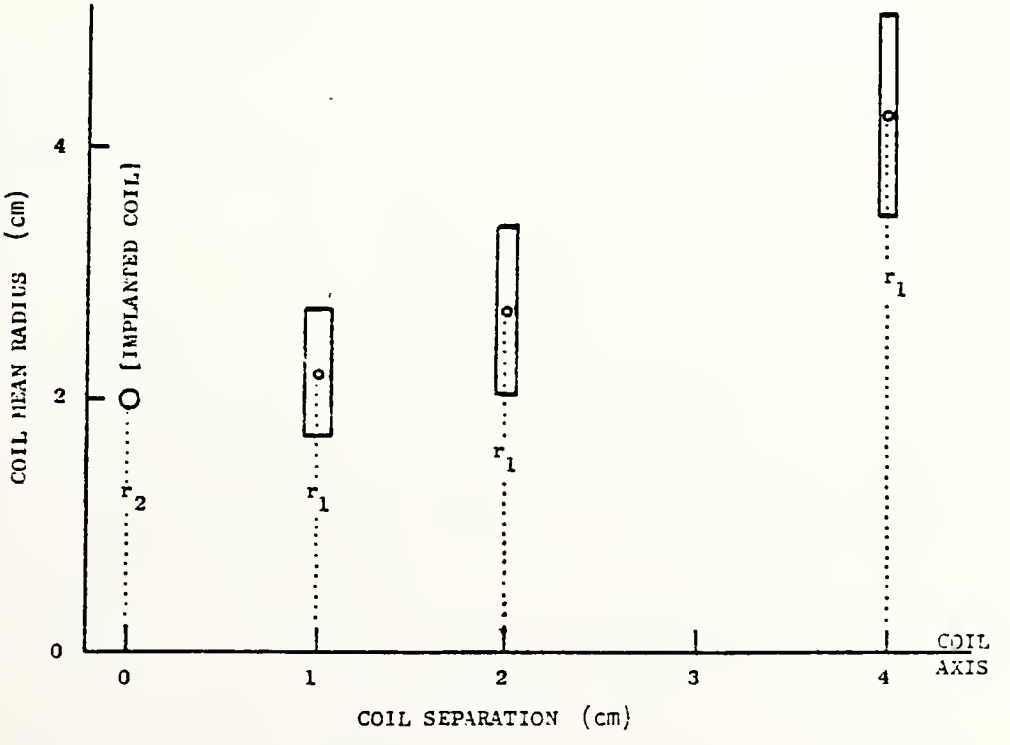

Fig. 14. COIL CROSS-SECTION GEOMETRY AS A FUNCTION OF COIL SEPARATION.

improvement over a one turn/layer flat spiral is not large. In the cases calculated, the difference between the coupling coefficient of a one turn/layer flat spiral coil and a coil with the optimal cross-section geometry is less than 5%.

D. Experiments and Conclusions

The equations and figures in the above sections can be verified by simple experiments. Three coils are wound on acrylic plastic forms with No. 40 AWG wire. The measured coil parameters are

L_1, L_2: mean coil radius (r_2) = 20 mm
winding diagonal (s) = 1.1 mm
inductance = 1360 μH

L_3 : mean coil radius (r_1) = 27 mm
winding diagonal (s) = 1.1 mm
inductance = 1367 μH

At a coil separation (d) of 19 mm,

$$\frac{d}{r_2} = \frac{19}{20} = 0.95$$

From this and Fig. 13, the optimal r_1/r_2 ratio to maximize k is 1.35, or r_1 = 27 mm. At d = 19 mm, the coupling coefficients between L_1 and L_3 and then L_1 and L_2 are measured. The following results support the selection of r_1 = 27 mm to maximize k:

$$k_{L_1L_2} = 0.12 \qquad k_{L_1L_3} = 0.14$$

The ratio between r_2 and s_2 is 20/1.1 = 18. At d/r_2 = 0.95 and r_2/s_2 = 18,

Figure 12 gives the expected value of k at approximately 0.11 which is close to the measured value.

The power-transfer efficiency of L_1 and L_3 is next measured. The optimal load resistance is $kL\omega$. At 500 KHz,

$$R_{L\ opt} = (0.14)(1360\ \mu H)(500\ kHz)2\pi = 590\Omega$$

For this load, the measured circuit input resistance is 755Ω. Voltage measurements yield V_{in} = 7.22 V and V_{out} = 5.19 V, and the resulting efficiency is 67%. The measured values of coil Q at 500 kHz are 40 for L_1 and 31 for L_2. The geometric mean Q is

$$Q = \sqrt{(40)(31)} \approx 35$$

With Q = 35 and k = 0.14, Fig. 6 is used to estimate efficiency, and the result is 67% which agrees with the measured value and supports the validity of Eq. (2.20). Litz wire would raise efficiency by increasing coil Q. At higher coil Q's (>100), high-Q tuning capacitors should be used -- typically silver-mica or variable mica.

The following conclusions are drawn from the study described in this chapter.

(1) Transcutaneous power tranfer is a practical means of powering implanted electronic sensors.

(2) Definite guidelines are established for maximizing power-transfer efficiency.

(3) A properly designed and applied power-transfer circuit is capable of efficiencies as high as 90%.

Chapter III

LOW-VOLTAGE REGULATOR DESIGN

This chapter investigates voltage regulator design to maximize power efficiency at low-output voltages. The regulator is intended to power subcutaneous physiological sensors and to operate as a replacement for batteries. It will be designed for monolithic fabrication so as to be size-compatible with current and future miniature implantable integrated-circuit sensors.

The most commonly used battery is the mercury cell with a nominal output of 1.35 V; two of these cells are generally arranged in series for a supply voltage of 2.7 V. Power efficiency at such a low output requires a special circuit design.

The regulator is also designed for temperature stability. This is not a critical factor after the regulator has been implanted because body temperature is stable; however, certain systems are calibrated at room temperature before implant. Calibration often depends on supply voltage and, in these cases, the output-voltage variation with temperature must be minimized.

A. Limits to Efficiency

Voltage regulators are usually designed for outputs greater than 5 V and for operation from line power. Under such conditions, efficiency is often reasonable but of little importance. If the output is reduced to the 1 to 3 V range and the primary source of power is batteries, inefficiency and battery life become significant. The key to efficiency is minimizing the voltage drop across the regulator. Figure 15 is a block diagram of a basic series pass voltage regulator, where the difference

between V_{in} and V_{out} is defined as ΔV. Assuming $I_{out} \approx I_{in}$, efficiency becomes

$$eff = \frac{V_{out}}{\Delta V + V_{out}} \tag{3.1}$$

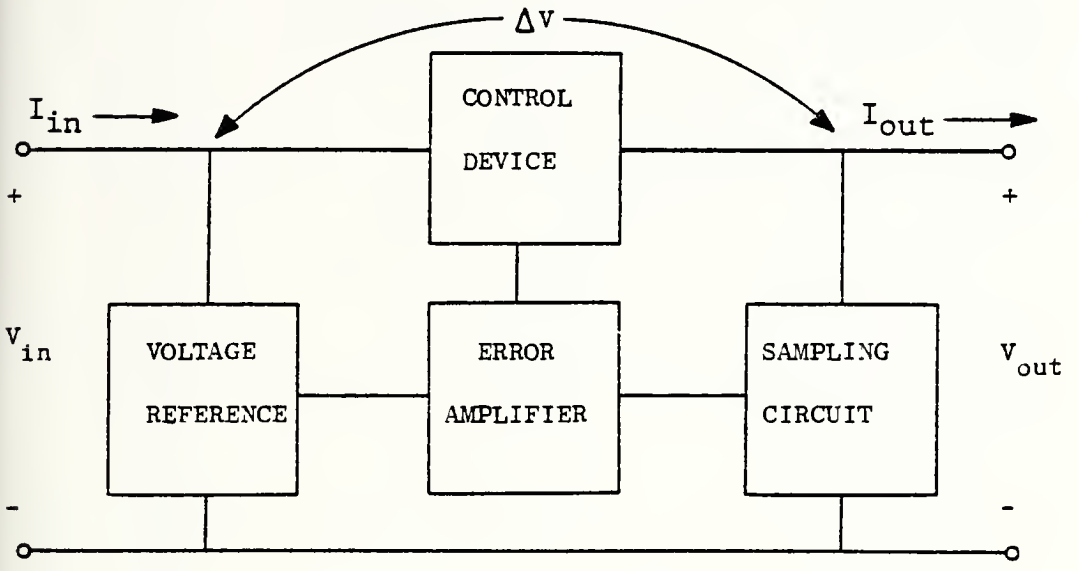

Fig. 15. BLOCK DIAGRAM OF A BASIC SERIES PASS VOLTAGE REGULATOR.

The need to minimize ΔV to achieve higher efficiency at low-output voltages is demonstrated in Fig. 16 where it can be seen that, at low-output voltages, ΔV affects efficiency significantly.

The two potential sources of inefficiency are the control circuit and the voltage reference. Any voltage drop required by the control circuit immediately limits the minimum value of ΔV. The reference has a minimum operating voltage that affects efficiency indirectly by limiting the minimum value of V_{in} and, therefore, ΔV. To achieve greater efficiency, the control circuit must be capable of passing 10 to 50 mA with voltage drops of less than 1 V. The voltage reference must be able to

operate from a low voltage (<2 V), be temperature stable, and require very little current (<500 μA).

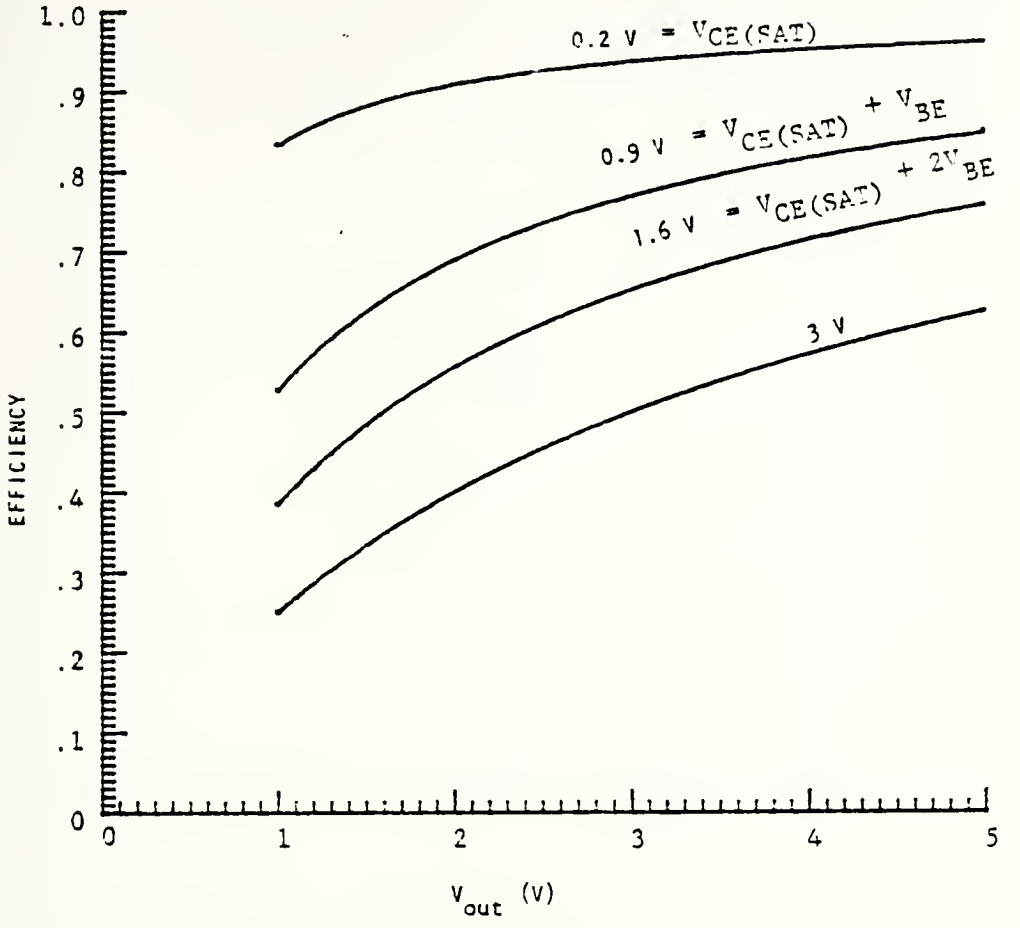

Fig. 16. EFFICIENCY VS VOLTAGE-REGULATOR OUTPUT AS A FUNCTION OF ΔV.

B. Voltage Reference

Two standard types of temperature-stable voltage references are used in monolithic regulators. The first is based on a temperature-compensated zener diode [40]. This is a relatively noisy circuit and it requires an input voltage of 7 to 9 V and tight process control for good stability. The second makes use of the positive temperature coefficient of the emitter-base junction voltage differential of two transistors

operating at different current densities [41]. The stable reference produced is 1.2 V; however, the circuit is relatively complex, requires good process control, and operates best above 0.5 mA. It also tends to produce unstable oscillations under certain load and current conditions.

Figure 17 is a schematic of an alternative reference that is a less complex circuit and operates at low current. The constant-current

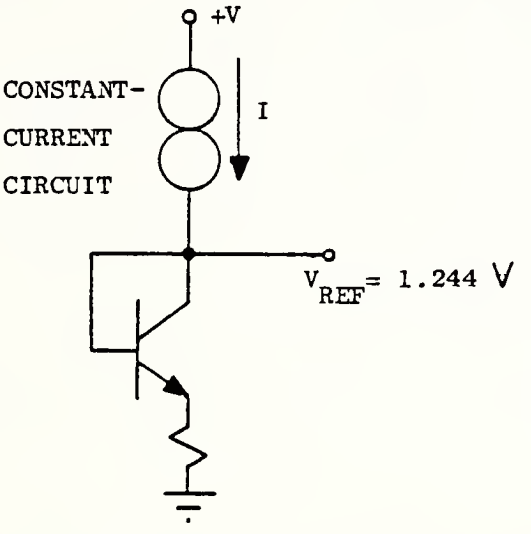

Fig. 17. TEMPERATURE-STABILIZED LOW-VOLTAGE REFERENCE CIRCUIT.

circuit in the reference has the following key characteristics: (1) operation at a single-controlled value as low as 10 μA, (2) high dynamic resistance -- greater than 20 MΩ, and (3) a well-defined positive temperature coefficient. The operation of this circuit can best be understood by examining Fig. 18. Half of the circuit is a modified Wilson current mirror. The addition of R_E and n parallel transistors produces an input-output current relationship with one point at which $I_1 = I_2$, as shown by the curve that crosses the $I_1 = I_2$ line. Combining this n-p-n circuit with a similar p-n-p circuit (Fig. 19), yields a constant-current circuit that operates at a single current level because there is only one value

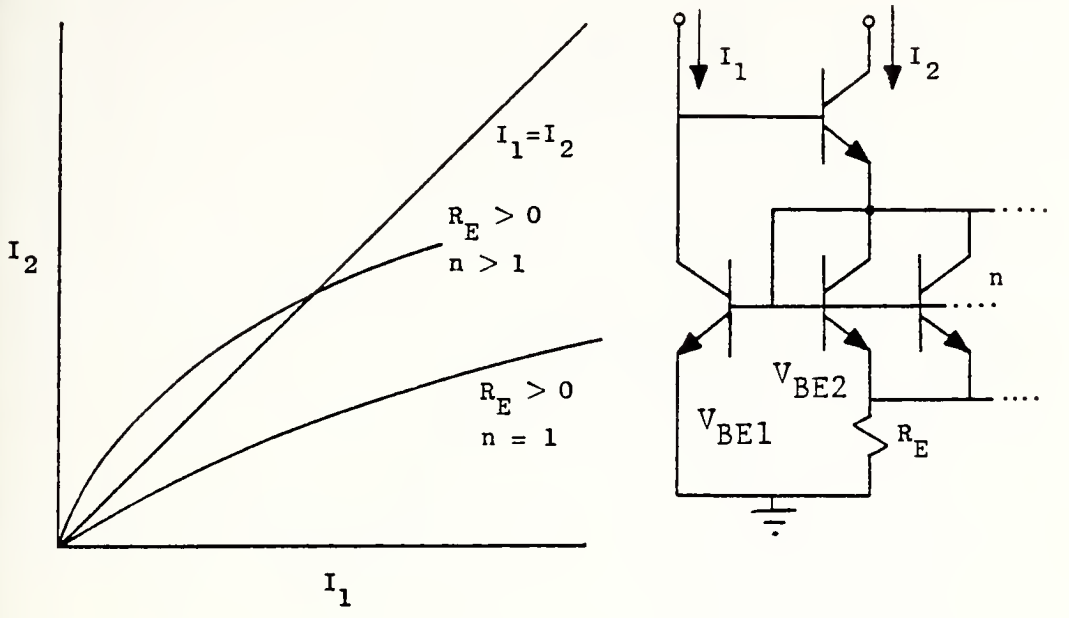

Fig. 18. MODIFIED WILSON CURRENT MIRROR AND I_1 VS I_2 FOR DIFFERENT CONDITIONS.

of I_1 and I_2 (other than zero) at which operation is stable. This current value is controlled by n and by the size of R_E; it can be determined by considering Fig. 18. The voltage around the loop produces

$$V_{BE1} = V_{BE2} + I_2 R_E \tag{3.2}$$

if all transistors are assumed to be identical and have reasonable betas. The basic diode equation yields

$$V_{BE1} = \frac{kT}{q} \log_e \frac{I_1}{I_s} \tag{3.3a}$$

and

$$V_{BE2} = \frac{kT}{q} \log_e \frac{I_2}{nI_s} \tag{3.3b}$$

Combining these equations results in

$$I_2 = \frac{kT}{q} \log_e \frac{nI_1}{I_2} \tag{3.4}$$

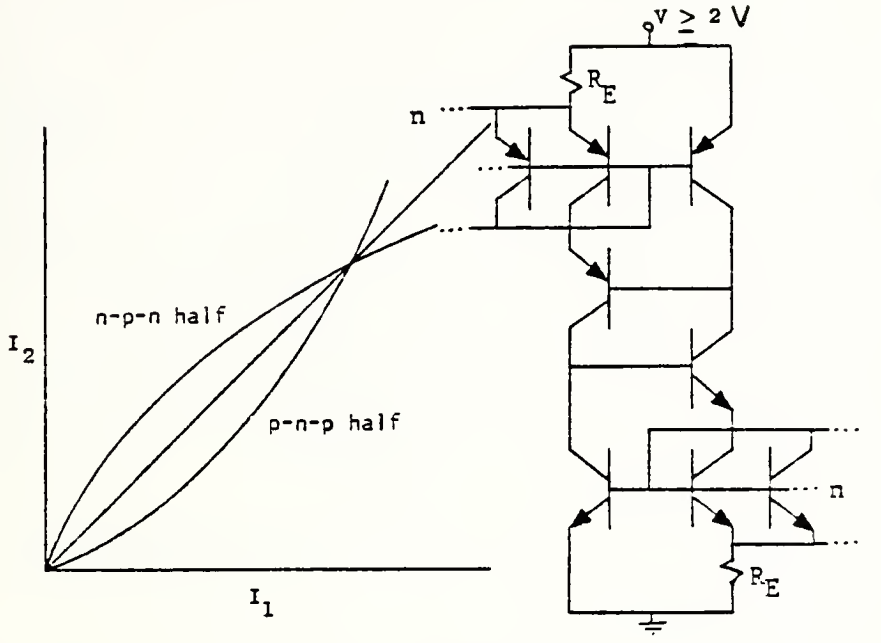

Fig. 19. CONSTANT-CURRENT CIRCUIT AND I_1 - I_2 CHARACTERISTIC.

If both halves of the circuit have the same n and R_E, then $I_1 = I_2$ and the total current is

$$I = I_1 + I_2 = \frac{2kT}{qR_E} \log_e n \tag{3.5}$$

Dynamic resistance can be calculated by an analysis of one of the two halves of the circuit. From the literature [42], the output resistance of the Wilson current mirror is

$$R_{out} \approx \frac{B_1 r_{o1}}{4} \tag{3.6}$$

for the parameters shown in Fig. 20 and with $R_E = 0$, $n = 1$, and $R_s \longrightarrow \infty$.

A more detailed analysis reveals that Eq. (3.6) is correct only when $R_s \gg r_\pi$. For $R_E > 0$ and $n > 1$, the output resistance is

$$R \approx \frac{B_1 r_{o1}}{2} \left(\frac{1 + R_E n g_{m3}}{2 + R_E n g_{m3}} \right) \qquad (3.7)$$

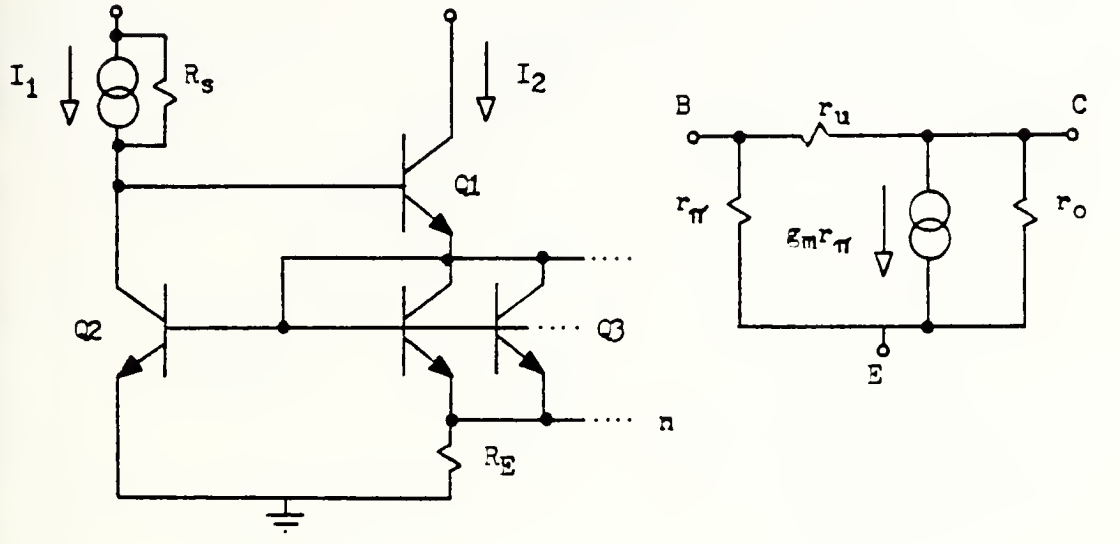

Fig. 20. MODIFIED WILSON CURRENT MIRROR AND HYBRID-π TRANSISTOR MODEL.

The addition of R_E increases the output resistance by 20% to 50%, depending on n. It is interesting to note that the circuit output resistance depends primarily on the characteristics of Q_1 when the betas of Q_2 and Q_3 are greater than 30. Typically, for the n-p-n half of the circuit, R_{out} = 100 MΩ ; for the p-n-p half, using lateral devices, R_{out} = 10 MΩ. The total circuit has an output resistance of approximately twice that of the p-n-p half. In Fig. 21, the curves of I_1 vs I_2 for the n-p-n and p-n-p halves are plotted for two values of V_{CE}. Because the n-p-n half has high dynamic resistance ($\approx$ 100 MΩ), its I_1 vs I_2 relationship exhibits little change with voltage; because the p-n-p half has lower

resistance its I_1 vs I_2 relationship changes more rapidly. The result is a shift in the actual operating point from point 1 to point 2 caused by

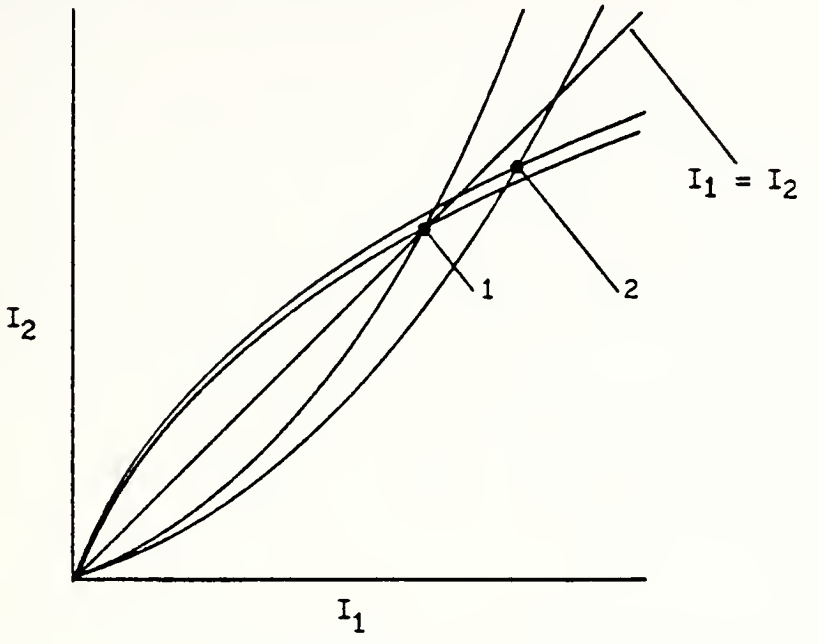

Fig. 21. I_1 VS I_2 FOR BOTH THE P-N-P AND N-P-N CIRCUITS AT TWO VALUES OF V_{CE}.

the increase in the values of I_1 and I_2. The total current is $I = I_1 + I_2$. A percent change in I_1 or I_2 produces a percent change in I. Because $I_1 \approx I_2$, a percent change in either current causes a percent change in I of one-half that amount; that is, if a variation in V_{CE} results in a rate of change to I_1 proportional to a resistance of 10 MΩ, then I varies at a rate proportional to 20 MΩ, assuming the rate of change of I_2 is proportional to a resistance large compared to 10 MΩ. This actually occurs in a constant-current circuit where total resistance is approximately twice the output resistance of the p-n-p half of the circuit ($\approx$ 20 MΩ).

Temperature stability is a function of the actual reference-voltage level. From Fig. 17, the reference voltage is

$$V_{ref} = V_{BE} + IR_1 \tag{3.8}$$

Substituting Eq. (3.5) for I produces

$$V_{ref} = V_{BE} + \frac{2kTR_1}{qR_E} \log_e n \tag{3.9}$$

To determine the value of V_{ref} for a zero temperature coefficient, Eq. (3.9) is differentiated with respect to T,

$$\frac{\Delta V_{ref}}{\Delta T} = \frac{\Delta V_{BE}}{\Delta T} + \frac{2kR_1}{qR_E} \log_e n \tag{3.10}$$

From the literature [43],

$$V_{BE} = V_{go}\left(1 - \frac{T}{To}\right) + V_{BEo}\left(\frac{T}{To}\right) + \frac{mkT}{q} \log_e\left(\frac{T}{To}\right) \tag{3.11}$$

where

V_{go} = silicon energy band-gap voltage (1.205 V)

V_{BEo} = V_{BE} at T_o

m = constant dependent on transistor fabrication (approximately 1.5 for monolithic transistors)

At $T = T_o$,

$$\frac{\Delta V_{BE}}{\Delta T} = \frac{-V_{go}}{T_o} + \frac{V_{BEo}}{T_o} - \frac{1.5k}{q} \tag{3.12}$$

which substituted into (3.10) and set equal to zero results in

$$V_{BEo} + \frac{2kT_o R_1}{qR_E} \log_e n = V_{go} + 1.5 \frac{kT_o}{q} \tag{3.13}$$

The left-side of Eq. (3.13) is V_{ref} at $T = T_o$ from Eq. (3.9). At $T_o = 300°K$,

$$V_{ref} = V_{go} + \frac{1.5kT_o}{q} = 1.244 \text{ V} \tag{3.14}$$

If R_1 and I are adjusted to produce a V_{ref} of 1.244 V, then V_{ref} is stable with temperature to a first approximation. Reference voltages equal to integer multiples of 1.244 V can be obtained by arranging a number of diode-connected transistors in series.

This reference circuit was constructed from discrete components with $n \approx 2$ and $R_E = 316\Omega$; R_1 was adjusted to produce $V_{ref} = 1.248$ V at 26°C. Care was taken to ensure that the resistors had very stable temperature characteristics. At 100°C, V_{ref} increased to 1.253 V which is a change of 56 ppm/°C. The measured dynamic resistance was 60 MΩ for a current of 100 μA; this was high because the discrete p-n-p devices were not lateral transistors.

The reference circuit can also be fabricated in monolithic form. The advantages of this type of fabrication are close transistor matching (n can be made greater than 2) and close thermal coupling so that thermal gradients between transistors cause minimum circuit imbalance. For normal processing variations, circuit stability with temperature can be determined as a function of n (the number of parallel transistors). Figure 22 is a plot of a set of typical- and worst-case processing variations with the following parameter tolerances:

Parameter	Typical Case	Worst Case
V_{BE} (run to run)	±36 mV	±60 mV
V_{BE} (adjacent devices)	±2 mV	±6 mV
R_1/R_E	±2 %	±5 %

For typical-case tolerances, reference stability is better than 200 ppm/°C for $n > 3$. Because the reference operates from as low as 3.2 V at 100 μA and is stable with temperature, it is an ideal circuit for a monolithic high-efficiency voltage regulator. The p-n-p and n-p-n halves of the circuit must be processed separately so that the p-n-p devices can also be vertical. Lateral p-n-p devices behave differently with temperature and the circuit loses its stability.

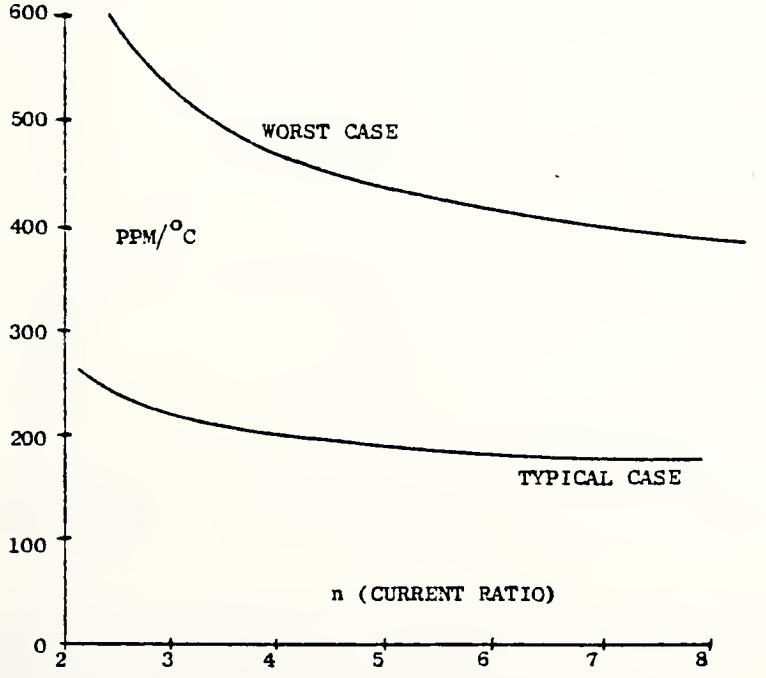

Fig. 22 THE NUMBER OF PARALLEL TRANSISTORS (CURRENT RATIO) VS VOLTAGE CHANGE IN PPM/°C FOR THE VOLTAGE-REFERENCE CIRCUIT IN FIG. 17 FOR TYPICAL- AND WORST-CASE PROCESSING PARAMETERS.

C. Voltage Regulator

Voltage regulator design for greater efficiency at low voltages includes solving the voltage-reference and control-circuit problems. Section B described the design of a stable low-voltage low-current reference, and this section details the control circuit and total regulator design.

Figure 23 presents schematics of three possible control-circuit designs. In the circuit in Fig. 23a (commonly used in commercial monolithic regulators), an n-p-n series pass transistor is controlled by a p-n-p device. This transistor can handle currents in the 10 to 100 mA range; however, its principal disadvantage is the high voltage drop ($\triangle V$) required. The minimum voltage to operate the two-transistor circuit is $V_{BE} + V_{CE(SAT)} = 0.9$ V. It was observed in Fig. 16 that, for $\triangle V = 0.9$ V, regulator efficiency is less than 80% for output voltages of < 3.5 V. If a regulator with this control circuit is used to replace a pair of mercury batteries ($V_{out} = 2.7$ V), efficiency will be only 75%.

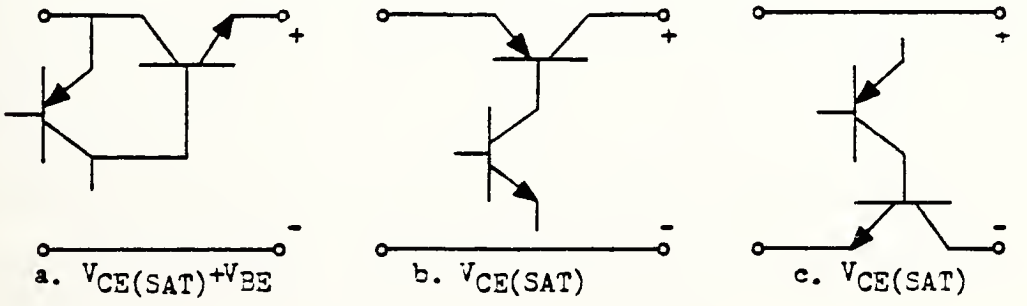

Fig. 23. THREE CONTROL CIRCUITS FOR A LOW-VOLTAGE HIGH-EFFICIENCY VOLTAGE REGULATOR.

Figure 23b is a solution to the large $\triangle V$ value. In this circuit, a p-n-p pass transistor is controlled by an n-p-n transistor. The required

voltage is $V_{CE(SAT)}$ = 0.2 V for a good vertical p-n-p transistor. In monolithic fabrication, however, this transistor is constructed as a lateral device with a much higher $V_{CE(SAT)}$ for a given current than its vertical counterparts; there is also a parasitic substrate p-n-p transistor associated with its operation.

The third control circuit (Fig. 23c) is potentially the most satisfactory. It has an n-p-n pass device that can handle 10 to 100 mA with $V_{CE(SAT)} < 0.3$ V. Its n-p-n transistor operates in a ground-regulation scheme where all dc levels are referenced to the positive bus. The circuit is an effective negative-voltage regulator.

The voltage reference described in Section B and the control circuit in Fig. 23c were combined to produce a simple monolithic voltage regulator that is temperature stable, versatile and efficient at low-output voltages. The regulator schematic is shown in Fig. 24. The circuit was constructed with monolithic transistor arrays. Transistors Q_1 to Q_9 are small-area devices, and Q_{10} is a large-area device with a saturation resistance of 5 Ω . The ground regulation and low saturation resistance of Q_{10} allows a minimum ΔV (for a load current of 10 mA, ΔV = 0.17 V). Other characteristics include:

(1) load regulation = 0.3% (V_{out} = 2.8 V; no load to 27 mA)

(2) line regulation = 0.06% (V_{out} = 2.8 V; I_{out} = 10 mA)

(3) minimum V_{in} = 3.2 V

(4) minimum V_{out} = 1.35 V

(5) ΔV (V_{in} - V_{out} differential);

(I_{out} = 10 mA) = 0.17 V

(I_{out} = 27 mA) = 0.35 V

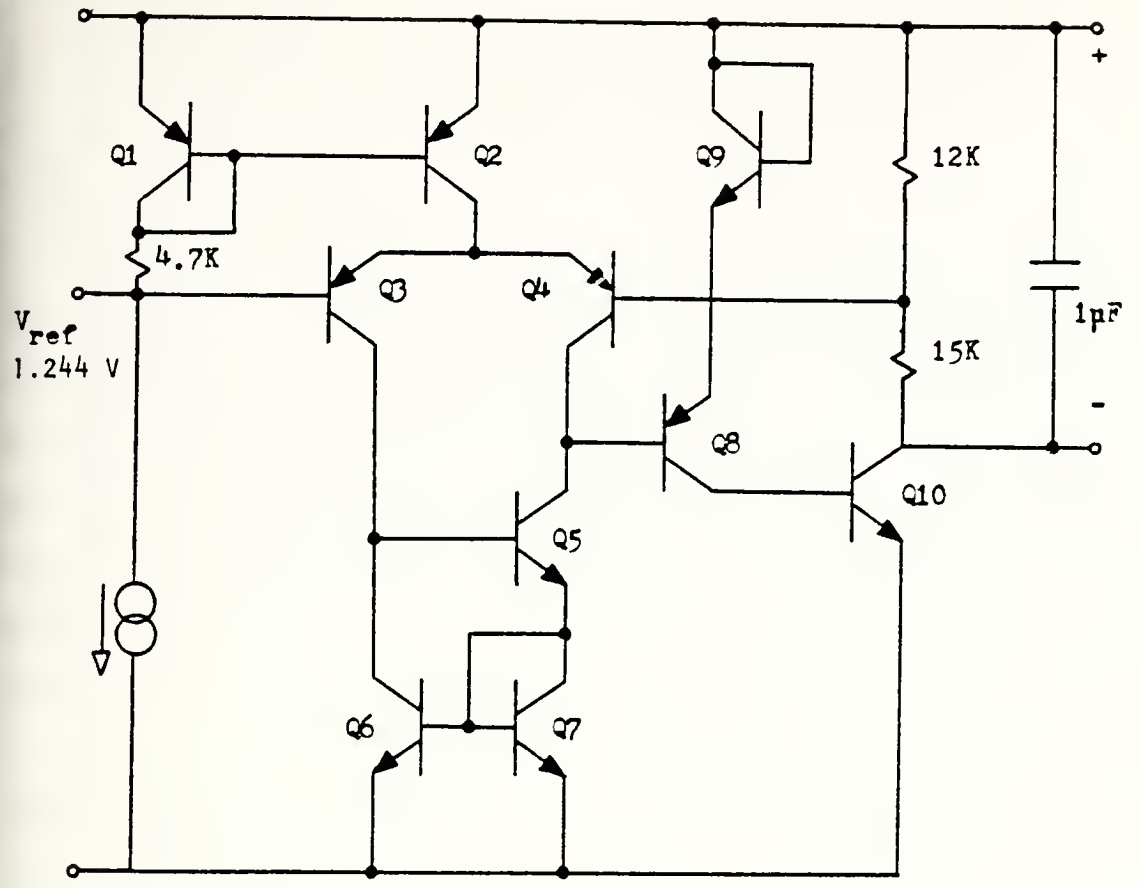

NOTES:

1. Q1 to Q4 and Q8 are on two Interdesign Monochips, Part No. MO-003
2. Q5 to Q7, Q9, Q10 are on one Monochip, Part No. MO-001
3. All resistors 1/8 W, 10% tolerance, carbon

Fig. 24. SCHEMATIC OF A VOLTAGE REGULATOR INCORPORATING THE LOW-VOLTAGE REFERENCE AND CONSTRUCTED WITH MONOLITHIC TRANSISTOR ARRAYS.

Chapter IV

AN ULTRASONIC BLOOD-FLOW VELOCITY SENSOR

One of the primary goals of the Integrated Circuits Laboratory at Stanford University is the fabrication of integrated circuits for medical applications, including the measurement of blood flow. An attractive method for measuring blood flow in small deep veins and arteries is the use of miniature low-power totally implanted ultrasonic sensors. Minitature size and low power operation can be achieved through integrated circuits; however, considerable time is required to produce a properly functioning circuit. As a result, prototype blood-flow sensors are often constructed in discrete component form to verify circuit design and system feasibility. Such a sensor can be produced more economically and rapidly in small quantities than its monolithic counterpart, and any necessary changes or modifications are easier to make. For these reasons and because of the immediate demands for an implanted blood-flow velocity sensor, an intensive effort was undertaken to produce several in discrete form.

The blood-flow sensor discussed in this chapter is the fourth version in a line of such sensors developed at Stanford University and is referred to as the MK IV unit. It is, however, the first to be produced and used successfully in quantity. The principal weaknesses of the earlier discrete-component blood-flow velocity sensors and, therefore, the design goals of this fourth-generation system included:

(1) an improved FM broadcast-band transmitter with greater signal strength and higher immunity to frequency shifts after encapsulation for implant

(2) higher drive level on the crystal transducer to improve the signal-to-noise level

(3) more reliable command transmitter-receiver link with greater turn-on range

(4) reliable and reproducible circuit and system design

(5) overall package volume reduction

Solutions to these problems and many others were obtained during the process of constructing the MK IV unit. Every attempt was made to design simple circuits and to use available standard tolerance components. The entire unit and batteries were placed on miniature printed-circuit boards to minimize interconnections and volume. The result was a blood-flow velocity sensor that was reproducible, reliable and simple to manufacture and use.

A. Principles of Operation

The blood-flow velocity sensor detects the movement of blood by scattering ultrasonic pressure waves off red blood cells and then comparing the frequency of the reflected wave to that of the transmitted wave. The frequency difference is the result of the movement of the reflector (the red blood cell), and this is called the doppler-shift frequency after the Austrian mathematician and physicist Christian Doppler (1803-1853). The doppler shift is a function of red cell (or blood) velocity and, algebraically, it is positive or negative depending on whether the blood is moving toward or away from the source of the pressure waves (ultrasound). This information is not retained, however, because of the simplicity of the electronics; a certain velocity toward or away from the ultrasound source will yield the same doppler frequency. The relationship between blood velocity and doppler-shift frequency is closely approximated by [44]

$$v = \frac{-cf_D}{2f \cos \delta} \qquad (4.1)$$

where

v = absolute velocity of the reflector along the direction of flow

c = propagation velocity (1540 m/sec in human tissue)

f_D = doppler-shift frequency

f = ultrasound frequency

γ = angle of attack (angle between ultrasonic beam and direction of blood flow)

The algebraic sign, in Eq. (4.1) resulting from f_D, is lost in simple systems and only the magnitude of f_D is retained. The elements of Eq. (4.1) are clarified in Fig. 25.

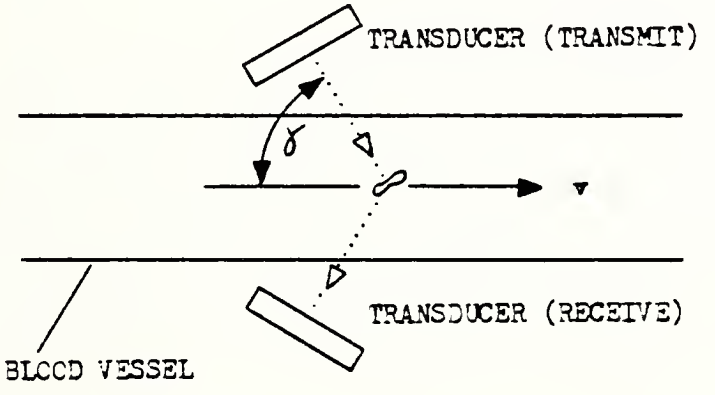

Fig. 25. TRANSDUCER ARRANGEMENT FOR THE MEASUREMENT OF RED BLOOD CELL VELOCITY USING ULTRASONIC DOPPLER TECHNIQUES.

Also shown in this figure is the arrangement of the transducers (piezoelectric crystals) used to convert the electrical signal into a pressure wave (transmit) and then back into an electrical signal (receive). The transmitting crystal is excited continuously. Red blood cells passing through the pressure wave (ultrasonic beam) from this crystal scatter a certain amount of their incident energy toward the

receiving crystal. The frequency of the scattered wave is different from the frequency of the incident wave because of the motion between the transmitting crystal and the red blood cells.

Figure 26 is a block diagram of the implantable ultrasonic blood-flow velocity sensor. The ultrasonic frequency (f) is set by the local oscillator and amplified by the tuned RF amplifier. This amplifier excites the

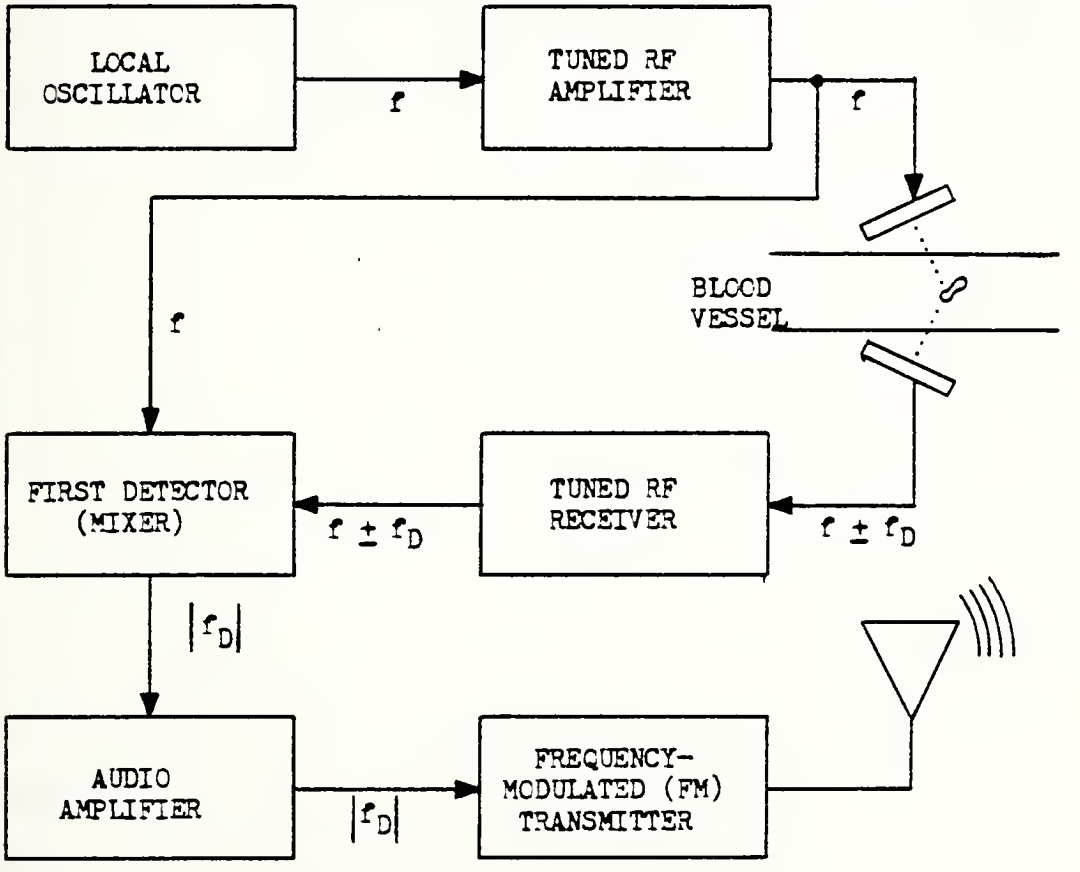

Fig. 26. BLOCK DIAGRAM OF DOPPLER-SHIFT IMPLANTABLE ULTRASONIC BLOOD-FLOW VELOCITY SENSOR.

transmitting piezoelectric crystal. The scattered pressure wave is detected by the receiving crystal, and the signal containing the flow information ($f \pm f_D$) is amplified by the receiver. In the mixer (first detector), f is combined with the information signal ($f \pm f_D$).

The local oscillator and the first detector form a nonlinear frequency converter whose output contains a large number of frequencies related to the two input-signal frequencies. The two dominant resulting frequencies are the sum and difference frequencies ($2f \pm f_D$ and $\pm f_D$). The output of the converter is fed to an audio amplifier that attenuates the RF portion of the signal ($2f \pm f_D$) and amplifies the audio portion ($\pm f_D$). At this point, the algebraic sign of f_D is lost and only its magnitude ($|f_D|$) is retained.

The output of the audio amplifier frequency modulates a VHF oscillator. The center frequency of this oscillator is located in the FM broadcast band (88 to 108 MHz) so that a standard FM receiver is able to detect the transmitted blood-flow information. This simple FM transmitter forms the data link between the implanted blood-flow velocity sensor and the external apparatus that will be used to process, record and analyze the flow information.

Determination of the ultrasonic frequency at which the piezoelectric crystal becomes excited has received much attention. In a pulse-echo systems, frequency selection can be theoretically optimized and is an important aspect of overall system performance; on the other hand, continuous wave systems (Fig. 26) can be operated over a wide range of frequencies. Practical constraints, however, determine the actual frequency. Maximum useful frequency is limited by circuit design and tissue attenuation. At frequencies above 10 MHz there are limits on devices and on the gain-bandwidth product. As power gain becomes more difficult to obtain, power losses due to tissue attenuation increase. The minimum useful frequency is limited by ultrasonic beam spreading and the relationship between the doppler equation (Eq. (4.1)), normal blood-flow velocities and circuit design.

For a given transducer size, the length of the Fresnel zone becomes shorter with decreasing frequency if the ultrasonic wavelength is small compared to transducer size. (The Fresnel zone is the distance normal to the transducer surface over which the ultrasonic beam is approximately parallel.) At the end of the Fresnel zone, the beam begins to spread. A well-defined beamwidth is necessary because the intersection of the transmitting and receiving beams forms the sample volume or the volume in which the movement of the reflectors is detected. To obtain an accurate measurement of velocity at a certain point in a blood vessel, the sample volume must be small compared to the vessel cross section. The relationship between the doppler equation, normal blood-flow velocities (4 to 200 cm/sec), and circuit design can be illustrated by the following example. At an ultrasonic frequency of 6 MHz, the audio-amplifier bandwidth required to cover the flow rates from 4 to 200 cm/sec is 170 to 7500 kHz. A direct relation exists between capacitor size and the low-frequency end of the audio bandwidth in simple audio amplifiers. To achieve a low-frequency roll-off, the capacitor size must be increased. If the ultrasonic frequency is to be dropped to 1 MHz, the audio bandwidth becomes 28 to 1250 Hz. A low-frequency roll-off of 28 Hz requires considerably larger capacitors than does a 170 Hz roll-off; 28 Hz is also below the aural spectrum, and further signal processing would be necessary if the system is intended to provide direct aural information.

Another consideration in the selection of an ultrasonic frequency is the type of piezoelectric material available. The best frequency for these crystals is a function of their area and thickness. The piezoelectric crystals used during this study were designed to operate between 5.5 and 6.8 MHz. This range produces reasonable doppler-shift frequencies,

and the currently available discrete transistors have sufficient gain at 6 MHz for simple circuit design.

B. Circuit Design

The MK IV discrete-component ultrasonic blood-flow velocity sensor was first constructed on a breadboard, using standard-size components. After the design was finalized, the unit was constructed with miniature components and on a small printed-circuit board. The command transmitter and implantable circuitry are described in this section, as are the key operating parameters and the source of all components.

1. Command Receiver

The purpose of the command receiver is to conserve battery power. The flow sensor is powered by two Mallory RM625RT2 mercury cells rated at 1.35 V and 250 mA hours connected in series to produce a supply voltage of 2.7 V. The T2 designation indicates that there is a welded tab on both the positive and negative battery terminals, used to solder the battery in place on the printed-circuit board. Figure 27 is a schematic of the command receiver. The circuit was developed by earlier Stanford University researchers, and its operation is unique. Modifications included the use of standard high-quality transistors in epoxy cases and a long ferrite-loaded solenoid as an antenna for better receiver "turn-on" range. The standard transistors have stronger leads for more reliable circuit assembly, lower leakage currents to produce lower "off" supply currents, better gain, and reduced saturation voltages, especially on transistor switch Q7, for greater receive efficiency. Q7 exhibits a very low $V_{CE(SAT)}$ (approximately 0.1 V) which reduces the voltage drop across the transistor switch and maximizes the supply voltage available to the blood-flow sensor.

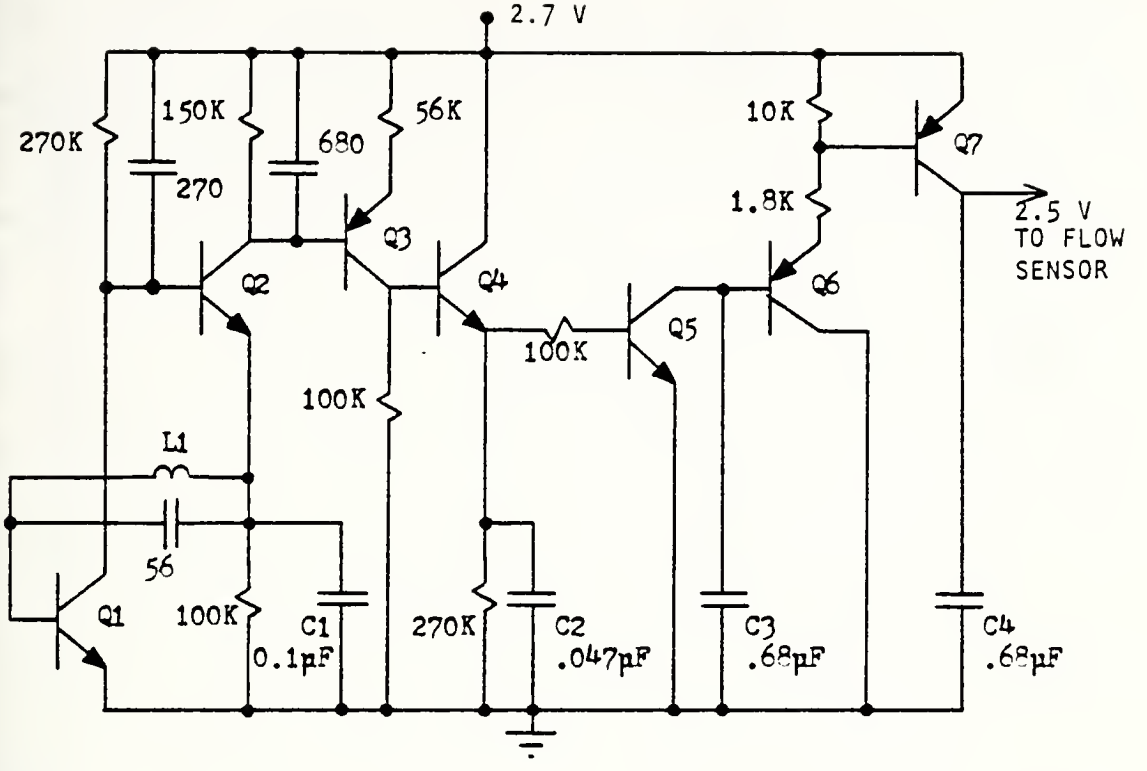

NOTES:

1. Q3, Q6 and Q7: 2N4520
2. Q1, Q2, Q4 and Q5: 2N3565
3. Capacitors in pF except as noted. pF capacitors are ceramic: Series C10, U. S. Capacitor Corp., 2151 No. Lincoln St., Burbank, California 91504
4. μF capacitors are tantalum: type HA, Tansitor Electronics Inc., West Road, Bennington, Vermont
5. Resistors in ohms: 1/8 W, 10% tolerance, Allen-Bradley
6. L1 is 260 turns No. 40 AWG single layer on ferrite rod 25.4 mm long, 6.35 mm diameter, Q-1 material, part No. F125-1, Indiana General, Valparaiso, Indiana 46383
7. Circuit tuned to 460 kHz and 1300 Hz

Fig. 27. COMMAND RECEIVER CIRCUIT OF THE MK IV BLOOD-FLOW VELOCITY SENSOR.

The command receiver is activated by a 460 kHz carrier frequency that is amplitude modulated 100% by a 1300 Hz signal. The selection of this frequency is such that it will not interfere with the intermediate

frequency of AM broadcast receivers (455 kHz) and will not coincide with the international distress signal (500 kHz). It was chosen in the MF band (300 kHz to 3 MHz) because of the reasonable propagation ranges and power requirements at these levels. The carrier frequency is modulated or coded at 1300 Hz to provide some immunity to spurious noise and extraneous RF energy that would turn the command receiver "on" at unwanted times.

The LC circuit at the base of Q1 has sufficient Q to turn on Q1. The RC collector circuits of Q1 and Q2 produce negli ible gain at 460 kHz, but they amplify the 1300 Hz signal injected at the base of Q1; Q3 further amplifies this 1300 Hz signal and drives Q4. The RC time constant of the emitter circuit of Q4 is sufficiently long (compared to 1300 Hz) to allow C2 to charge until Q5 is turned on. The current gain of Q5, Q6 and Q7 is high enough to force Q7 into saturation; Q7 is then "on," and the remaining circuitry receives battery voltage minus the $V_{CE(SAT)}$ of Q7 for a supply voltage of approximately 2.55 V. C3 and C4 filter out the remaining 1300 Hz signal and minimize ripple on the dc supply bus. Tests conducted on three MK IV blood-flow sensors indicated that the optimal carrier frequency is 458 to 460 kHz and the peak modulation frequency is 1300 to 1400 Hz. Using the command transmitter discussed below, the same three circuits were successfully turned "on" at a maximum range of 2.5 to 2.7 m which is considered adequate for most laboratory uses.

The command receiver conserves battery energy because, in the "off" condition, the total supply current is only 15 μA. Neglecting internal battery resistance, the 250 mAhr battery discharged at the 15 μA rate will last 1.9 years which is longer than necessary for most laboratory experiments. Practical battery lifetimes with intermittent operation usually run four to six months.

The following problems were encountered with the command receiver.

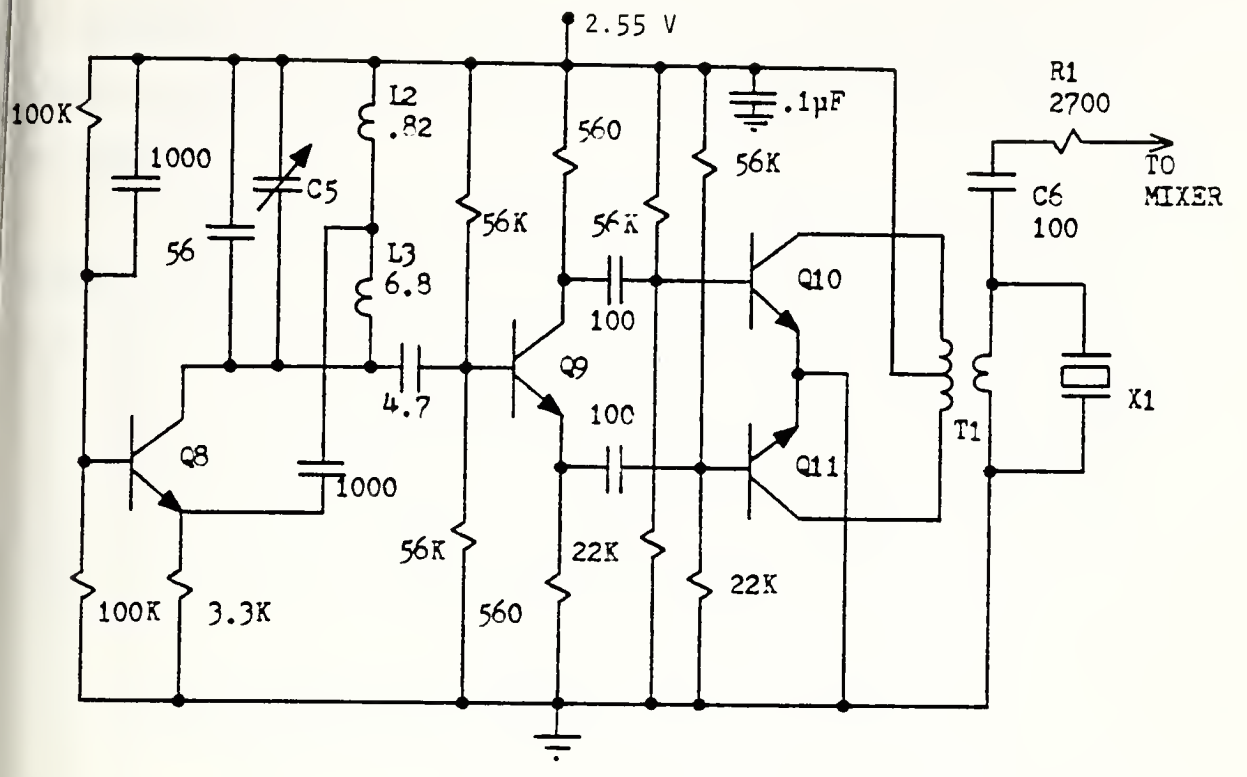

NOTES:

1. Q8 to Q11: 2N3565
2. Capacitors in pF except as noted. Notes 3 and 4 Fig. 27 apply
3. Resistors in ohms. Note 5 Fig. 27 applies
4. L2 and L3 in μH: Series 1025, Delevan molded RF coils, Delevan Electronics Division, 270 Quaker Road, East Aurora, N. Y. 14052
5. C5 miniaturized variable capacitor range 4 to 18 pF, part No. 9410-4, Thin Trim Capacitor, Johanson Manufacturing Corp., Boonton, N. J. 07005
6. T1 center tapped transformer, primary 24 turns No. 34 AWG, Secondary 12 turns No. 34 AWG: Toroid core part No. F303-1 of Q-1 ferrite material. Note 6 Fig. 27 applies
7. X1 is 1.5 x 1.5 mm square piezoelectric crystal

Fig. 28. ULTRASONIC TRANSMITTER CIRCUIT OF THE MK IV BLOOD-FLOW VELOCITY SENSOR.

amplifier buffer the oscillator from any variation in load across the secondary of T1. As seen in Fig. 26, the output of the transducer-driving amplifier provides a reference signal to the mixer. This reference signal

is connected to the mixer through R1 and C6 which serve to adjust the signal level at the mixer and block the flow of dc current through T1 to ground.

The oscillator and crystal drive amplifier have the highest power consumption of all the circuits in the flow sensor; combined, they draw between 6 and 8 mA. Because of the base-biasing scheme on Q10 and Q11, supply current is dependent on the supply voltage level. An increase of 0.5 V or more from a nominal 2.6 V will cause a rapid rise in supply current. At 2.6 V, the power delivered to the crystal is approximately 4.5 mW for a power efficiency of approximately 25%.

3. Tuned RF Receiver and Mixer

Figure 29 is a schematic of the tuned RF amplifier that functions as a receiver and the mixer that detects the doppler-shift information. The receiving transducer X2 converts the ultrasonic pressure wave to an electrical signal and drives the base of Q12 through transformer T2. Q12 amplifies the signal containing the information and feeds it to Q13 where it is mixed with the reference signal to remove the RF portion and leave only the audio frequency range doppler-shift information.

By reversing the action of X1, where an electrical signal is converted into a mechanical vibration to produce a pressure wave, X2 senses the pressure wave scattered from the red blood cells and causes it to vibrate and produce an electrical signal capable of amplification and processing. The signal level generated by X2 while sensing blood-flow velocity is on the order of 1 μv rms. At such a low signal level, amplifier and transistor noise become significant. Each transistor has an optimal source resistance that minimizes noise. Q12 has the lowest noise when its collector current is small and the signal source impedance is

large. T2 increases the source resistance seen by Q12 by a factor of 25 and, at the same time, multiplies the voltage level produced by X2 by a factor of 5.

C7 couples the output of T2 to the base of Q12 so that this base can be easily biased by a pair of resistors. Without C7, the base of Q12 would be at ground potential; however, the selection of C7 is not arbitrary because C7 and T2 form a resonant circuit. For certain values of C7, Q12 acts as an oscillator because of the resonant circuit connected to its base and collector. Values of C7 greater than 33 pF cause an oscillation problem. Values less than 33 pF unnecessarily attenuate the

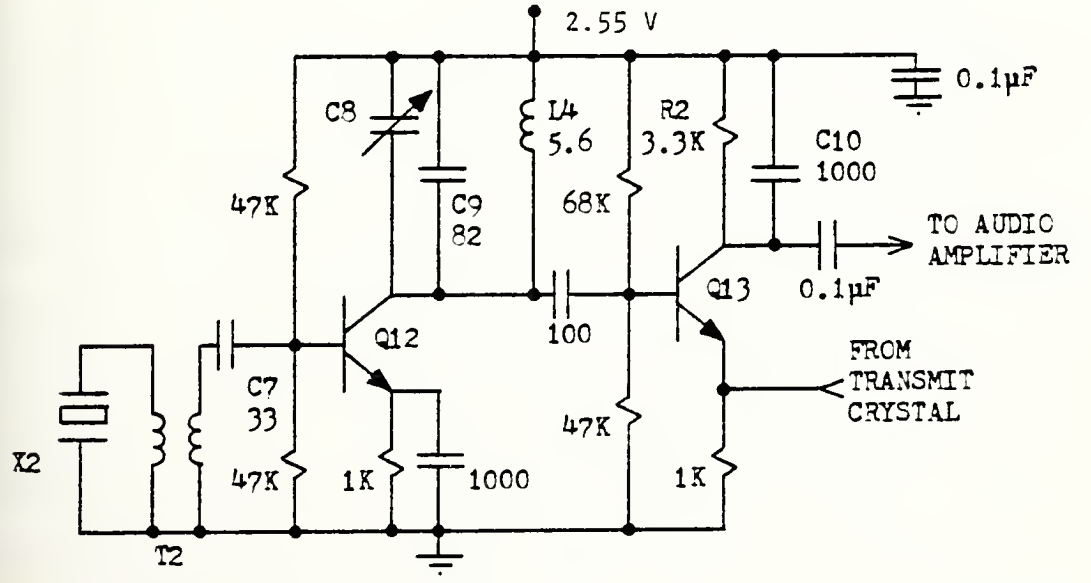

NOTES:

1. Q12: 2N3563
2. Q13: 2N3565
3. Capacitors in pF except as noted. Notes 3 and 4 Fig. 27 apply
4. Resistors are in ohms. Note 5 Fig. 27 applies
5. C8 similar to C5 Fig. 28 but with range 7 to 45 pF, part No. 9410-4
6. L4 in μH, similar to L2 and L3 Fig. 28
7. T2 transformer, primary 5 turns No. 34 AWG, secondary 25 turns No. 34 AWG toroid core F303-1 of Q-1 ferrite material. Note 6 Fig. 28 applies
8. X2 same as X1 Fig. 28

Fig. 29. ULTRASONIC RECEIVER CIRCUIT OF THE MK IV BLOOD-FLOW VELOCITY SENSOR.

signal received by X2. Originally, this receiver input circuit was designed with X2 as a 4 x 4 mm transducer. Later it was reduced to 1.5 x 1.5 mm, a factor of 7 reduction in surface area with a corresponding increase in transducer impedance. With this rise in impedance, T2 became less important and could probably have been removed. Any transformer voltage multiplication lost by its removal would have been offset by enlarging C7 and reducing its effective attenuation. It remained in the circuit, however, because the system was already a proven design and experiments indicated that the overall signal-to-noise ratio would not be changed by the removal of T2.

The collector circuit of Q12 serves as a resonant load and a filter. The combination of C8, C9 and L4 in parallel yields an amplifier tuning range for Q12 in the 6 MHz region. C8 allows for tuning from 5.6 to 6.6 MHz. When properly tuned this RF amplifier exhibits a typical voltage gain of approximately 37 dB. C9 must be sufficiently low loss to produce a high-Q resonant circuit. All components should be checked first with the HP 4815A RF Vector Impedance Meter to ensure they exhibit low-loss characteristics. During production of the flow sensors the USCC capacitor C9 was substituted with a Republic Mucon capacitor. Overall system signal-to-noise performance declined, and it took several days of trouble-shooting before it was determined that the RF amplifier gain had been degraded by the low-Q capacitor.

After the RF amplifier, the ultrasonic frequency signal containing the doppler-shift information is processed by the mixer stage Q13. This information is injected at the base of Q13 while its emitter current is modulated by the unshifted reference signal from the local oscillator. This circuit is a very crude but effective multiplier. One of its

fundamental outputs is the doppler frequency (f_D) which, for average flow velocities, is between 170 and 7500 Hz. The purpose of C10 in parallel with R2 in the collector circuit of Q13 is to roll off or filter out all signals with frequencies above 50 kHz. This retains the doppler information and suppresses the RF frequencies.

The magnitude of the signal at the emitter of Q13 affects the sensitivity of the flow sensor. After ensuring that C8 is properly tuned for highest gain at the chosen ultrasonic frequency, the reference-signal level at the emitter of Q13 is adjusted for maximum sensitivity and signal-to-noise ratio. This level ($\approx$ 950 mV peak-to-peak) is set by R1 and C6 and is a function of the drive level across X1. In addition to functioning as a multiplier and filter, this stage also has a voltage gain of approximately 10 dB.

4. Audio Amplifier

The audio amplifier circuit (Fig. 30) is a standard design, composed of two capacitively coupled common emitter stages. In both stages, the emitter resistor, which sets the emitter current in conjuntion with the two base resistors, is bypassed by a large tantalum capacitor to achieve adequate gain at low audio frequencies. The collector or load resistor of each stage (Q14 and Q15) is capacitively bypassed by a ceramic capacitor to remove stray RF signals that would be amplified and interfere with the transmission of the audio-frequency doppler information. The passband created by this RF filtering and by the emitter bypass capacitors is from 360 to 13,500 Hz. This frequency range has proven adequate for most blood-flow studies of major arteries. The measured voltage gain of the two-stage amplifier is approximately 15 dB for Q14 and 30 dB for Q15. Combined with the RF gain of the

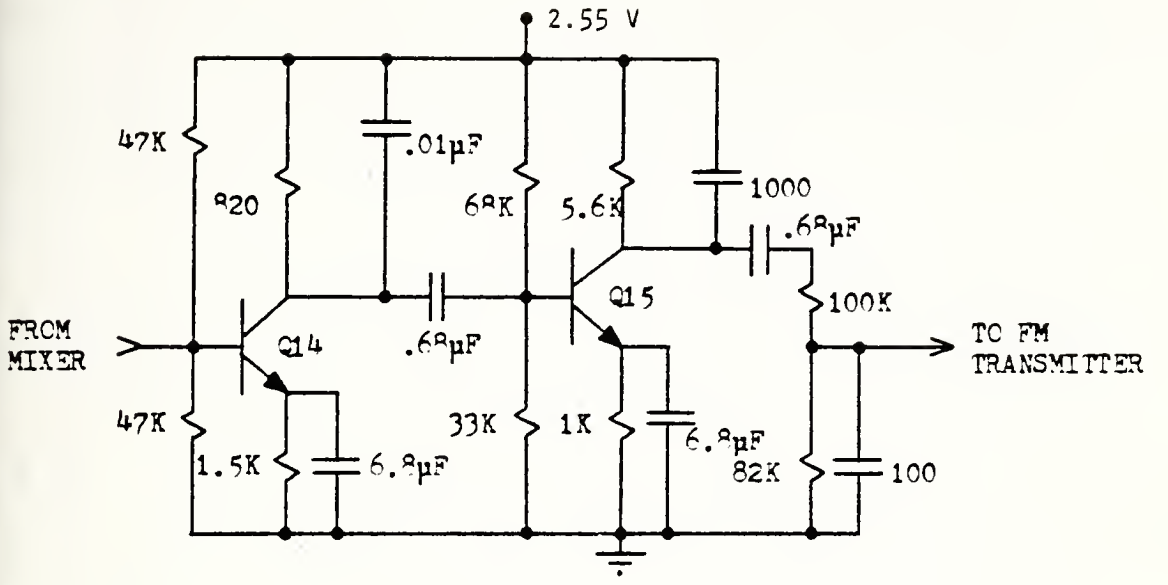

NOTES:

1. Q14, Q15: 2N3565
2. Capacitors in pF except as noted. Notes 3 and 4 Fig. 27 apply
3. Resistors in ohms, 1/8 W, 10% tolerance: Allen-Bradley

Fig. 30. AUDIO AMPLIFIER CIRCUIT OF THE MK IV BLOOD-FLOW VELOCITY SENSOR.

tuned receiver and the signal level produced by X2, this audio gain is sufficient to produce a 1.5 to 2 V peak-to-peak signal at the collector of Q15 during actual blood-flow measurements. Any increase in audio gain would only cause the second-stage amplifier to be overdriven, resulting in distortion in the modulation of the VHF carrier used to transmit the doppler-shift information and in a reduction in the overall signal-to-noise ratio.

5. Frequency-Modulated Transmitter

The final stage of the implanted ultrasonic blood-flow sensor is the simple frequency-modulated VHF transmitter (Fig. 31) which serves as

the information link between the implanted package and the external FM receiver and other data-processing electronics. The transmitter has four basic stages -- the variable capacitance diode D1, VHF oscillator Q16, oscillator buffer Q17 and antenna driver Q18.

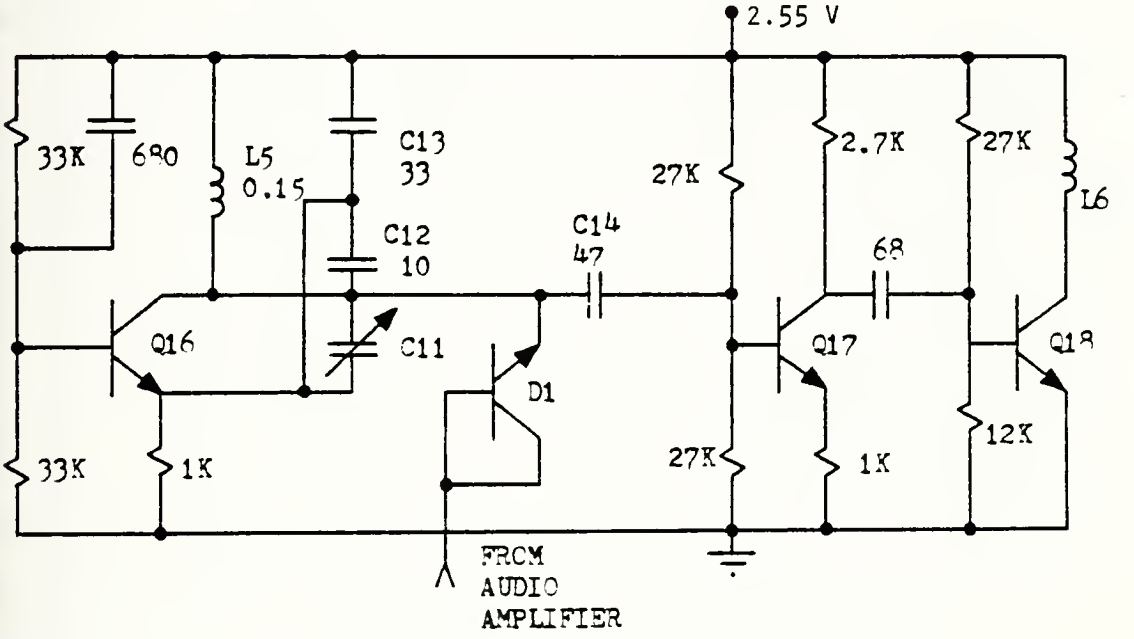

NOTES:

1. Q-16 to Q18 and D1: 2N3563 (Fairchild)
2. Capacitors in pF. Note 3 Fig. 27 applies
3. L5 in μH. Note 4 Fig. 28 applies
4. C11 similar to C5 Fig. 28 but with range 1 to 4.5 pF: Part No. 9410-0
5. L6 is 6 turns No. 26 AWG tinned wire single layer on ferrite rod 19 mm long and 6.35 mm diameter, Q-3 material: Part No. F125-1. Note 6 Fig. 27 applies

Fig. 31. FREQUENCY MODULATED (FM) TRANSMITTER CIRCUIT OF THE MK IV BLOOD-FLOW VELOCITY SENSOR.

The variable capacitance diode D1 is a diode-connected high-frequency transistor. It is reverse biased, and a change in junction voltage will vary the junction width and the diode capacitance. Using a 2N3563 transistor as D1, this capacitance change is approximately

0.0733 pF/V for reverse voltages from 1.5 to 2.4 V. By using a voltage divider at the output of the audio amplifier, the voltage range can be adjusted to achieve an oscillator frequency change of 150 kHz. Normal FM broadcast-band transmitters produce a carrier that varies 75 kHz either side of their center frequency, and standard FM receivers are designed for this range.

Circuit Q16 is a modified Colpitts oscillator. Its frequency can be changed approximately 8 to 9 MHz by the variable capacitor C11. Using the capacitance values for C12, C13 and C14, production oscillators have a minimum and maximum frequency of 93 and 105 MHz, respectively; any variance in one of these capacitors will affect this range. The FM broadcast band is 88 to 108 MHz. The wax-encapsulation process used to protect the flow sensor decreases oscillator frequency approximately 5 MHz. As a result, the preencapsulation oscillator frequency should not be less than 93 MHz to avoid shifting the frequency below the broadcast band and out of the range of the FM receiver.

The buffer circuit Q17 is a simple common-emitter circuit without an emitter bypass capacitor. It provides a certain amount of isolation between the oscillator and the transmitting antenna L2. It has a theoretical voltage gain of 8 dB; however, in practice, it has approximately unity voltage gain because of the frequency of operation.

The antenna drive circuit Q18 is a grounded emitter circuit with the transmitting antenna as the only load. If is biased just above turn-on and, when a signal is present at its base, the current drain is reasonable (2 to 3 mA). The signal level across the antenna is approximatley 1.2 V peak-to-peak, and the transmitter has an effective range exceeding 10 m. After encapsulation in wax for implant, the transmitted frequency becomes

immune to change from capacitive loading of the antenna by contact with the receiving animal or by handling.

The selection of transistors D1, Q16, Q17 and Q18 is critical. Experience with both Fairchild and National devices revealed that the Fairchild transistors produce 6 to 8 dB less noise. This decrease reduces overall signal-to-noise ratios by the same amount.

Although C13 was connected as shown in Fig. 31, it could also have been connected directly from the emitter of Q16 to ground. This redesign would simplify the printed circuit board.

6. Command Transmitter

The command transmitter is not a part of the implanted electronics package; however, it is a key segment of the system and essential to the operation of the flow sensor. Figure 32 is a schematic of the carrier and modulation oscillators and the antenna drive amplifier, and Fig. 33 is the circuit design of the power supplies.

The amplitude-modulated signal required to turn on the command receiver is produced by carrier and modulation circuits (Fig. 32). These are astable multivibrators whose frequency of operation is determined by the size of C1 and C2; C1 is adjusted for 460 kHz and C2 is adjusted for 120 Hz. The multivibrators then drive a pair of parallel connected transistors Q9 and Q10 that are turned on and off at the carrier (460 kHz) and modulation frequencies, respectively. The result is a 460 kHz signal turned on and off at 1200 Hz, and this approximates a 100% amplitude-modulated carrier. This modulated signal becomes the input to a push-pull amplifier that drives a series-tuned loop antenna. The resulting transmitted signal has sufficient power to activate the command receiver at approximately 3 m.

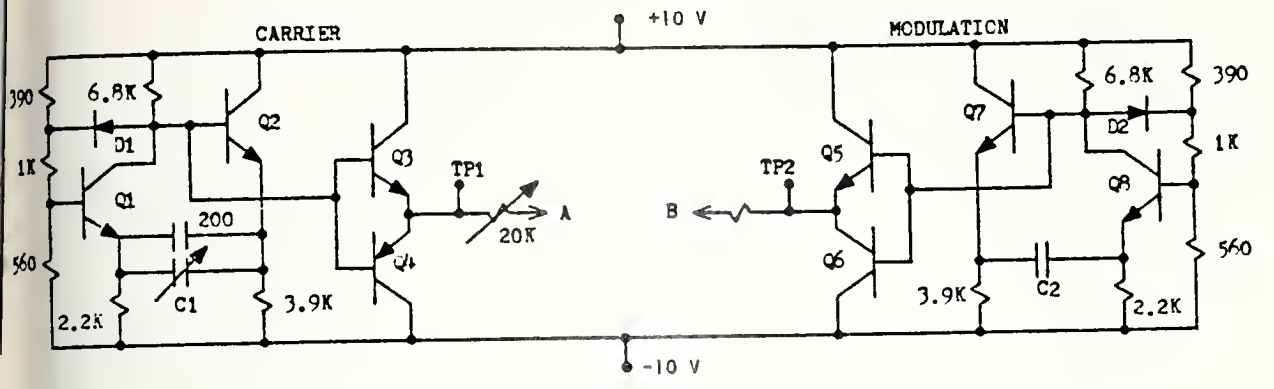

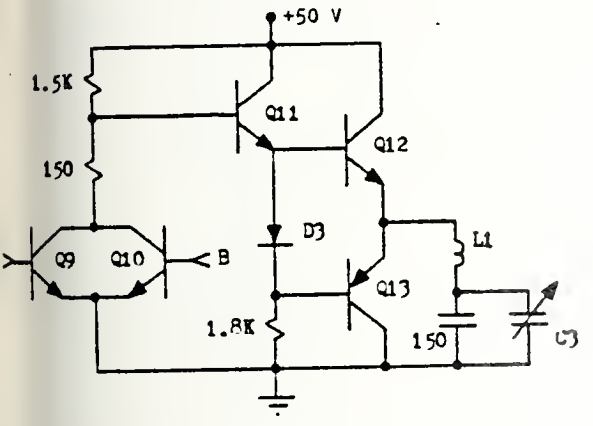

NOTES:

1. Q1 to Q3, Q5, Q7, Q8: 2N706
2. Q4, Q6: 2N3640
3. Q9 to Q11: 2N3053 with finned heat sink NF-207
4. Q12: MJE2523
5. Q13: MJE2491
6. D1 to D3: 1N914
7. Resistance in ohms, 1/4 W
8. Capacitance in pF
9. C1 is carrier frequency adjustment: 10-100 pF
10. C2 is front panel plug for modulation frequency adjustment: 0.1 μF for 1200 Hz
11. C3 is for antenna tuning: 5.6 to 102 pF
12. L1 is 266 mm diameter loop antenna 25 turns No. 20 AWG, approximately 700 μH
13. TP1 is carrier frequency front panel test point
14. TP2 is modulation frequency front panel test point

Fig. 32. COMMAND TRANSMITTER CIRCUIT FOR THE MK IV BLOOD-FLOW VELOCITY SENSOR.

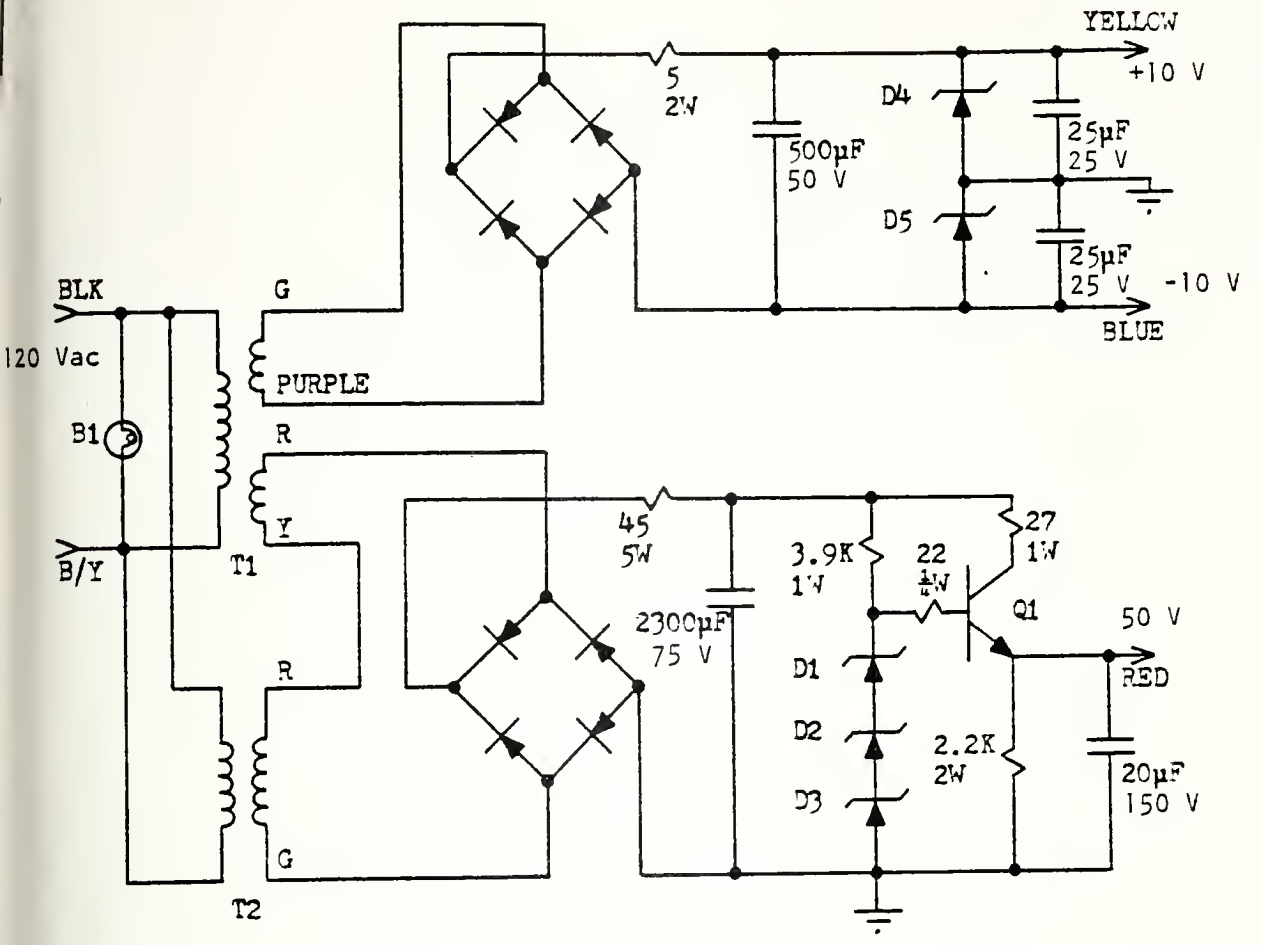

NOTES:

1. Q1: MJE2523 with homemade heat sink of aluminum 1.5 mm thick
2. D1, D2: 1N5248 (18 V zener diode)
3. D3: 1N5242 (12 V zener diode)
4. D4, D5: 1N5240 (10 V zener diode)
5. T1 and T2: Triad F91X, 300 mAdc, Triad Distributor Division, 305 North Briant St., Huntington, Indiana. The secondary of T1 has been split to form two separate transformers.
6. Resistances in ohms, power ratings shown in watts
7. B1: Neon Eldema E-Lite power indication lamp, resistance 100 KΩ

Fig. 33. POWER-SUPPLY CIRCUIT FOR COMMAND TRANSMITTER.

The power supply (Fig. 33) is crude but adequate to power the command-transmitter circuits; however, more efficient power supplies

TRANSCUTANEOUS POWER

AND

ULTRASONIC BLOOD-FLOW

VELOCITY SENSORS

A THESIS
SUBMITTED TO THE DEPARTMENT OF ELECTRICAL ENGINEERING
AND THE COMMITTEE OF GRADUATE STUDIES
OF STANFORD UNIVERSITY
IN PARTIAL FULFILLMENT OF THE REQUIREMENTS
FOR THE DEGREE OF
ENGINEER

BY

LCDR PHILIP JAMES CURTIS USN

MARCH 1978

Approved for the Electrical Engineering Department:

Approved for the University Committee
on Graduate Studies:

ABSTRACT

Ultrasonic flow sensors to monitor blood flow in animals and humans have been in use for many years. This study draws on the experience of past research to solve some of the recurring problems found with implanted sensors. Four areas have been explored, all linked by the contribution each makes toward the development of an improved blood-flow sensor.

In the first, the use of transcutaneous power to operate an implanted ultrasonic blood-flow sensor is analyzed. The purpose of such a study is the total elimination of batteries. The theory of transcutaneous power is developed from the basic equations of Maxwell and Stefan and a basic efficiency statement is derived. Design guidelines and graphs are generated from this statement and basic experiments are conducted to indicate the validity of the theory. The conclusion is that a properly designed and applied transcutaneous power-transfer circuit is capable of efficiencies as high as 90%.

A high-efficiency low-voltage regulator and a low-voltage reference are developed in the second area. This regulator and reference are compatible with existing low-voltage implantable circuits intended initially to be battery powered. The regulator is capable of delivering 2.7 V (two mercury cells in series) with better than 85% efficiency; the voltage reference operates from less than 100 μA and has a temperature stability better than 200 ppm/°C.

The third area details an extensive program involving the design, fabrication and employment of a discrete-component continuous-wave implanted ultrasonic doppler blood-flow velocity sensor. The study

could be redesigned. Figure 34 is a photograph of the complete command transmitter with loop antenna, used successfully for over two years with more than a dozen implanted blood-flow sensors.

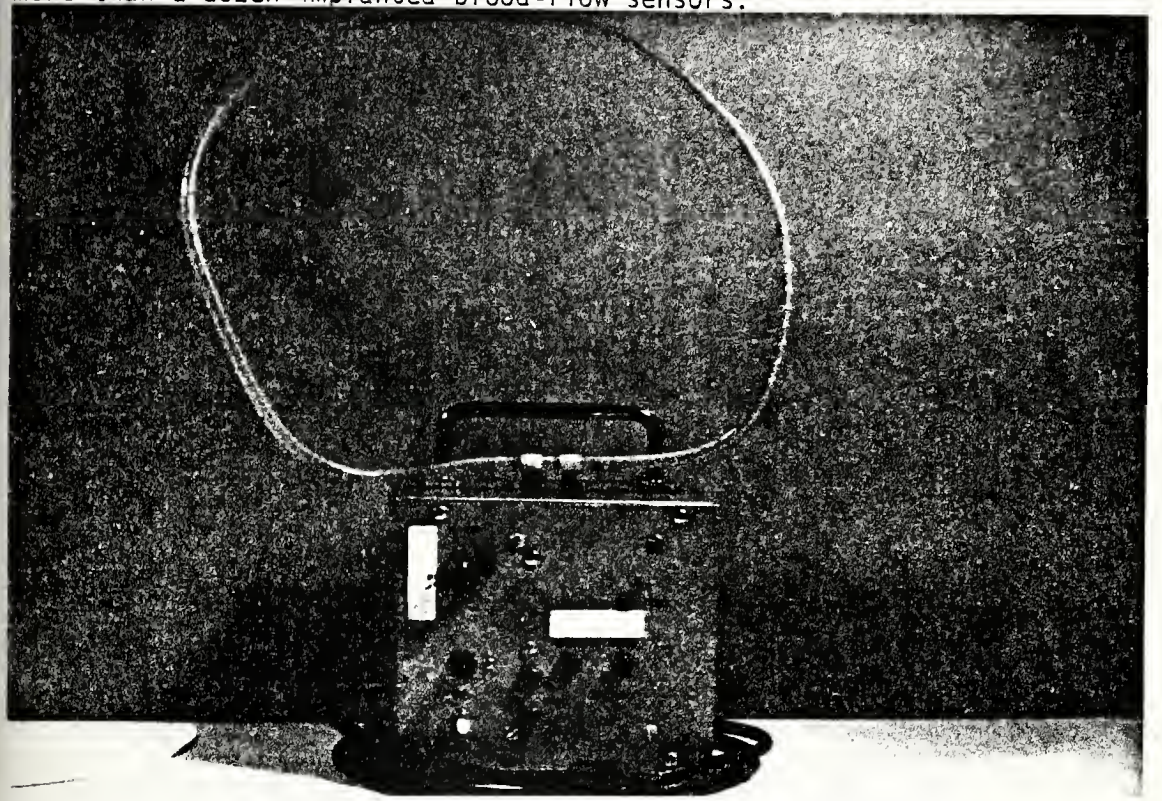

Fig. 34. COMMAND TRANSMITTER WITH LOOP ANTENNA.

C. Package Design

Earlier blood-flow velocity sensors have failed to produce medical data because they were poorly packaged or powered or because transducer connectors or cables failed prematurely. Electronics packaging for implant is as important as circuit design. The procedures used to package the MK IV discrete-component blood-flow sensors are detailed in this section. Six major areas are discussed -- the printed circuit board, battery connections, transducer cable design, cable strain relief and wax and silastic encapsulations.

1. Printed Circuit Board

A single one-sided miniature printed circuit board is the backbone of the blood-flow velocity sensor. Its fabrication begins with a double-sided fiberglass board; one side contains the foil circuit and the other holds the component location guides and values. The first circuit boards were made from thin stock, 0.762 mm thick (0.030 in.), to reduce package volume and weight; however, so thin a stock tended to warp, and it was more difficult to drill holes for component leads to a size that would provide a snug fit to prevent the components from backing out when the board is inverted for soldering. A thicker board offers increased rigidity. The stock finally selected was 1.524 mm thick (0.060 in.). The art work (or mask) was made four times actual board size. Standard 4X layout tape and preformed masks were used for transistors and component lead holes. This art work was then photoreduced to actual board size. Figure 35 is a photograph of a printed circuit board after tinning but before trimming and drilling component-lead and battery-location holes.

The dimensions are 33.7 x 68.5 mm. An attempt to maximize component density and to minimize circuit size resulted in a 73% packing density. Because the ferrite rod antennas for the command receiver and FM transmitter established the minimum thickness of the finished circuit, all components are mounted vertically. Including the thickness of the solder on the component leads on the circuit side of the board, the package thickness is 9.65 mm prior to wax and silastic encapsulation.

This single-sided circuit board containing all components, batteries and antennas (Fig. 36) incorporates the basic design criteria required to produce the blood-flow sensor. It is simple, makes use of standard techniques and available components and parts, and eliminates all types of socket and plug interconnections.

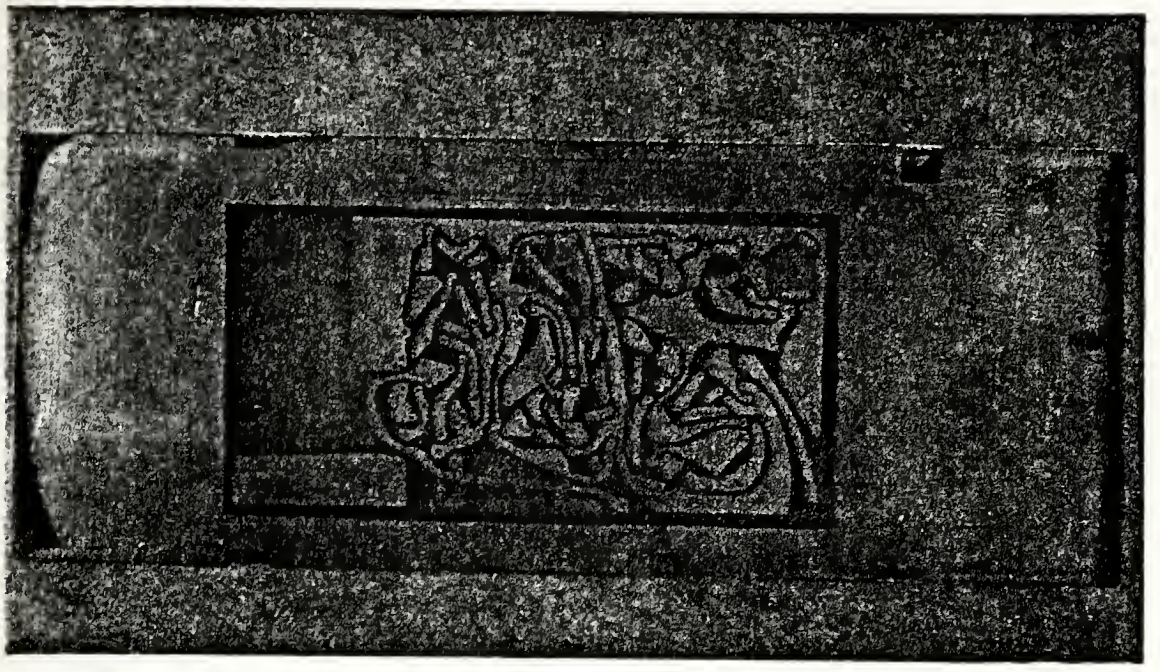

Fig. 35. PRINTED CIRCUIT BOARD FOR MK IV BLOOD-FLOW SENSOR.

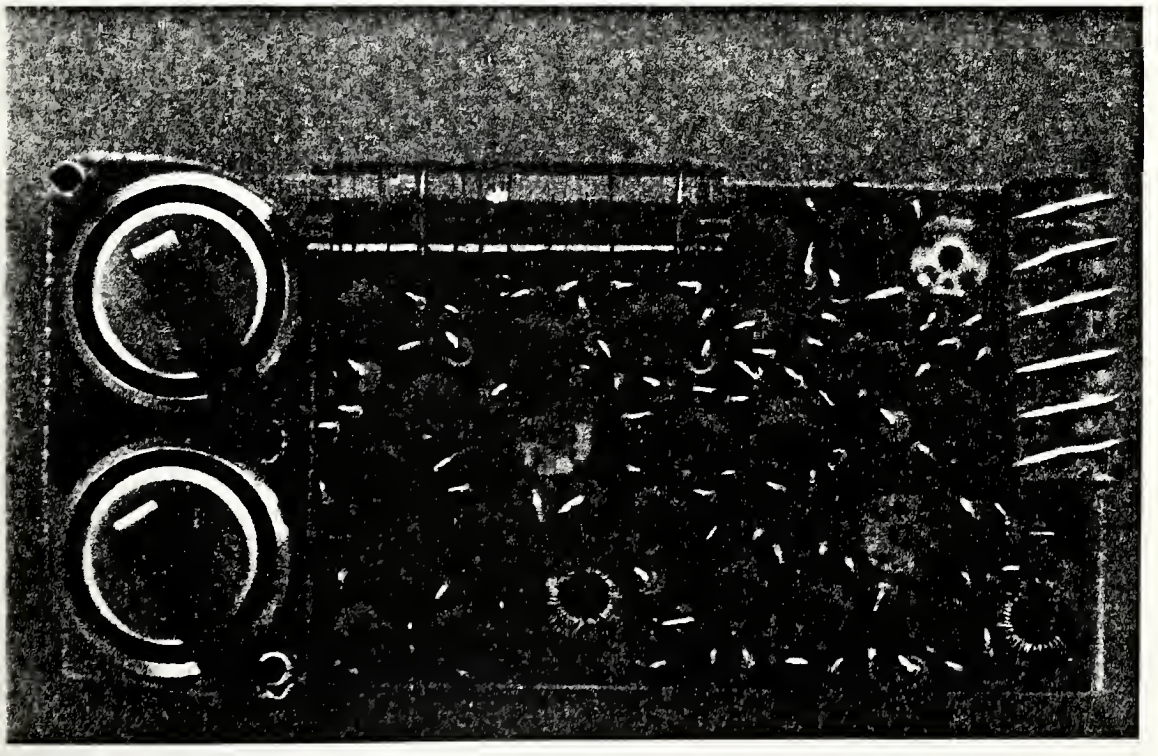

Fig. 36. COMPLETE MK IV BLOOD-FLOW VELOCITY SENSOR WITHOUT TRANSDUCERS ATTACHED.

Also shown in Fig. 36 are the toroidal transformers used for the transmitting and receiving transducers. The transducer cables are soldered to the board just in front of the transformers. A wire loop is then placed around the cable, pulled tight, and each end is also soldered to the circuit board to anchor the cable. Medical adhesive is applied to the entire connection for initial strain relief. The black strip on top of the batteries is the shrink-tubing around the negative battery terminal tabs. The large round black components are the epoxy case transistors.

2. Battery Connections

A key failure mode in all battery-powered implanted electronics is battery failure. Earlier versions of discrete-component blood-flow sensors used an interchangeable battery pack for easy battery renewal; however, plug and socket interconnections risk poor contact as a result of corrosion or loose fit. The Mallory RM625RT2 cell has a tab welded to each terminal, and the battery can be mounted in a recess on the circuit board and the tabs can then be soldered directly to the tinned circuit. Experience with a dozen units that have been "turned around" two, three and four times apiece shows this to be a reliable means of connecting the batteries. The tab on the negative battery terminal is insulated from the positive case by slipping a short length of shrink-tubing over it prior to installing the battery.

3. Transducer Cable

Transducer cable failure is the result of mechanical fatigue or chemical corrosion. A miniature coaxial cable manufactured by Microdot was selected to connect the electronics package and the transmitting and receiving transducer. Its inner connector and shield are tinplated copper. The

cable is purchased with a hard Teflon outer insulation which is removed because it tends to make the cable rigid. A length of this cable is then inserted into a silastic tube that has been enlarged by soaking in toluene. The tubing with the inserted cable is then injected with silastic medical adhesive that has been thinned with toluene or TCE (trichoroethylene). This produces a soft and flexible cable, and the medical adhesive bonds the outer conductor or shield to the tube. Care must be taken to avoid air pockets in the adhesive. A properly assembled cable, void of air pockets, will withstand corrosion over a long period of time.

The connection of the cable to the transducer and package must also be sealed with medical adhesive to prevent body fluids from seeping into the outer shield and inner conductor. This phase of the implanted package design still requires considerable research and development. Controlled assembly of the cable and silastic tubing in a vacuum followed by curing at atmospheric pressure would help to eliminate air pockets and voids that are sites for corrosion.

Figure 37 is a photograph of a transducer and cable. The crystal holder is made of epoxy, and the small gray square is the piezoelectric material attached to the epoxy holder with acrylic cement. Additional epoxy is poured onto the back of the holder to secure the cable after it has been connected to the crystal. The transducer holder does not have the taper discussed in the following section. This is a photograph of a used transducer, and careful study will reveal a dark discoloration in the coaxial shield. This is a result of corrosion and indicates that body fluid has begun to leak into the cable and attack the tinned copper shield. Stainless steel cables will prevent such corrosion and improve mechanical strength as well.

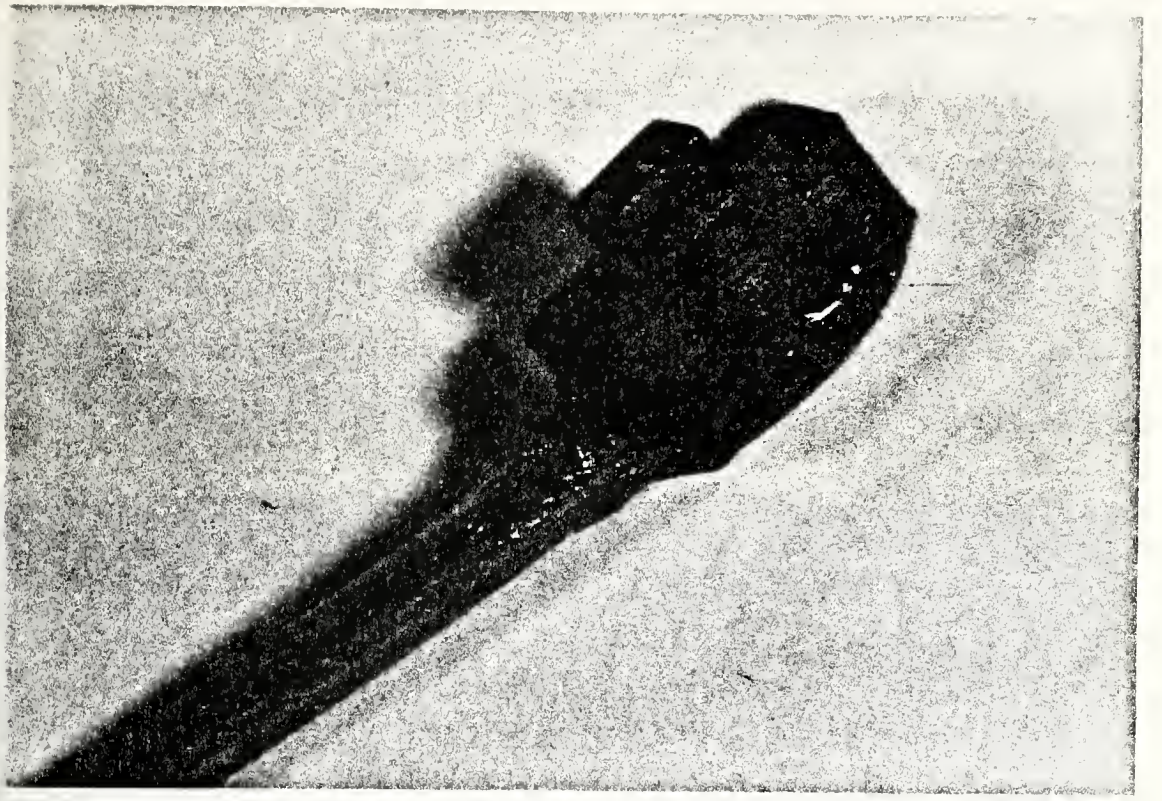

Fig. 37. TRANSDUCER AND CABLE SHOWING THE FIRST SIGNS OF DETERIORATION.

4. Cable Strain Relief

Mechanical fatigue of the cable also causes deterioration and eventually an open circuit. It occurs most often when the cable is forced to flex sharply at one point repeatedly and where the cable attaches to the printed circuit board and to the transducer. The most effective way to relieve cable strain at these two points is to form a long taper on the cable, beginning with a diameter of approximately 7 mm and then tapering to the size of the silastic tubing over a length of 45 mm. This taper is made of silastic and is part of the outer coating on the unit. To prevent bending the cable at the point where it is attached to the circuit board, the tapers are molded at a 45° angle to the edge of the package.

Figure 38 is a photograph of a MK IV blood-flow velocity sensor ready for implant. The tapers are evident on each transducer cable. This photo is of an early version, and the taper at the transducer end of the cables formed with clear medical adhesive is not present. Later versions have tapers that extend 15 mm up the cable. The two transducer holders are inserted into an epoxy and silastic strip cuff formed from two semi-circular epoxy pieces hinged at one side. The cuff is then slipped around

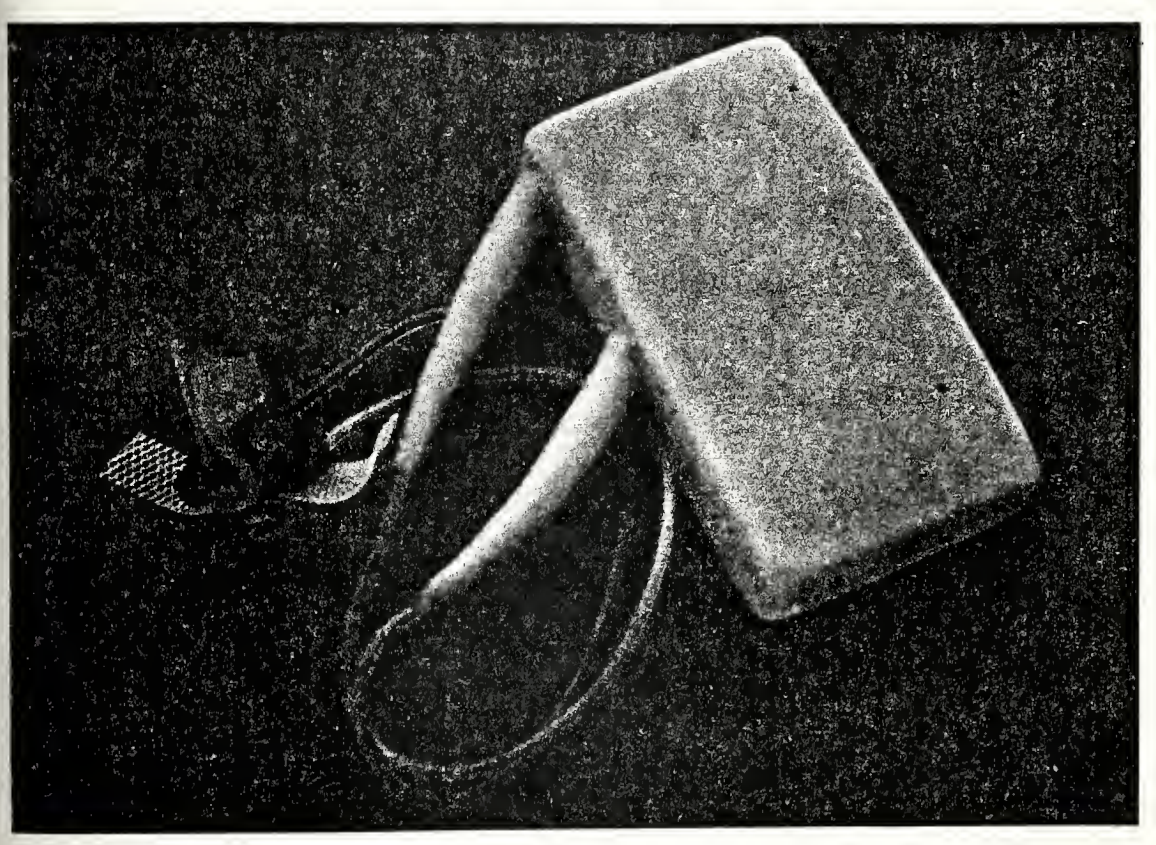

Fig. 38. COMPLETE MK IV BLOOD-FLOW SENSOR READY FOR IMPLANT.

the vessel whose flow is to be monitored. The other side of the cuff is sutured closed, using the inner silastic strip, and the second outside silastic strip is also sutured closed to stabilize the transducer holders

in the cuff. This interchangeable cuff is made in a variety of sizes to accommodate a number of different vessels.

5. Wax Encapsulation

One of the most important steps in preparing the flow sensor for implant is the wax encapsulation. To protect electronic circuits from body fluids that cause corrosion and shorts, they have been enclosed in metal cans and cast in clear resin. The can approach, however, requires through-can connectors for the antenna and transducers -- a potential source of leakage. The can must be carefully sealed and unsealed to replace batteries or to repair the circuit, and metal enclosures are usually bulky. Casting in resin makes circuit repair impossible and requires that the batteries be connected externally, thereby creating a potential problem of battery shorts from body fluid. Resin is not waterproof and leakage through the resin will degrade circuit performance.

Wax, on the other hand, does not interfere with antenna operation, is easy to remove, and forms a waterproof barrier on the electronic circuit. The wax, called Paraplast, is a mixture of parafin and plastic fibers that toughen it and make it less brittle. In the MK IV, the entire printed circuit board with batteries and transducer cables attached is cast in a block of Paraplast. Performance of all circuits remains unchanged except that the frequency of the FM transmitter shifts down approximately 5 MHz. A few important procedural steps must be followed to produce uniformly reliable wax encapsulations.

Paraplast melts at 68°C. To prevent damage to the mercury batteries, the temperature should not exceed 70°C. The flow sensor is placed in a wax mold and then in a heated vacuum chamber at 70°C for approximately

four hours to evenly heat the circuit and mold. A beaker of wax chips is melted on a hot plate, cooled to 75°C, and poured into the mold. The chamber is then evacuated to 685 mm-Hg or better, and this vacuum is maintained for 15 min to produce a wax casting free from bubbles and voids. The chamber is then returned to atmospheric pressure and left sealed to retain the heat. The chamber heater is then turned off, and the mold and wax are allowed to cool slowly for approximately six hours. The wax should not be cooled under vacuum or too rapidly because it contracts 50% while cooling and voids or flaws will result. The casting is then carefully removed from the mold, and all sharp edges are scraped smooth. The flow sensor is now ready for molding in silicon rubber (medical-grade silastic).

Wax adheres to everything. Although this makes it an ideal material for protecting the blood-flow sensor circuits, it is also a difficult material to cast because of the problems encountered when separating it from the mold. Proper mold design will minimize this problem. The mold should be made of Teflon and be sprayed with mold release before each use. The sides and bottom should be constructed in many sections to minimize the surface area in contact with the casting that must be separated at one time. The joints should be tight to prevent the liquid wax from leaking out before it cools. One of the large surface areas of the casting must open on top so trapped air can escape and so the wax will contract evenly as it cools. Around this large top opening through which the wax is poured, there must be a built-up section that increases the volume of wax necessary to fill the mold by 50% above that required to make the desired casting. This additional wax prevents the cooling wax from contracting to the point where the flow sensor circuits are not covered with the proper thickness of wax; a casting should have a minimum thickness of 1.27 mm on all components.

Once cooled, this extra section can be removed, and the excess wax that extends above the actual casting scraped off before it is removed from the mold. This procedure was used at least thirty times to encapsulate the MK IV blood-flow velocity sensor.

This process could be simplified, however, by placing the printed circuit board with all its components and batteries in a small plastic box with an open top. The transducer cables could enter through the side. A holder could be made to act as a "cofferdam" around the open top to hold the excess wax necessary to allow for contraction during cooling and to prevent spillage of the "boiling" wax during the vacuum phase.

After the unit is retrieved from the subject in which it was implanted, the wax casting can be removed to fit fresh batteries and to attach new transducer cables. The bulk of the wax is removed by heating the unit in a beaker and allowing the melted wax to drain off through a screen at the bottom. A temperature of 80°C is adequate. The remaining film of wax is removed by boiling the unit in a freon solvent at 40°C; TCE (trichloroethylene) is not recommended because of its harsh properties and possible damage to the tantalum capacitors. After freon cleaning, the batteries and transducer leads are unsoldered. When new batteries and transducers are connected, sufficient amounts of solder flux must be used to produce a rapid and good quality solder bond. Care must be taken to avoid overheating the fine printed circuit and separating the foil from the board.

6. Silastic Encapsulation

The final step in preparing the MK IV blood-flow sensor for implant is encapsulating the wax casting in medical-grade silicon rubber (Dow Corning trade name "silastic"). Silastic is the antithesis of wax in

its ability to adhere to different surfaces and the ease by which it can be released from its mold.

The mold used to cast silastic on the MK IV units is a combination of Teflon, phenolic and acrylic. Care should be taken, however, with mold design. The mold should be released with only a small amount of applied pressure. It should also produce a casting with a minimum silastic thickness of 1.27 mm; such a thin layer of silastic could tear if this mold design is improper.

The silastic and its catalyst are normally refrigerated. In advance of its use, the silastic should be allowed to warm because, at room termperature, it is easier to pour and mix with its catalyst. Cure times are very temperature-sensitive, and the mixing table that comes with the silastic assumes a temperature of 21°C. The catalyst should be added in accordance with the directions so as to avoid too long or too short a cure time. It must be thoroughly mixed with the silastic, or the casting will not cure properly. A uniform layer free from voids and air pockets can be obtained only if the silastic is first de-aired in a vacuum chamber. The silastic with its catalyst is placed in a beaker at least five times larger than its original amount and is then subjected to 685 mm-Hg vacuum or better. It will bubble and foam and increase four or five times it volume, and then it will suddenly fall or shrink. The vacuum should be continued for several minutes longer, and then the silastic is ready to pour into the mold. Because of its high viscosity, the mold is filled half full before the wax casting is inserted in it to ensure that the underside of the casting is completely coated. The top of the casting is then covered with silastic, and the lid is placed over the mold. The lid has suitable pressure-relief holes through which excess silastic can escape. The room-temperature

cure time is 24 hours. This can be shortened to approximately four hours by heating the mold in an oven at 50°C; this temperature will not soften the wax casting enough to deform it.

The silastic provides a biologically inert covering for the flow sensor and a tapered strain relief for the transducer cables; it also serves to cushion the hard wax coating. After silastic encapsulation, the MK IV discrete-component ultrasonic blood-flow velocity sensor is ready for sterilization followed by implantation.

D. Clinical Experience

Twelve MK IV blood-flow velocity sensors were built between December 1972 and July 1973. Units 1 through 6 were originally built as MK IV Mod-1 units and were later converted to Mod-2 units -- the major difference was the crystal drive level.. The Mod 1 operated with 4 x 4 mm crystals and a drive level of 1.2 to 1.5 V peak-to-peak; the Mod 2 used 1.5 x 1.5 mm crystals and a 5.8 to 6.5 V peak-to-peak drive level.

More than 19 canine implants were performed with these twelve units between May 1973 and March 1975 at Stanford University Hospital, and a few at NASA Ames. The Stanford implants monitored renal and iliac artery blood flow in control and cardiac autograft canines to determine the response to exercise of the denervated heart in heart transplant subjects. Figure 39 is a section of a strip-chart recording of renal and iliac flow taken with units 8 and 9 just after implant.

Table 1 summarizes the experiences through June 1974 with the twelve MK IV units. The prototype unit (Unit 1) was never implanted but was retained for display. The purpose of unit 2 was to test the effectiveness of Paraplast in protecting the electronic circuit from body fluids. It was

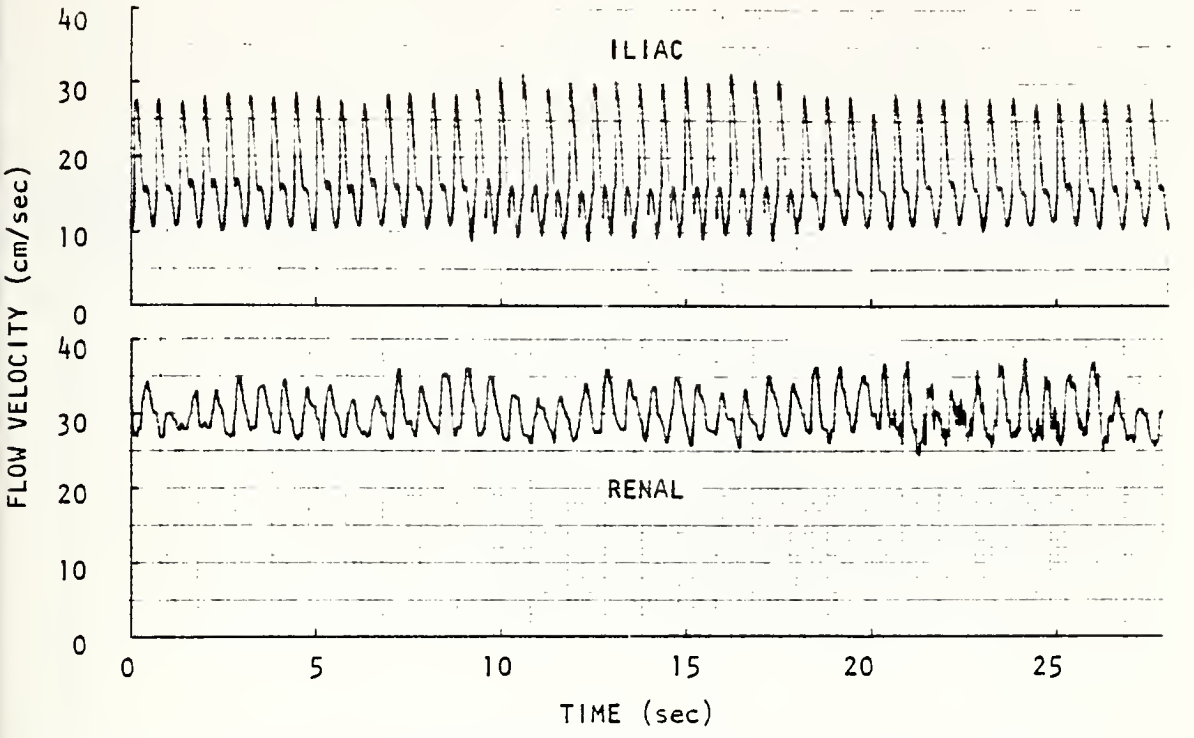

Fig. 39. STRIP-CHART RECORDINGS OF ILIAC AND RENAL FLOW VELOCITIES.

placed in a tank containing a saline solution maintained at 37°C and was turned on periodically by the command transmitter to determine its operational status. After six months, the batteries failed; however, there were no indications of corrosion or signs of damage from the saline solution. Subsequent experience has shown that Paraplast is a nearly perfect insulator for the electronic circuit, and no implanted unit has failed because of body-fluid leakage.

Figure 40 is a photograph of five MK IV units taken from implant subjects. The two on the left have had the wax removed, and the three on the right have had the silastic removed except for the strain reliefs on the transducer cables. On the far left unit, the white material near the two toroidal transformers is the medical adhesive applied to the transducer cable connections to the printed circuit board.

TABLE 1

SUMMARY OF BLOOD-FLOW VELOCITY-SENSOR IMPLANTS

UNIT/IMPLANT NUMBER	DAYS FUNCTIONAL	DAYS IMPLANTED	FAILURE MODE(S) AND COMMENTS
1	--	--	prototype
2/1	180	--	environmental tank
2/2	unknown	45	perhaps cables; confused with unit 5
3/1	151	191	first cables, then batteries; information intermittent throughout; with unit 6
4/1	7	7	dog destroyed due to foot injury
4/2	30	150	cables; FM carrier remained good throughout; with unit 5
4/3	59	59+	batteries
5/1	7	7	dog destroyed due to foot injury
5/2	30	150	cables; FM carrier remained good throughout; with unit 4
5/3	unknown	45	perhaps cables; confused with unit 2
6/1	151	191	first cables, then batteries; information intermittent throughout; with unit 3
7/1	102	167	cables first, then batteries; with unit 10
8/1	2	12	cables
9/1	unknown	12	batteries
9/2	30	30	dog died of pneumonia; FM and information good
9/3	7	7	sutures opened; dog died
10/1	88	167	cables; with unit 7; FM carrier still good when removed

TABLE 1

CONTINUED

UNIT/IMPLANT NUMBER	DAYS FUNCTIONAL	DAYS IMPLANTED	FAILURE MODE(S) AND COMMENTS
11/1	31	124	batteries; cables still good when removed
12/1	59	124	batteries
12/2	43	43	unit removed intact; dog used as a heart donar
12/3	unknown	unknown	implanted at NASA Ames

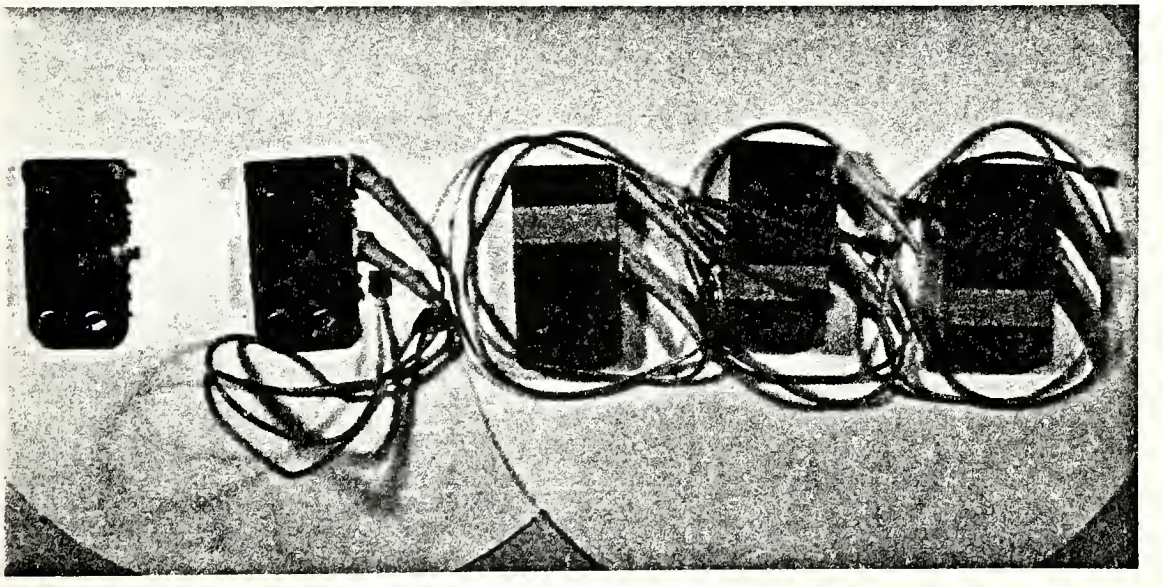

Fig. 40. MK IV UNITS AFTER REMOVAL FROM IMPLANT SUBJECTS.

The packaging techniques discussed in the previous section were developed as a result of the clinical experience obtained from these twelve MK IV blood-flow sensors. It can be seen in Table 1 that eight units failed because of cable problems and four failed because of

batteries. The solution to the cable failures is a more careful assembly under controlled conditions and better strain-relief tapers at both the transducer and the package to extend the life of the average implant to eight or ten months. The solution to the battery failures is to replace the batteries with a transcutaneous power system; improvement in cable design and construction will extend cable life to the point where battery failure becomes the primary failure mode. The next chapter discusses the details of such a transcutaneously powered discrete-component blood-flow velocity sensor -- the first of its kind.

Chapter V

A TRANSCUTANEOUSLY POWERED ULTRASONIC BLOOD-FLOW VELOCITY SENSOR

This chapter describes the fabrication of a discrete-component ultrasonic blood-flow velocity sensor (the MK V) that operates without batteries. It receives power through a pair of inductively coupled coils. The driving (or primary) coil is external to the subject, and the driven (or secondary) coil is part of the implanted package. The external coil is placed over the implanted package and power is transferred to the implanted coil at radio frequencies. The RF power is then rectified and regulated and used to supply a blood-flow sensor that is approximately the same as the unit described in Chapter IV. The details and theory of transcutaneous power transfer were presented in Chapter II.

A. Circuit Design

The theory of operation of the MK V transcutaneously powered sensor is identical to that of the MK IV; however, the MK IV operated by means of a command-receiver antenna and batteries, but the MK V has a very thin pancake coil and rectifier and regulator circuits. Elimination of the batteries and command-receiver antenna reduces volume, and further reductions are achieved through the use of smaller toroidal transformers and a smaller FM transmitter antenna. The volume of the MK IV is 43.7 cm^3 and the MK V is only 15.5 cm^3; this is a volume reduction of 64%.

Figure 41 is a photograph of the first MK V unit. The circuitry is housed in a round plastic package only 8.3 mm deep. This plastic case adds strength and simplifies wax encapsulation. There is no need for a complex mold. A simple retaining ring around the top of the case contains

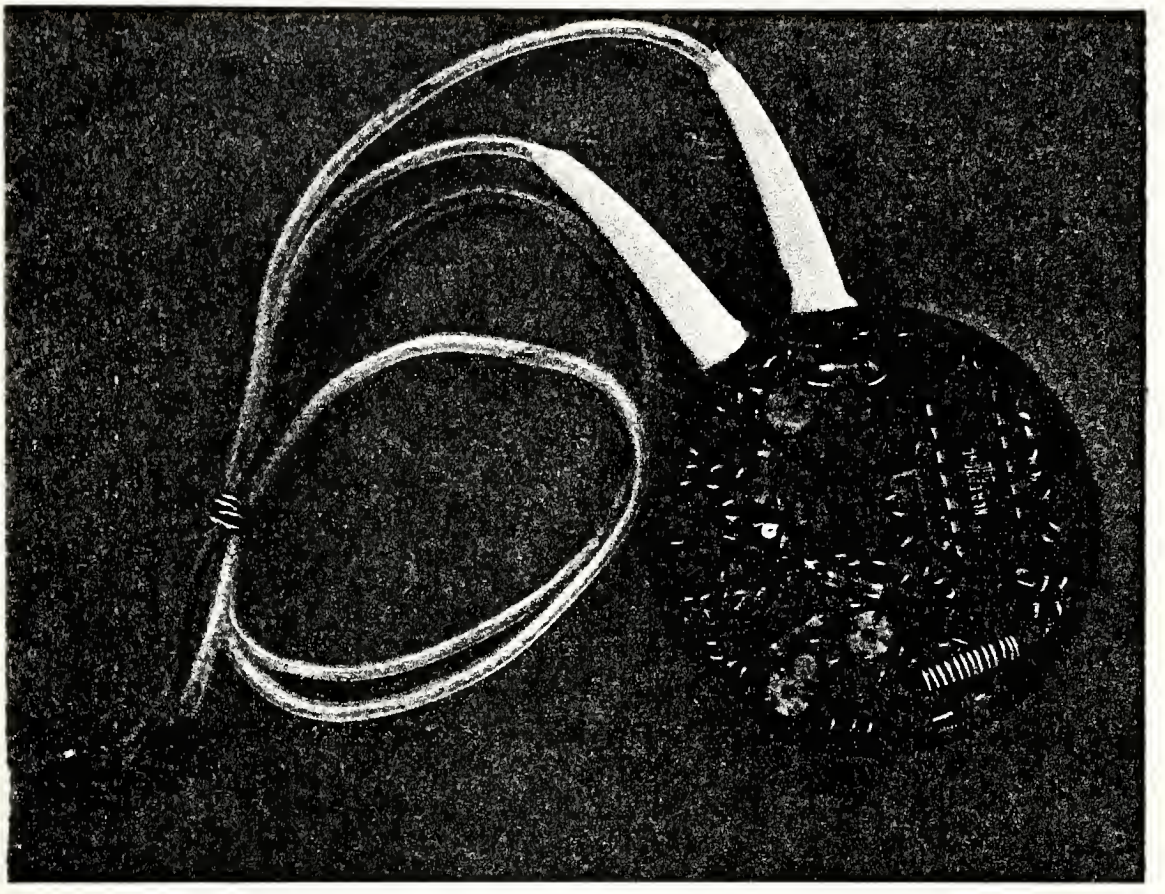

Fig. 41. THE MK V TRANSCUTANEOUSLY POWERED BLOOD-FLOW SENSOR.

the excess wax required during cooling to compensate for contraction and to prevent spillage during the vacuum phase of the casting.

Figure 42 is a schematic of the first stage of the implanted circuitry -- the rectifier. The secondary coil (L1) is series tuned by capacitor C1. A full-wave bridge composed of diodes D1 through D4 rectifies the RF signal received by L1, and capacitor C2 connected across the input of the voltage regulator (Fig. 43) filters the rectified signal.

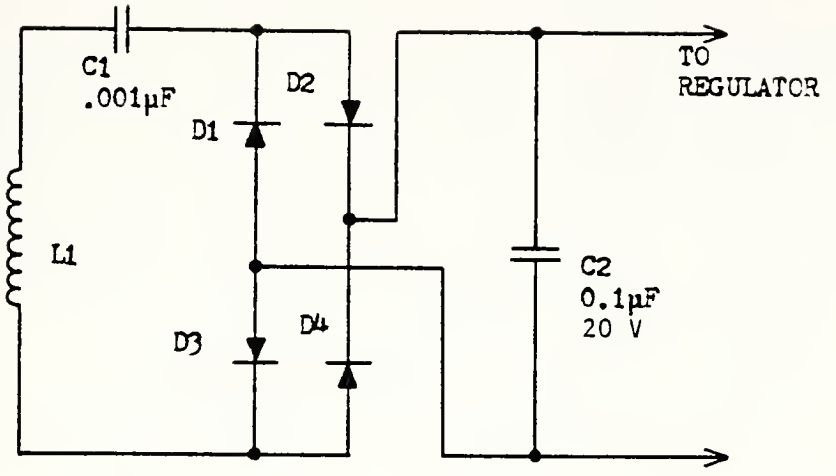

NOTES:

1. D1 to D4: 1N4148
2. C1 is ceramic. C2 is tantalum.
3. L1 is 47 turns of 7-41 AWG litz wire in a single layer pancake, I. D. 13 mm, O. D. 44 mm. Coil wound between two acrylic discs 0.79 mm thick.

Fig. 42. POWER-RECEIVING COIL, RECTIFIER AND FILTER FOR THE MK V TRANSCUTANEOUSLY POWERED BLOOD-FLOW VELOCITY SENSOR.

The voltage regulator uses five monolithic transistors in a 14-pin dual inline package. The V_{BE} of these monolithic transistors are more closely matched than are those of the randomly selected discrete-component transistors. Close V_{BE} matching of Q11 and Q12 and Q14 and Q15 is necessary because of their common-emitter connections. Diodes D10 and D11 at the base of Q12 act as a voltage reference. By adjusting R16 to produce an output voltage of 2.87 V at room temperature (21°C), the output voltage at body temperature (37°C) will be approximately 2.7 V which is equivalent to two 1.35 V mercury cells in series. This regulator has an output resistance of 0.5 Ω at V_{in} = 3 V and 0.24 Ω at V_{in} = 6 V.

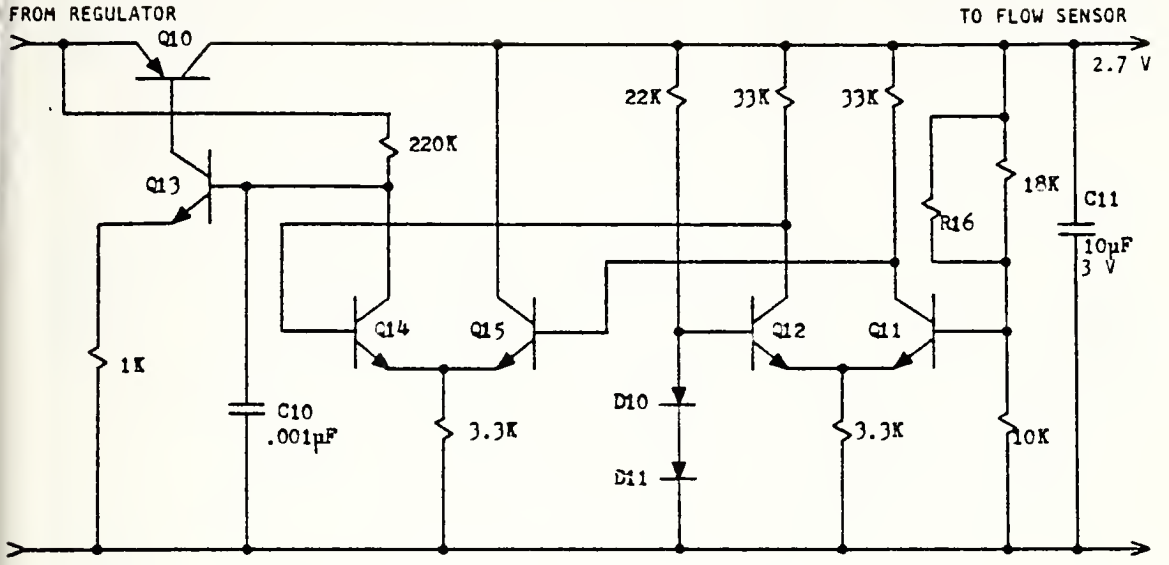

NOTES:

1. Q10: 2N4250
2. Q11 to Q15: CA3046 14 pin dual inline package
3. R16 is selected to give 2.87 V output at 21°C.
4. Resistances in ohms, 1/8 W, 10% tolerance, Allen-Bradley
5. C10 is ceramic, series C10, U. S. Capacitor Corp., 2151 North Lincoln St., Burbank, CA 91504.
6. C11 is tantalum, type HA, Tansitor Electronics Inc., West Road, Bennington, VT
7. D10 and D11: 1N4148

Fig. 43. VOLTAGE REGULATOR FOR THE MK V TRANSCUTANEOUSLY POWERED BLOOD-FLOW VELOCITY SENSOR.

The regulation factor over a 30 V V_{in} range is better than 0.1%. One discrete transistor (Q10), used in the circuit as the pass transistor, produces a 2.7 V output with only a 2.9 V input for a load current of 22 to 26 mA.

Figure 44 is a schematic of the ultrasonic transmitter. The modified Colpitts oscillator formed by Q20 produces a variable frequency range of 6.22 to 6.91 MHz. A transformer-coupled input and output are provided by

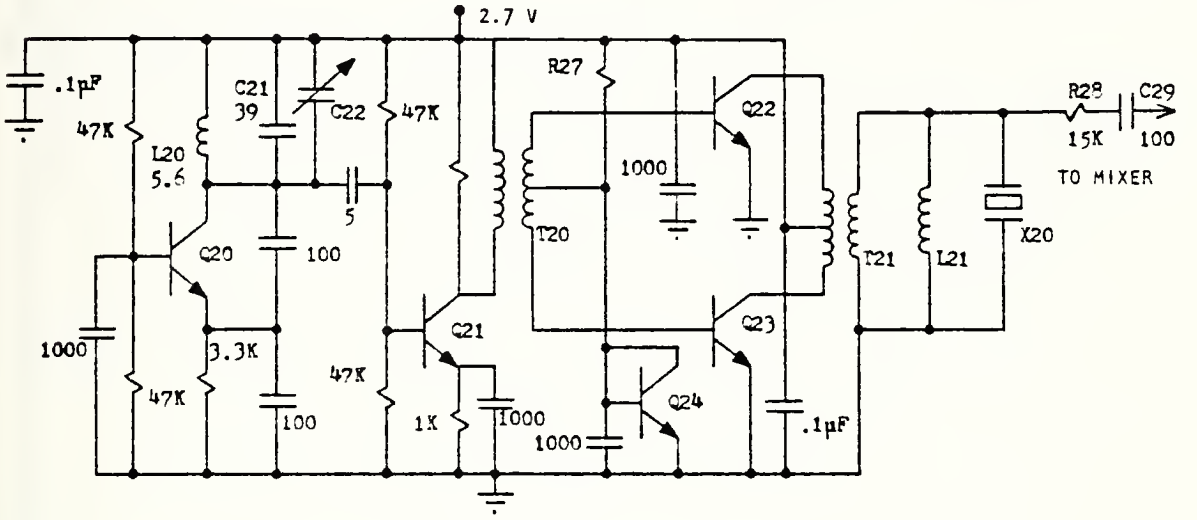

NOTES:

1. Q20 and Q21: 2N3565
2. Q22 to Q24: 2N3904
3. Capacitances in pF except as noted, ceramic series C10, Note 5 Fig. 43 applies
4. uF capacitors are tantalum, Note 6 Fig. 43 applies
5. Resistances in ohms, 1/8 W, 10% tolerance, Allen-Bradley
6. C22 variable capacitor 4 to 18 pF, Thin Trim capacitor, Part No. 9410-4, Johanson Manufacturing Corp., Boonton, NJ 07005. C22 gives tuning range of 6.2 to 6.9 MHz
7. T20 and T21 are identical except primary and secondary reversed. Primary 45 turns No. 34 AWG, secondary 15 turns No. 34 AWG bifilar on ferrite toroid of Q-1 material, Part No. F2062-1, Indiana General, Valparaiso, Ind. 46383
8. L20 in uH, delevan molded RF coil, series 1025, Delevan Electronics Division, 270 Quaker Rd., East Aurora, NY 14052
9. R27 selected to give 14 V peak-to-peak output at a supply current of 18 mA.
10. L21 selected to give an impedance of 1000 ohms at 0° phase in parallel with X20.

Fig. 44. ULTRASONIC TRANSMITTER OF THE MK V BLOOD-FLOW VELOCITY SENSOR.

T20 and T21 for the power amplifier formed by Q22 and Q23. The bias level for the push-pull output transistors is set by Q24 and R27. L21 is chosen in connection with the transmitting piezoelectric crystal X20 to produce an impedance of 1000Ω at a 0° phase shift. The amplifier yields a 14 V peak-to-peak signal across X20 for a power output of 25 mW. The signal from X20 is attenuated and connected to the mixer circuit in the ultrasonic receiver by R28 and C29.

Figure 45 is a schematic of the ultrasonic receiver, mixer and audio amplifier. The input crystal X40 is capacitively coupled to a tuned RF amplifier Q40, and C42 is varied to produce the greatest output at the collector of Q40. The mixer circuit that multiplies the received ultrasonic waves containing the doppler shift with the reference signal from the transmitting amplifier is formed by Q41 and Q42. The output of the mixer at the collector of Q41 is capacitively coupled to a two-stage audio amplifier whose output is connected to the reversed-bias diode in the collector circuit of the VHF oscillator in the FM transmitter.

Figure 46 is the MK V FM transmitter which is identical to the FM transmitter in the MK IV except for the size of its antenna. It is a ferrite rod 3.17 mm in diameter instead of 6.35 mm as in the MK IV. This smaller size allows a thinner overall circuit profile and reduces package volume. There is no noticeable decrease in transmitter range or signal quality.

B. Transcutaneous Power Transmitter

Figure 47 is a schematic of a battery-powered medium-frequency oscillator and amplifier designed to drive the external or primary coil for transcutaneous power transfer. The oscillator is a variable-frequency

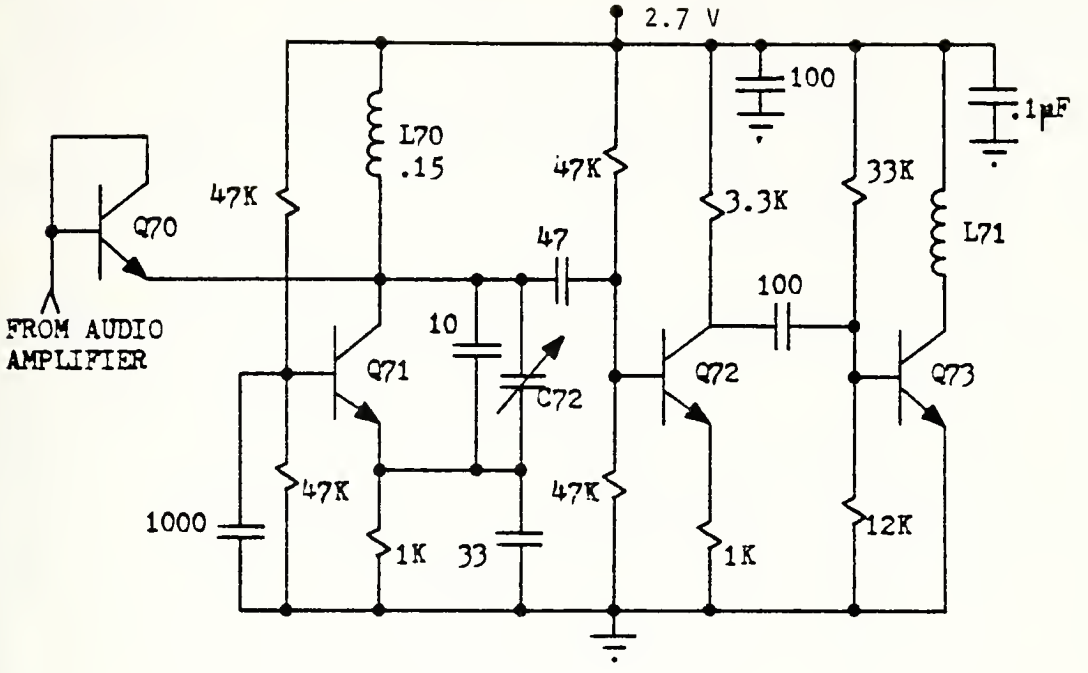

NOTES:

1. Q70 to Q73: 2N3563 manufactured by Fairchild
2. Notes 3, 4, 5 and 8 of Fig. 44 apply
3. C72 variable capacitor 1-4.5 pF, Part No. 9410-0, Note 6 of Fig. 44 applies
4. L72 antenna is 12 turns No. 26 AWG tinned wire on ferrite rod of Q-3 material 3.18 mm diameter and 19.05 mm long, Part No. F172-1, Indiana General, Valparaiso, Ind. 46383
5. Supply current 1.5 to 2.5 mA depending on frequency
6. Tuning range 97 to 105 MHz
7. Range of transmission greater than 10 m

Fig. 46. FREQUENCY-MODULATED TRANSMITTER CIRCUIT OF THE MK V BLOOD-FLOW VELOCITY SENSOR.

or primary coil (L1) is wound of litz wire, series tuned by C1 and transformer coupled to the amplifier output. C1 must be a low-loss capacitor; silver mica is recommended, and ceramic should be avoided. The circuit supply current varies between 25 and 70 mA, depending on antenna

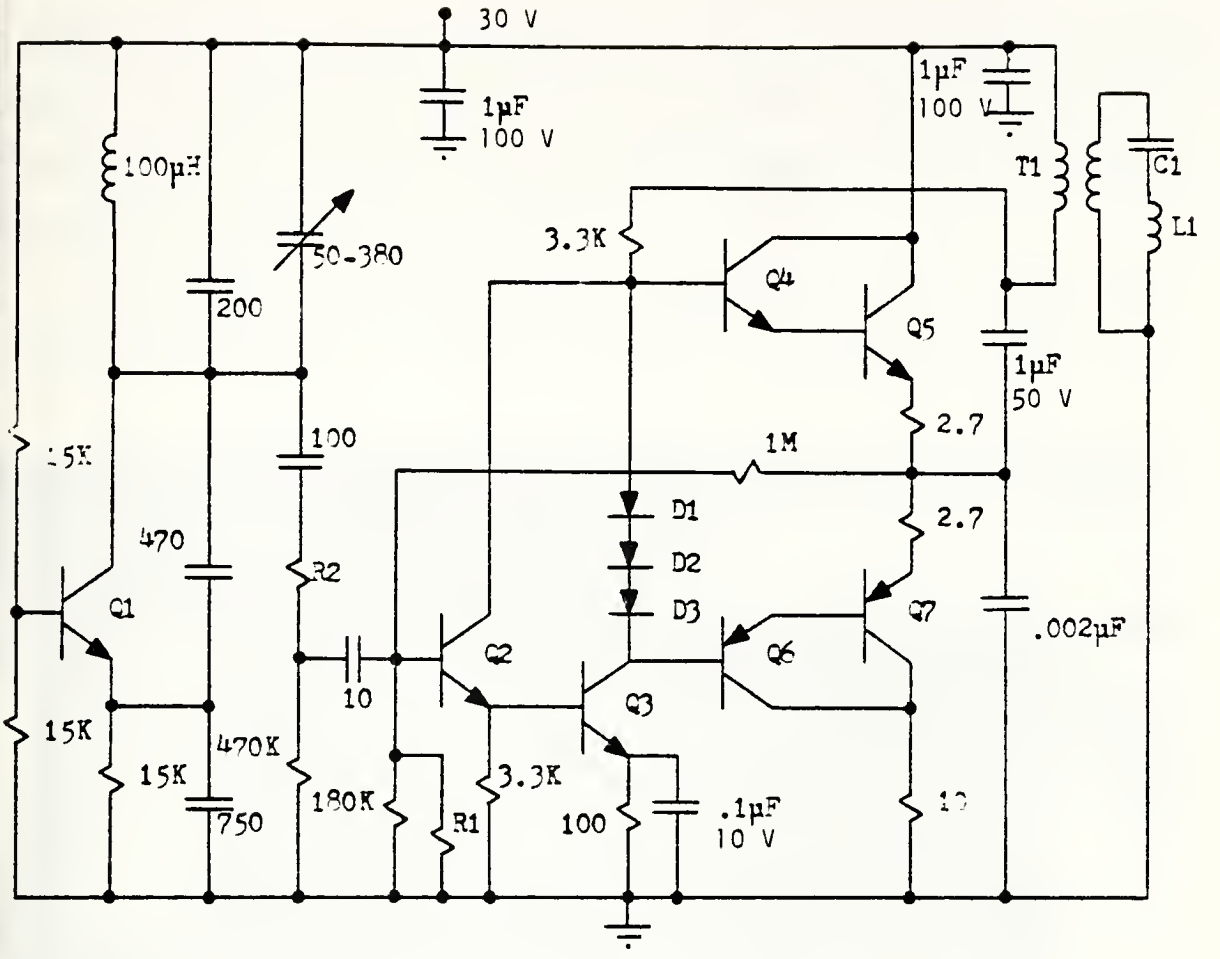

NOTES:

1. Q1 to Q5: 2N3904
2. Q6 and Q7: 2N3906
3. Q5 and Q7 use homemade aluminum heat sink
4. D1 to D3: 1N4148
5. T1 is a toroid of Q-1 material, 12.7 mm O. D., primary 36 turns No. 24 AWG, secondary 9 turns No. 24 AWG, Part No. F627-8, Indiana General, Valparaiso, Ind. 46383
6. L1 is 47 turns of 7-41 AWG litz wire, single layer pancake, 43 mm O. D. wound between two acrylic discs 0.79 mm thick
7. R1 is selected to give a dc output of 15 V with transmitter operating
8. R2 is selected to give maximum output (ac) without spurious oscillations
9. C1 is silver-mica for maximum Q of C1-L1 at series resonance
10. Supply current is 60 to 70 mA with antenna (L1) unloaded
11. Supply current is 25 to 70 mA with antenna loaded depending on the distance between L1 and the implanted pancake coil (coil L1 of Fig. 42)

Fig. 47. TRANSCUTANEOUS POWER-TRANSFER TRANSMITTER FOR THE MK V BLOOD-FLOW VELOCITY SENSOR.

loading; in free air and unloaded, this current is 70 mA. When the primary coil is brought into the proximity of the implanted secondary coil in the blood-flow sensor package, the current drain decreases as the coupling coefficient between the coils increases.

Figure 48 is a laboratory version of the transcutaneous transmitter. The batteries are located under the handle (five 6 V batteries = 30 V),

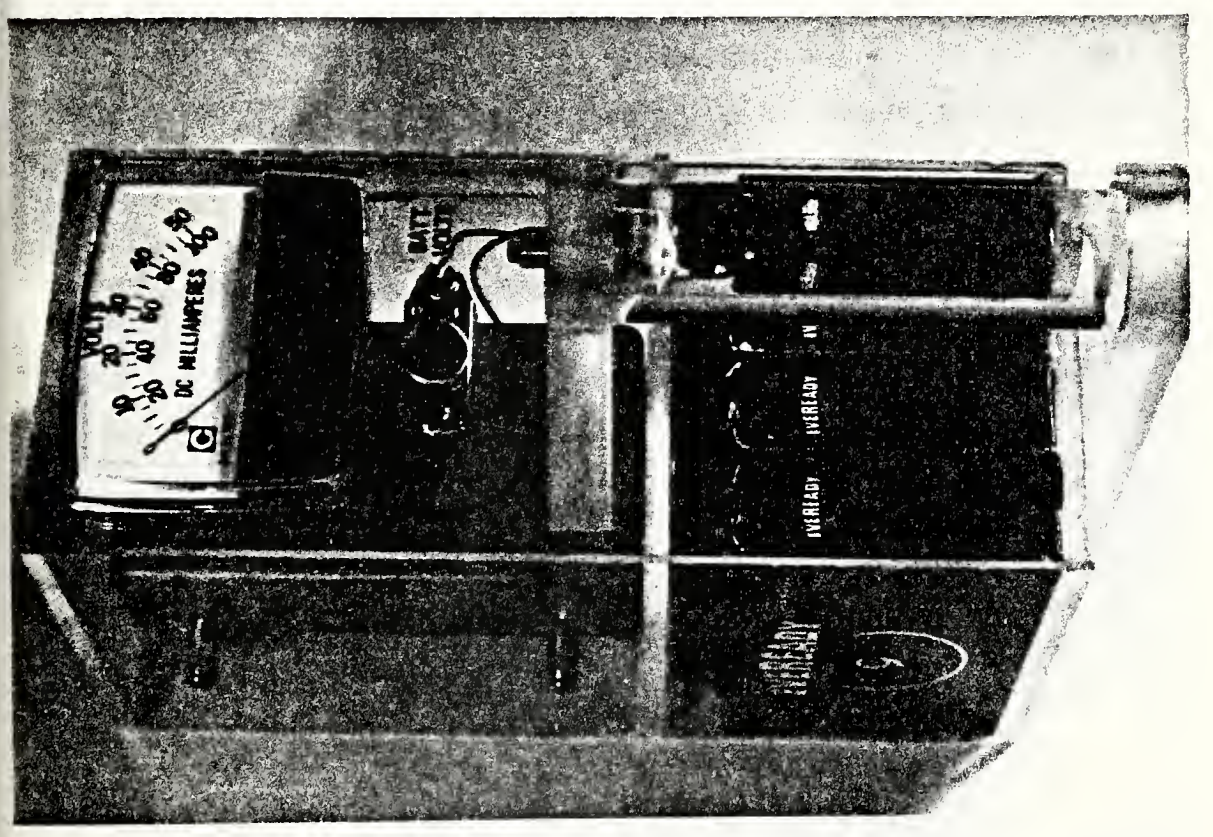

Fig. 48. LABORATORY VERSION OF TRANSCUTANEOUS TRANSMITTER.

and the power on-off switch is in the handle. The transmitter case is made of acrylic plastic to avoid loading the output coil. The purpose of the meter and slide switch is to monitor both supply current and voltage. The supply current is important because it can be used to tune the oscillator and to determine the best position for the external coil. The

oscillator frequency can be adjusted through a hole in the bottom of the acrylic case and in the metal circuit box inside; it should be adjusted for maximum supply current. At this point, the output coil is operating at resonance. The supply current is also monitored when positioning the external coil near the implanted coil; it will be minimum when coil coupling is maximum.

Figure 49 is a photograph of the transmitter being positioned over the blood-flow sensor. The transmitter is turned on and off with the thumb on the spring-loaded pushbutton which minimizes battery usage and prevents inadvertent battery failure caused by leaving the switch on when

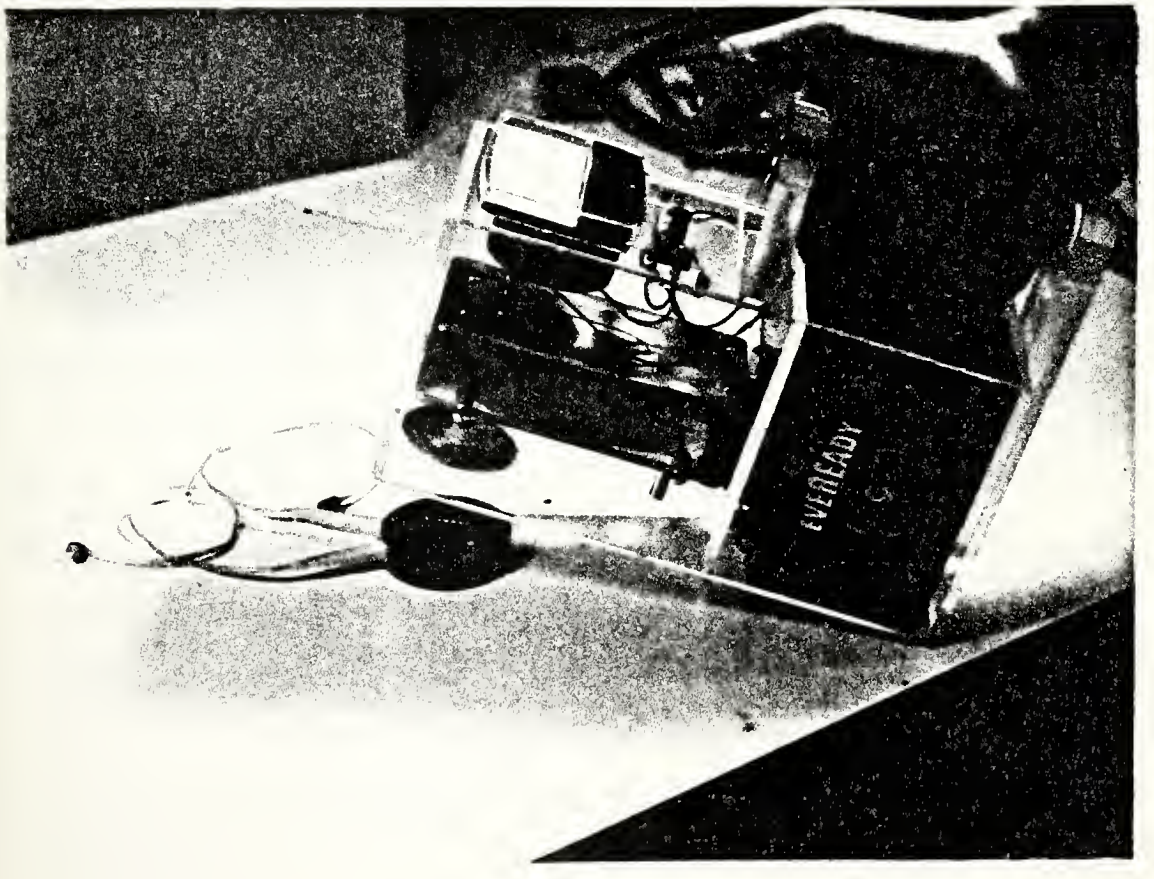

Fig. 49. OPERATION OF TRANSCUTANEOUS TRANSMITTER.

the unit is not in use. This photograph illustrates more clearly the housing of the oscillator and amplifier circuit in a shielded metal box supported in the case away from the primary coil. The primary coil is identical to the implanted secondary coil and is wound from litz wire in a single-layer pancake between two thin acrylic disks to provide mechanical strength.

C. Clinical Experience

On 22 April 1974, the MK V transcutaneously powered discrete-component ultrasonic blood-flow velocity sensor was implanted in a canine at Stanford University Hospital. It operated satisfactorily for six weeks, and then it was removed to allow the canine to become a heart donor. The same unit and transducers were placed in a canine at NASA Ames. Throughout both implants, the sensor functioned satisfactorily. After several months at Ames, the transmitted information became intermittent which indicated cable deterioration.

Experience with this prototype unit demonstrated the practicality of RF induced power from the standpoint of flow measurement interference and coil alignment. As compared with battery powered units in the laboratory, the MK V unit exhibited comparable signal-to-noise ratios and no aural indication of RF interference. Alignment of the external and subcutaneous coils was facilitated by the meter on the transmitter that deflected noticeably when the coils were aligned for maximum coupling. Coil separation was small with the package implanted just under the canine's skin. A misalignment of the coils equal to their radius was possible without loss of information.

Chapter VI

CONCLUSIONS AND RECOMMENDATIONS

A. Summary

This report has described the design of a discrete-component blood-flow sensor and a transcutaneous power theory and system. The study has also been concerned with the development of a low-voltage regulator and reference. This work was based on the concept that maximum usage of a transcutaneous power system would depend on an efficient regulator circuit to produce a stable supply voltage to operate implanted circuits that have previously been battery operated.

A comprehensive transcutaneous power theory has been developed, and the major factors contributing to power-transfer efficiency and to power losses were identified and included in a simple efficiency equation. Techniques to minimize power losses in actual coil design were described. Close agreement between theory and experiments has proven the validity of the derived equations.

A unique prototype low-voltage reference has been constructed. The efficiency of voltage regulators was investigated, and the key factors contributing to inefficiency were identified. Solutions to these sources of inefficiency were demonstrated through a prototype voltage regulator capable of monolithic fabrication.

A major emphasis of this report has been directed toward the design, fabrication and use of a miniature ultrasonic blood-flow velocity sensor. The purpose of this sensor was to meet the urgent demand for a clinical device to monitor blood flow while the development of an integrated-circuit flow sensor continued. The basic design goals included package

volume reduction, circuit reliability, simplicity and reproducibility, wider FM transmitter range, increased signal-to-noise ration, and more reliable operation of the command receiver. These goals have been achieved, and a new flow sensor (the MK IV unit) has been developed.

The culmination of this research and the study of transcutaneous power was the fabrication of a miniature blood-flow sensor (the MK V) that is only one-third the size of the MK IV, contains no batteries and is transcutaneously powered. The circuit design of this unit has been discussed, and the results obtained from implants were described.

B. Findings

The following conclusions can be drawn from this report.

(1) Transcutaneous power transfer is a practical and reasonably efficient means of powering implanted electronic sensors.

(2) Definite guidelines must be established to maximize power-transfer efficiency.

(3) A properly designed and applied power-transfer circuit is capable of efficiencies as high as 90%.

(4) A unique voltage-reference circuit fabricated in monolithic form yields 1.244 V, is stable to better than 200 ppm/°C, and operates from less than 100 μA.

(5) A voltage regulator compatible for use with implanted circuits designed to operate from two mercury cells can be designed with 85% power efficiency.

(6) The primary causes of failure among discrete-component implanted blood-flow velocity sensors are battery and transducer cable failures.

(7) Implanted circuits properly encapsulated in Paraplast are waterproof and immune to damage from body fluids.

(8) Transcutaneously powered blood-flow velocity sensors are practical.

C. Recommendations

As a result of this study, many improvements were conceived for the operation and longevity of implanted blood-flow sensors. The three major recommendations concern transducer cables, circuit components, and transcutaneous power. Transducer cables will remain the primary "weak link" when transcutaneous power is used, and more research is required to improve cable longevity in the implanted environment. Possible solutions include more careful assembly of the coaxial cable in the silastic tubing, the use of larger tubing to increase the volume of medical adhesive around the cable and the use of stainless steel cables.

The reliability of circuit components can be improved by replacing much of the discrete circuitry with standard integrated circuit packages containing either custom or commercially available circuits. This approach would eliminate many of the potentially troublesome soldered joints. Care must be taken, however, not to sacrifice circuit simplicity and the use of standard miniature components when components external to the IC packages are required. The simple but effective printed circuit board could still be used for mounting all components.

Transcutaneous power should be encouraged because it eliminates the possibility of battery failure.

REFERENCES

1. E. L. Chaffee and R. U. Light, "Method for Remote Control of Electrical Stimulation of Nervous System," Yale Journal of Biology and Medicine, 7, 1934, pp. 83-128.

2. W. W. L. Glenn and A. Mauro, "Remote Stimulation of the Heart by Radio-Frequency Transmission," New England Journal of Medicine, 261, 1959, pp. 948-951.

3. L. D. Abrams, W. A. Hudson and R. Lightwood, "A Surgical Approach to the Management of Heart Block Using an Inductive-Coupled Artificial Cardiac Pacemaker," Lancet, June 25, 1960, pp. 1372-1374.

4. L. Eisenberg, A. Mauro and W. W. L. Glenn, "Transistorized Pacemaker for Remote Stimulation of the Heart by Radio-Frequency Transmission," IRE Trans. on Bio-Medical Electronics, BME-8, 1961, pp. 253-258.

5. D. M. Hickman et al, "A Portable Miniature Transistorized Radio-Frequency Coupled Cardiac Pacemaker," IRE Trans. on Bio-Medical Electronics, BME-8, 1961, pp. 258-262.

6. J. G. Davies, "Artificial Cardiac Pacemakers for the Long-Term Treatment of Heart Block," Journal of the British IRE, 24, 1962, pp. 453-456.

7. P. I. Hershberg et al, "Pathologic Effects of Recharging Nickel-Cadmium Cells through the Intact Skin - A Preliminary Report," Trans. of the American Society of Artificial Internal Organs, 11, 1965, pp. 143-147.

8. G. H. Myers et al, "Experimental Radio-Frequency Cartoid-Sinus Pacemaker," Medical Research Engineering, 7, 1, First Qtr 1968, pp. 13-16.

9. A. M. Dolan et al, "Heat and Electromagnetic Energy Transport through Biological Material at Levels Relevant to the Intrathoracic Artificial Heart," Trans. of the American Society of Artificial Internal Organs, 12, 1966, pp. 275-281.

10. F. W. Fraim and F. N. Huffman, "Performance of a Tuned Ferrite Core Transcutaneous Transformer," IEEE Trans. on Bio-Medical Engineering, BME-18, 1971, pp. 352-359.

11. J. W. Fuller and H. M. Bourland, "Efficient Power Transfer through a Tissue Barrier," Proc. of the 19th Annual Conf. on Engineering in Medicine and Biology, 8, 1966, p. 150.

12. J. W. Fuller, "Apparatus for Efficient Power Transfer through a Tissue Barrier," IEEE Trans. on Bio-Medical Engineering, BME-15, 1968, pp. 63-65.

13. R. J. Harvey et al, "Studies Related to Development of an Implantable Power Source for Circulatory Assist Devices," American Journal of Surgery, 114, 1967, p. 61.

14. L. Heimlich and F. Christiansen, "Energy Transmission through the Intact Skin," Artificial Heart Program Conference, (R. J. Hegyeli, ed.), U. S. Government Printing Office, Washington, D. C., 1969, pp. 937-944.

15. G. H. Myers, A. Thumin and G. E. Reed, "Power Transfer Device for Mechanical Hearts," ASME - Paper 68, 1968, p. 8.

16. G. H. Myers et al, "A Transcutaneous Power Transformer," Trans. of the American Society of Artificial Internal Organs, 14, 1968, pp. 210-217.

17. P. M. Newgard, J. R. Woodbury and L. T. Harmison, "Implantable Electrical Power and Control System for Artificial Hearts," Intersoc. Energy Conversion Engineers Conf., 7th Conference Proc., San Diego, California, Sept. 25-29, 1972, pp. 765-799.

18. P. M. Newgard and G. Eilers, "Skin Transformer and Power Conditioning Components," Artificial Heart Program Conference (R. J. Hegyeli, ed.), U. S. Government Printing Office, Washington, D. C., 1969, pp. 927-936.

19. J. C. Schuder and H. E. Stephenson, "Energy Transport through Closed Tissue Walls by Capacitive-Conductive Coupling," Digest of the 1961 International Conference on Medical Electronics, Radio Corporation of America Laboratories, Princeton, New Jersey, 1961, p. 51.

20. J. C. Schuder, H. E. Stephenson and J. F. Townsend, "Energy Transfer into a Closed Chest by Means of Stationary Coupling Coils and a Portable High-Power Oscillator," Trans. of the American Society of Artificial Internal Organs, 7, 1961, pp. 327-331.

21. J. C. Schuder, H. E. Stephenson and J. F. Townsend, "High-Level Electromagnetic Energy Transfer through a Closed Chest Wall," IRE International Convention Record (Pt. 9), 9, 1961, pp. 119-126.

22. J. C. Schuder and H. E. Stephenson, "Energy Transport into the Closed Chest from a Set of Very Large Mutually Orthogonal Coils," IEEE Communications and Electronics, Jan. 1963.

23. J. C. Schuder and H. E. Stephenson, "Energy Transport and Conversion for a Permanently Implanted Artificial Heart," Trans. of the American Society of Artificial Internal Organs, 9, 1963. pp. 286-291.

24. J. C. Schuder, "Parametric Motor Energized by Radio-Frequency Field," Proc. of the IEEE, 51, 1963, p. 399.

25. J. C. Schuder and H. E. Stephenson, "Energy Transport and Conversion in the Artificial Heart," in Heart Substitutes, by Albert N. Brest (Charles C. Thomas, Publisher), CH. 15, 1964, pp. 1-10.

26. J. C. Schuder, J. H. Gold and H. E. Stephenson, "Transport of Very High Power Levels through the Skin by Inductively Coupled Radio-Frequency System" Abstract No. 87, Electrochemical Society Extended Abstracts, Atlantic City, New Jersey, Oct. 4-8, 1970, pp. 219-220.

27. J. C. Schuder, J. H. Gold and H. E. Stephenson, "Ultrahigh Power Electromagnetic Energy Transport into the Body," Trans. of the American Society of Artificial Internal Organs, 17, 1971, pp. 406-410.

28. J. C. Schuder, J. H. Gold and H. E. Stephenson, "An Inductively Coupled RF System for the Transmission of 1KW of Power through the Skin," IEEE Trans. on Bio-Medical Engineering, BME-18, 1971, pp. 265-273.

29. H. E. Stockman, "Parametric Motor Energized by Radio-Frequency Field," Proc. of the IEEE, 51, 1963, p. 1253.

30. A. Thumin et al, "A Power Transformer for Mechanical Hearts," Artificial Heart Program Conference (R. J. Hegyeli, ed.), U. S. Government Printing Office, Washington, D. C., 1969, pp. 915-926.

31. G. R. Abell, "Practical Design of an Implantable Passive Receiver of Radio-Frequency Energy," 20th Annual Conf. of Engineering in Medicine and Biology, Boston, Massachusetts, Nov. 13-16, 1967.

32. C. C. Stenberg, H. W. Burnette and R. C. Bunts, "Electrical Stimulation of Human Neurogenic Bladders: Experience with Four Patients," Journal of Urology, 97, 1967, pp. 79-84.

33. T. Hald et al, "Clinical Experience with a Radio-Linked Bladder Stimulator," Journal of Urology, 97, 1967, pp. 73-78.

34. W. H. Ko and E. Yon, "RF Induction Power Supply for Implant Circuits," Digest of the 6th International Conf. on Medical Electronics and Biological Engineering, Tokyo, 1965, pp. 266-267.

35. M. L. Leonhardt and D. A. Hodges, "An Inductively Coupled Power Source," Report of Research sponsored in part by the Joint Services Electronics Program, Contract F44620-71-C-0087, Electronics Research Laboratory, University of California, Berkeley, California, 94720.

36. T. B. Fryer and H. Sandler, "A Rechargeable Battery System for Implanted Telemetry Systems," 23rd ACEMB, Washington, D. C., 1970, p. 129.

37. F. E. Terman, Electronic and Radio Engineering, McGraw-Hill Book Co., 1955, pp. 21-24.

38. Bulletin of the Bureau of Standards, 8, No. 1, 1912, pp. 1-238.

39. "Radio Instruments and Measurements," Circular of the National Bureau of Standards C74, U. S. Government Printing Office, Washington, D. C., 1937, p. 257.

40. R. J. Widler, "Application Notes: Monolithic Voltage Regulator," National Semiconductor Corporation, 1967.

41. R. J. Widler, "New Developments in I. C. Voltage Regulators," IEEE Journal of Solid-State Circuits, SC-9, 1974, pp. 192-194.

42. R. C. Jaeger, "A High Output Resistance Current Source," IEEE Journal of Solid-State Circuits, SC-9, 1974, pp. 192-194.

43. J. S. Brugler, "Silicon Transistor Biasing for Linear Collector Current Temperature Dependence," IEEE Journal of Solid-State Circuits, SC-2, 1967, pp. 57-58.

44. P. N. T. Wells, Physical Principles of Ultrasonic Diagnosis, Academic Press, 1969, p. 195.

Thesis
C9585
c.1

Curtis

187440

Transcutaneous
power and ultrasonic
blood-flow velocity
sensors.